

# Kinematic Analysis of faint blue stars in the MMT HVS survey

Bachelorarbeit aus der Physik

Vorgelegt von  
**Sebastian Weich**  
25.07.2022

Dr. Karl Remeis-Sternwarte Bamberg  
Friedrich-Alexander-Universität Erlangen-Nürnberg



Betreuer: Prof. Dr. Ulrich Heber und M.Sc. Matti Dorsch



# Abstract

The old stellar population of the Galactic halo provides a huge amount of mass probes for investigating the structure, the history and the shape of the gravitational potential of the Milky Way, especially its dark matter halo. Therefore, a spectroscopic survey at the Multiple-Mirror-Telescope (MMT) recorded an unbiased sample of faint blue halo stars, based on strict color and magnitude constraints.

Kreuzer (2021) revisited the MMT sample by complementing the spectroscopic data with *Gaia* DR2 astrometry and carried out a comprehensive analysis of atmospheric, stellar and kinematical properties. Since *Gaia* EDR3 has been published in the meantime, providing improved proper motions, the kinematic analysis of the MMT sample is redone for the most abundant stellar classes of the sample, which are blue horizontal branch (BHB) stars, blue stragglers (BSs) and white dwarfs (WDs). Galactic space velocity components ( $U, V, W$ ) are derived, based on spectrophotometric distances and radial velocities from Kreuzer (2021) and the new proper motions. Galactic trajectories are computed, in order to assign the stars to the Galactic populations of the thin and thick disk, as well as the halo. To this end, a new classification scheme is developed, which makes use of six kinematic diagrams, beginning with the  $U - V$ ,  $W - V$  and  $W - U$  diagrams. Properties of the orbits, i.e. their eccentricities ( $e$ ), their  $Z$ -components of the angular momentum ( $L_Z$ ) and their maximum extensions above or below the Galactic plane ( $z_{\max}$ ), complete the set of classification tools. The results are compared to the predictions from a Galactic model for each diagram in terms of population contours. A system of population scores finally allows the assignment of individual stars to a Galactic population.

Accordingly, the white dwarf sample is dominated by the thin disk population and consists of 79% thin disk stars, 19% thick disk stars and 2% halo stars. This was expected, because of the proximity of most WDs. The halo candidates are confirmed by the shape of their orbits. The BHB star and BS samples, however, are strongly dominated by the halo population, because of the large average distances (even beyond 100 kpc) of the stars. For both classes more than 98% belong to the halo population.

Six BHB stars and two BSs are identified to be possibly unbound to the Galaxy, as their boundness probability is below 5%. A particularly enigmatic object is the blue straggler J0946+4256, because it is traveling towards the Galactic plane rather than receding, which suggests that it comes from the outskirts of the Galactic halo or from even further away towards us. An alternative scenario, based on binary star evolution, is discussed to unravel the nature of J0946+4256. Follow-up observations are required to confirm or falsify its nature.

# Contents

<b>1</b>	<b>Introduction</b>	<b>1</b>
<b>2</b>	<b>Theoretical Background</b>	<b>3</b>
2.1	Stellar evolution . . . . .	3
2.1.1	Hertzsprung-Russell and Kiel diagram . . . . .	3
2.1.2	White dwarfs . . . . .	6
2.1.3	Blue horizontal branch stars . . . . .	6
2.1.4	Blue stragglers . . . . .	6
2.2	Astrometry . . . . .	7
2.2.1	Equatorial coordinate system . . . . .	7
2.2.2	Galactic coordinate system . . . . .	8
2.2.3	Distance measurements . . . . .	9
2.2.4	Velocity components and proper motion . . . . .	11
2.3	Different Galactic populations . . . . .	12
2.3.1	Thin disk population . . . . .	12
2.3.2	Thick disk population . . . . .	13
2.3.3	Halo population . . . . .	13
2.3.4	Metallicity and $\alpha$ -enhancement . . . . .	13
2.4	The Milky Way gravitational potential . . . . .	15
<b>3</b>	<b>Telescopes and Instruments</b>	<b>17</b>
3.1	The MMT HVS survey . . . . .	17
3.2	The <i>Gaia</i> space mission . . . . .	18
<b>4</b>	<b>Methods and Tools</b>	<b>20</b>
4.1	Previous classification scheme . . . . .	20
4.2	The extended classification scheme . . . . .	24
<b>5</b>	<b>White Dwarfs in the MMT sample</b>	<b>28</b>
5.1	Previous findings . . . . .	28
5.2	Comparison of <i>Gaia</i> DR2 and EDR3 astrometric data . . . . .	33
5.2.1	Proper motions . . . . .	33
5.2.2	Distances . . . . .	33
5.3	Kinematic analysis . . . . .	34
5.4	Discussion of the halo candidates . . . . .	37
<b>6</b>	<b>Blue Horizontal Branch stars in the MMT sample</b>	<b>39</b>
6.1	Previous findings . . . . .	39
6.2	Comparison of <i>Gaia</i> DR2 and EDR3 proper motions . . . . .	42
6.3	Kinematic analysis . . . . .	42

<b>7</b>	<b>Blue Stragglers in the MMT sample</b>	<b>48</b>
7.1	Previous findings . . . . .	48
7.2	Comparison of <i>Gaia</i> DR2 and EDR3 proper motions . . . . .	51
7.3	Kinematic analysis . . . . .	51
<b>8</b>	<b>Discussion of the kinematically most extreme objects</b>	<b>57</b>
<b>9</b>	<b>Summary and outlook</b>	<b>62</b>
	<b>References</b>	<b>64</b>



# 1 Introduction

Over thousands of years astronomy and the mechanisms of the night sky have always exerted fascination on mankind. For a long time, observations were only possible with the naked eye, until Galileo Galilei and Johannes Kepler invented the first telescopes in the 17<sup>th</sup> century. This led to the first scientific discoveries and astronomical theories about the universe. In the following time, especially since the end of the 19<sup>th</sup> century, more and more sophisticated technologies were developed and new fields have been opened, for example the examination of the whole cosmic electromagnetic spectrum or the multi-messenger astronomy. Therefore, our knowledge about the universe is continuously increasing.

Of special interest is, of course, our nearest vicinity, our home Galaxy - the Milky Way. Its structure, motion and formation history is a very interesting and highly topical field of research. In particular, the old Galactic halo provides considerable insight into the history of the Galaxy in terms of debris from past merger events with other galaxies or stellar streams. Furthermore, the old stellar halo population provides access to unravel the mass and the shape of the invisible dark matter halo.

Hence, Brown et al. (2003) started a spectroscopic survey of faint blue halo stars by recording their spectra with the Multiple Mirror Telescope (MMT), based on strict photometric criteria. This sample of stars is referred to as MMT sample. After the first serendipitous discoveries of so-called hyper-velocity-stars (HVSs) within the sample, which are stars gravitationally unbound to the Galaxy and probably ejected somewhere in the Galactic disk, a systematic search for them has been triggered. This survey was completed in 2014 (Brown et al. 2014), but suffered from a lack of reliable astrometric data, like parallaxes and proper motions.

In 2014, however, the *Gaia* space mission started, with the aim to provide extremely precise astrometric data for over one billion of stars within the Milky Way. Thus, Kreuzer (2021) revisited and comprehensively reanalysed the whole MMT sample in terms of atmospheric, stellar and kinematic properties by using astrometric data from the second *Gaia* data release (*Gaia* DR2), in addition to the MMT spectroscopic data. Since the early third data release (EDR3) of *Gaia* has been published in the meantime and as the *Gaia* mission is designed to increase in precision due to long term observations, it appears worthwhile to redo the kinematic analysis of the MMT sample, which is the aim of this work. While the spectroscopic and photometric data is adopted from Kreuzer (2021), the astrometric data, especially the proper motions, are exchanged by that from *Gaia* EDR3. Additionally, a classification scheme is developed to distinguish between thin disk, thick disk and halo stars, based on their kinematics. This is essentially built on the empirical classification scheme from Pauli et al. (2006), but is extended and improved.

The majority of objects in the MMT sample are blue horizontal branch (BHB) stars, blue stragglers (BSs) and white dwarfs (WDs). These are referred to as MMT BHB sample, MMT BS sample and MMT WD sample, respectively. All of them will be investigated from a kinematical point of view in this work.

First of all some theoretical background is briefly discussed in chapter 2, like stellar evolution, astrometric measurements and the structure of the Milky Way. Then the two most important telescopes for this work, the MMT and *Gaia*, are outlined in chapter 3, before addressing the newly developed classification scheme in chapter 4. In the following three chapters, first of all the findings of Kreuzer (2021) are summarized and then the results of the kinematic analyses are presented for each sample, respectively. Finally, the kinematically most extreme and also most exciting objects of this work are discussed in chapter 8.

# 2 Theoretical Background

## 2.1 Stellar evolution

Similar to human life cycles on Earth, stars are born, undergo different evolutionary stages during their life and finally die, for example in a supernova explosion. This is called stellar evolution and sets the stage for stellar astronomy. So stars are typically formed in huge gas and dust clouds, which contract under their own gravity. The masses of these clouds are often on the order of several ten thousands of solar masses and thus, the collapse brings not only one single star to life, but an extensive amount of them. The following evolution mostly depends on the initial masses of the born stars and will be briefly described in the next sections.

### 2.1.1 Hertzsprung-Russell and Kiel diagram

Since a large variety of different star populations can be observed, a reliable classification scheme is needed to distinguish them from each other. The probably most famous one is the Hertzsprung-Russell diagram (HRD), invented by Ejnar Hertzsprung and Henry Norris Russell in the early 20th century. There the absolute visual magnitude was plotted against the spectral type. But since the absolute magnitude is related, for example, to the luminosity and the spectral type to the effective surface temperature  $T_{\text{eff}}$ , there exist also other common combinations. So modern versions of the HRD often make use of these two fundamental properties of a star by plotting luminosity in solar units versus  $T_{\text{eff}}$  as shown in Figure 2.1.

Different stellar stages of evolution become apparent from structures of stars in specific regions in the HRD. For instance, the most prominent structure can be seen as almost straight diagonal line from the bottom right to the top left, which is called the main sequence (MS). Every star begins its life on the MS and spends most of the time there, burning hydrogen to helium via thermonuclear fusion. But once the hydrogen reservoir of a star gets exhausted and the fusion in the core stops, the star is only powered by a hydrogen-burning shell. While the outer layers increase in size, the core shrinks and the star moves to the top right in the HRD becoming a red giant on the red giant branch (RGB). When the conditions in the core get extreme enough, the fusion of helium to heavier elements, mainly carbon and oxygen, sets in and the core becomes electron degenerate, which leads to violent ignition of helium burning once the central temperature reaches  $10^8$  K. The star remains in this phase of evolution (the so-called horizontal branch, HB) until all fuel is burned to carbon and oxygen. Then helium burning proceeds in a shell around the core with hydrogen burning progressing in outer layers. The star expands again to supergiant dimensions (the so-called asymptotic giant branch, AGB, in the HRD). At its tip the star strips its outer layers and only the degenerate core remains, called a white

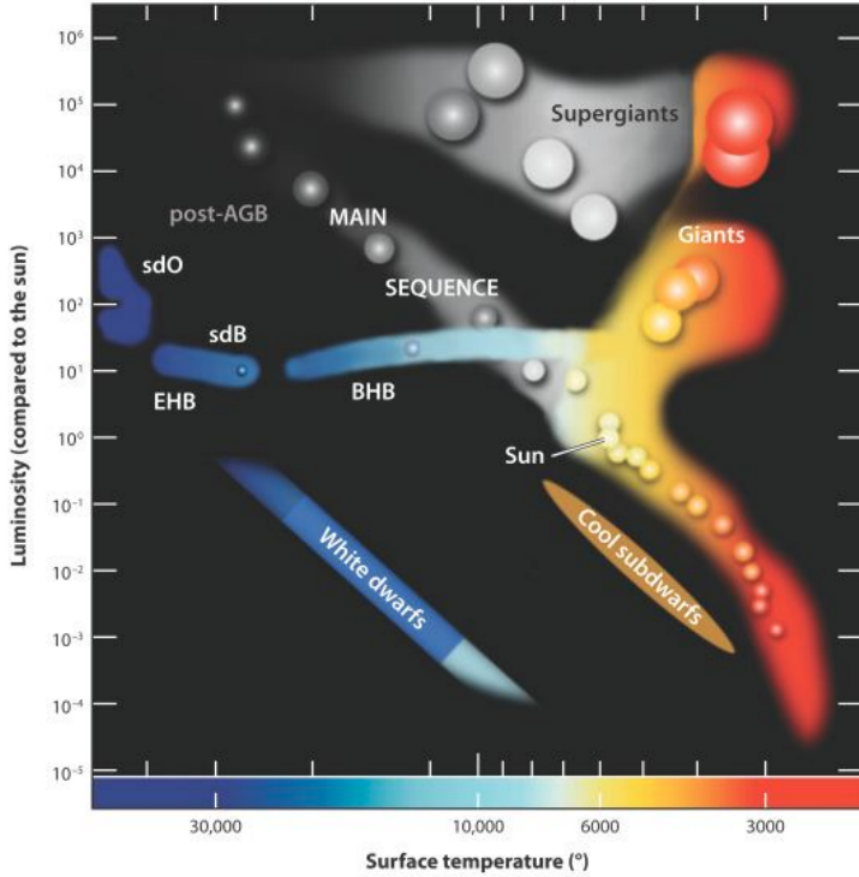


**Figure 2.1:** Sketch of a Hertzsprung-Russell diagram. Main sequence (MS) as almost straight diagonal line from the bottom right to the top left. Giants and supergiants above the MS. The HB crossing the MS with its bluest members, the blue horizontal branch (BHB) stars, to the left and below the MS and the extreme horizontal branch (EHB) as left part of the HB with its members, subdwarfs of type O and B (sdO/B). WDs at the bottom left and cool subdwarfs at the right below the MS (Heber 2009).

dwarf (WD). WDs are settled in the bottom left of the HRD below the MS. This scenario is a bit simplified and accounts only for stars with masses of half to about twice the solar mass. The most massive stars ( $> 8 M_{\odot}$ ) will path a different way and end up in a big supernova explosion, forming a neutron star or a black hole.

Another way of displaying different phases of stellar evolution is plotting a Kiel diagram, as shown in Figure 2.2. The difference to the HRD is that the luminosity on the y-axis is exchanged by the surface gravity, what means a Kiel diagram only involves directly measurable atmospheric parameters. To convert a Kiel diagram to the HRD the distance needs to be known for deriving the stellar luminosity.

The most important phases of stellar evolution for this work are white dwarfs (WD), blue horizontal branch (BHB) stars and blue stragglers (BS), which are a exceptional form of BHB stars. All of them will be discussed more detailed in the next sections.

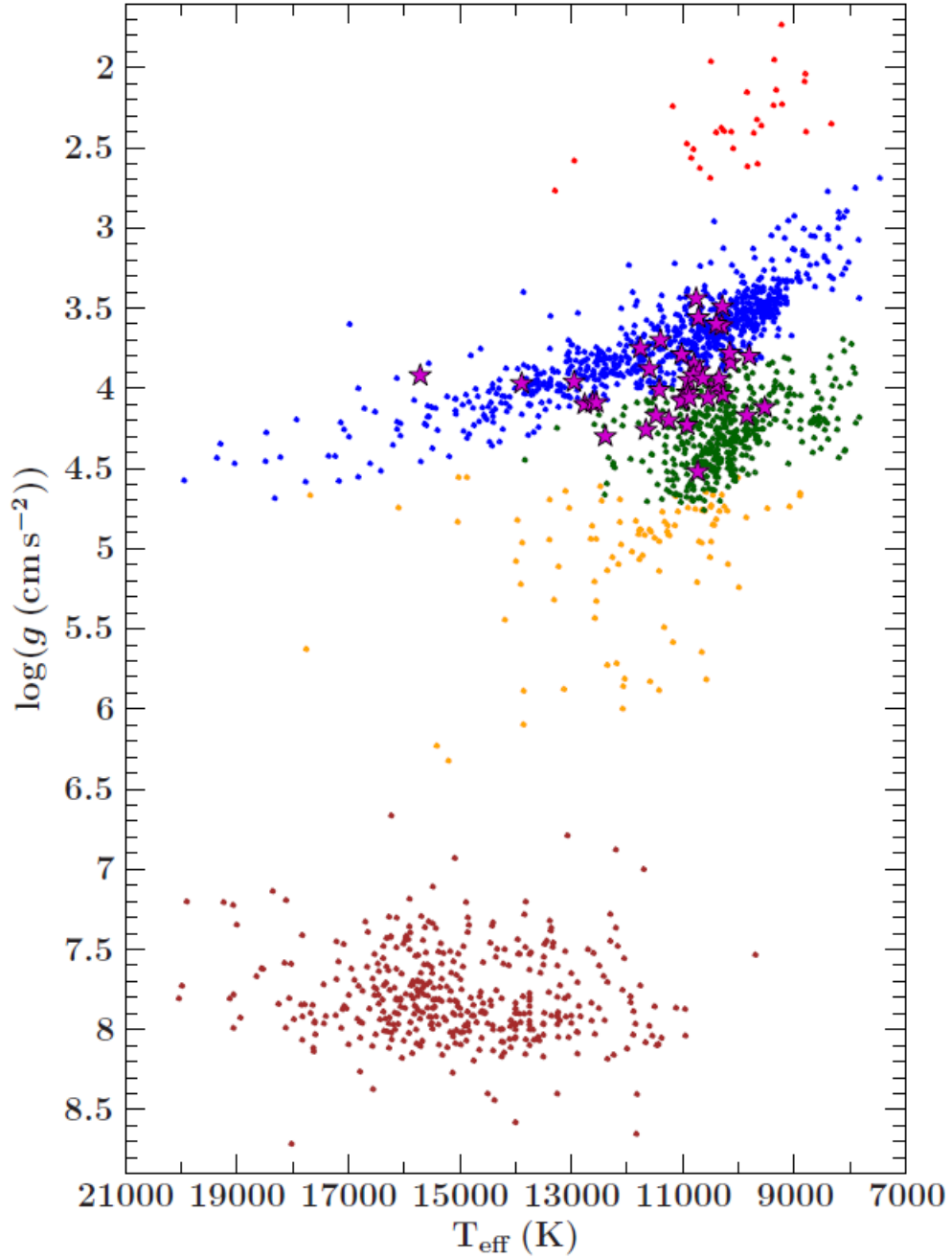


**Figure 2.2:** Kiel diagram of all analyzable candidates from the MMT HVS survey (see section 3.1). Different classes of stars are plotted in different color. From top to bottom: extragalactic supergiants (red), BHB stars (blue), BSs (green), pre-ELM WD candidates or sdB (yellow), WDs (brown). The positions of all MMT HVS candidates are overplotted as magenta stars with black edges. Since only the WDs, BHB stars and BSs will be investigated in this work, all other kinds of objects won't play a role and can be neglected (taken from Kreuzer 2021).

### 2.1.2 White dwarfs

As described above, WDs are endstages of stellar evolution, are stabilized by the pressure of the degenerate electron gas and do not produce energy by nuclear fusion any more. However, they are very compact objects with masses up to  $1.4 M_{\odot}$  (Chandrasekhar mass limit). Hence, they have high surface gravities and release energy from cooling of the ion gas by radiation, which makes them slowly cool down. Spectroscopically, they can be divided into two subgroups, namely DA and DB white dwarfs. While DA WDs only show hydrogen in their spectra, DB WDs only show helium. In general WDs are very faint and about 10 mag (or more) fainter than their main sequence counter parts. Thus, they can be observed just in a small volume around us.

### 2.1.3 Blue horizontal branch stars

The horizontal branch (HB) is the region in the HRD, where hot blue stars are located, which burn helium in their cores (see Figure 2.1). It can be divided into the extreme horizontal branch (EHB), which contains subdwarfs of spectral types O and B, called sdO and sdB, respectively, and the blue horizontal branch (BHB). The latter ones are an old population with stable helium burning in their cores and move slowly towards higher luminosities, before becoming red giants and entering the RGB. Blue horizontal branch stars also make up an important part of the Galactic halo population (see subsection 2.3.3).

### 2.1.4 Blue stragglers

Blue Stragglers (BSs) are often seen, for example, in star clusters, where all stars have formed at the same time. In a color-magnitude diagram (CMD, equivalent to a HRD if all objects are at the same distance) the point on the MS, where these stars are about to leave it towards the RGB, is called turnoff point (see Figure 2.3). However, it turns out that often some stars are left on the MS above the turnoff point. If these are still on the MS, they would need to be younger than the cluster, but yet are cluster members. This is in discrepancy to the evolution time (mass-age-relation) of these stars, so they are called blue stragglers. The origin of them is still debated, but it is believed that they must have undergone a rejuvenation event. This can be, for example, the merge of two single low mass stars. As mentioned above BSs can often be seen in clusters and thus, are also found in the Galactic halo, which is studded with globular clusters.

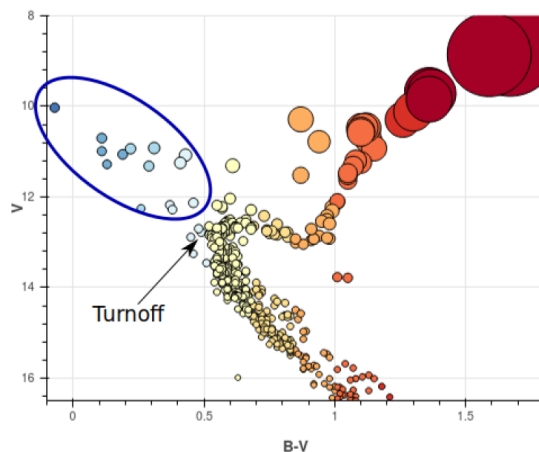


**Figure 2.3:** Positions of the BSs (blue ellipse) and the MS turnoff in a CMD of M67 (taken from Kreuzer 2021).

## 2.2 Astrometry

One of the fundamental aims in astronomy is to observe the positions and the motions of celestial objects in space. In order to make them unambiguous for different observers, it is necessary to define proper coordinate reference systems. Furthermore many physical quantities, like the velocity of a star, can not be directly measured. Thus, one needs to transform measurable parameters into such, one can deal with. The way of doing so and different common coordinate systems will be explained in the next sections.

### 2.2.1 Equatorial coordinate system

The Equatorial Coordinate System (ECS) is directly correlated to our position in space, as its origin is the center of Earth. Hence, it is best suited to describe the coordinates of an object on the night sky, also called the celestial sphere. However, the ECS is independent of the location of the observer on Earth, since its fundamental plane is the projection of Earth's equator onto the celestial sphere. This plane is called the celestial equator. Every star's position can be indicated by a pair of equatorial coordinates, the *right ascension*  $\alpha$  (RA) and the *declination*  $\delta$  (Dec), as shown in Figure 2.4.

The right ascension is defined similar to the terrestrial longitude. It measures the angular distance of an object eastwards, starting from the vernal equinox  $\Upsilon$  (which is one of the two points of intersection between the celestial equator and the ecliptic) along the celestial equator and is either given in sidereal hours, minutes and seconds or in degrees. Therefore it can range from 0h to 24h or from  $0^\circ$  to  $360^\circ$ , respectively.

The declination is analogous to the terrestrial latitude and measures the angular distance of an object perpendicular to the celestial equator. It ranges from  $90^\circ$  at the northern celestial pole, over  $0^\circ$  at the celestial equator, to  $-90^\circ$  at the southern celestial pole.

In reality, due to the dynamics of the Earth considered as rigid body, there occur effects like precession and nutation. These slightly move Earth's axis and cause the ECS to change over the course of years. For short enough time scales this can be neglected, but for longterm observations it must be taken into account, which is usually done by referring all positions, for instance in a catalog, to a so-called epoch. For example, since 1984 the Julian epoch J2000 is used, which corresponds to January 1, 2000, at 12:00 terrestrial time.

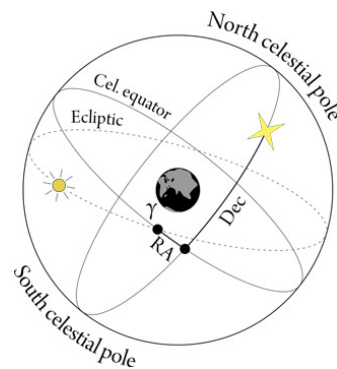


**Figure 2.4:** The equatorial coordinate system with vernal equinox  $\Upsilon$ , right ascension RA and declination Dec (Cesa 2020).

## 2.2.2 Galactic coordinate system

Whereas the equatorial coordinate system is best for an observer on Earth and cataloging the position of stars, it is not suited for studying the structure of the Galaxy. Therefore another appropriate coordinate system is needed, called the Galactic coordinate system (GCS) with the Sun in its center. In general the GCS is also a two dimensional spherical system with *Galactic longitude*  $l$  (from  $0^\circ$  to  $360^\circ$ ) and *Galactic latitude*  $b$  (from  $-90^\circ$  to  $90^\circ$ ), analogously defined as right ascension and declination. So  $l$  measures the angular distance of an object eastwards along the Galactic plane and  $b$  the angular distance of an object perpendicular to it (see Figure 2.5). The GCS can be derived from the ECS via coordinate transformation. So, for example, the Galactic center ( $l = 0^\circ$ ,  $b = 0^\circ$ ) has the equatorial coordinates  $\alpha = 266.40^\circ$  and  $\delta = -28.94^\circ$  and the Galactic plane is tilted against the celestial equator by  $62.6^\circ$ .

If also the distance  $d$  of an object to us is known, the Galactic coordinates ( $d$ ,  $l$ ,  $b$ ) can be transformed into three dimensional Cartesian coordinates via

$$\begin{pmatrix} x \\ y \\ z \end{pmatrix}_{\text{HC}} = d \cdot \begin{pmatrix} \cos l \cos b \\ \sin l \cos b \\ \sin b \end{pmatrix} \quad \text{or} \quad \begin{pmatrix} X \\ Y \\ Z \end{pmatrix}_{\text{GC}} = \begin{pmatrix} x - r_\odot \\ y \\ z \end{pmatrix}. \quad (2.1)$$

The indices HC and GC mean heliocentric (Sun in the origin) and galactocentric (Galactic center in the origin), respectively, and  $r_\odot = 8.33 \pm 0.35$  kpc (Irrgang et al. 2013) is the distance between the Sun and the Galactic center. The latter ones in Equation 2.1 are best for describing the Galaxy in the most general way and are also a good choice for kinematic studies within the Milky Way, like in this work. The direction  $X$  points from the Galactic center towards the sun,  $Y$  perpendicular to  $X$  in the Galactic plane and  $Z$  perpendicular to the Galactic plane, as shown in Figure 2.5.

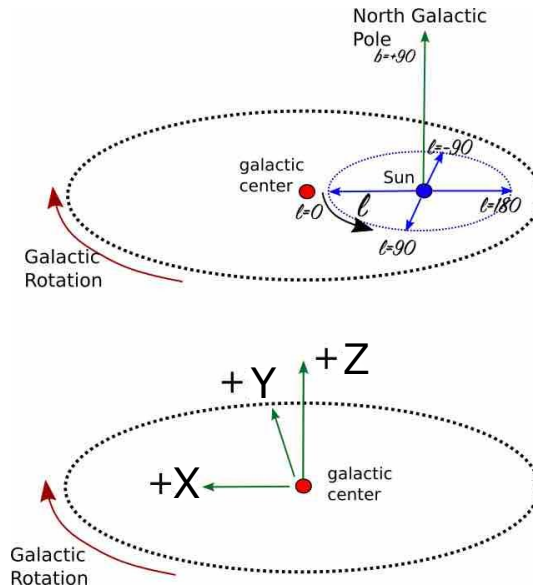


**Figure 2.5:** The Galactic coordinate system. Upper figure: Two dimensional heliocentric Galactic coordinates with longitude  $l$  and latitude  $b$ . Lower figure: Three dimensional galactocentric coordinates  $X$ ,  $Y$  and  $Z$  (de la Vega et al. 2015).

### 2.2.3 Distance measurements

As shown in Equation 2.1, the distance  $d$  of an object to us is crucial for obtaining the full three dimensional information of a star's position. Therefore, the question is, how distances can be determined in astronomy. The only direct way for that is measuring the annual parallax, what is just possible for close stars and with very precise telescopes. For further distant objects indirect ways have to be applied, for example calculating the distance from spectroscopic and photometric parameters. Both methods will be illustrated in the next two subsections.

#### Parallax inferred distances

The annual trigonometric parallax of a star is the apparent motion of it on the night sky for an observer on Earth, due to the Earth's rotation around the Sun (see Figure 2.6). Thus, the parallax angle  $p$  needs to be measured for at least half a year (the longer the observation time, the more precise the result). If the observed star is located exactly perpendicular to the Earth's orbit, the shape of the parallax will be circular. If the line of sight to the star lies within the ecliptic plane, one can observe a straight line as parallax. These are the most extreme cases and in general, however, the parallax will be elliptical.

With simple trigonometry and the small angle approximation, the distance  $d$  of an object can be inferred from the parallax angle  $p$  via

$$p \approx \tan p = \frac{1 \text{ AU}}{d} \quad \Leftrightarrow \quad d \approx \frac{1 \text{ AU}}{p}, \quad (2.2)$$

where  $1 \text{ AU} \approx 150 \times 10^9 \text{ m}$  is the radius of the Earth's orbit around the sun. Moreover, the astronomical length unit  $1 \text{ pc}$  (*parsec*, short for *parallax second*) is defined by the inverse value of a parallax angle  $p = 1 \text{ as}$ , given in arcseconds. A distance of  $1 \text{ pc}$  is equivalent to  $3.09 \times 10^{16} \text{ m} = 206\,265 \text{ AU} = 3.26 \text{ ly}$  and is often used with prefixes, like  $\text{kpc}$  (kiloparsec) or  $\text{Mpc}$  (megaparsec).

In general, the apparent motion of an object on the night sky is the superposition of the elliptical parallax motion and the linear proper motion (see subsection 2.2.4), resulting into a spiral trajectory as shown in Figure 2.7. Unfortunately, stars are often far away from us, which makes it hard to disentangle both from each other. Additionally, the parallax angle shrinks with  $1/d$ , so that even the extremely precise space telescope *Gaia* (see section 3.2) has a practical detection limit for the parallax of a few  $\text{kpc}$ . Therefore, another method is needed for obtaining reliable distances.

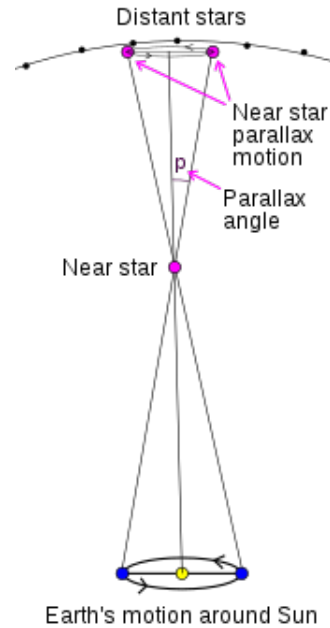


**Figure 2.6:** Definition of the trigonometric annual parallax angle  $p$  (Martin 2020).

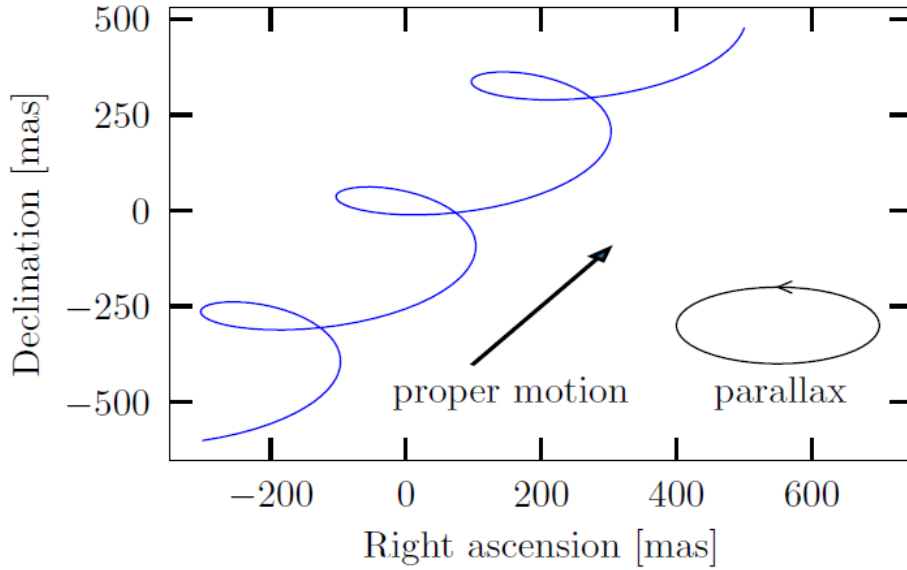


**Figure 2.7:** Superposition of the linear proper motion and the elliptical parallax motion of a star on the night sky (Dimpel 2018).

### Spectrophotometric distances

An indirect way is the calculation of distances based on spectroscopic and photometric quantities, called spectrophotometric distances. There, first of all, one needs to apply quantitative spectroscopy on stellar spectra to determine atmospheric parameters, that are the effective temperature  $T_{\text{eff}}$  and the surface gravity  $\log(g)$ . These can then be compared in a Hertzsprung-Russell or Kiel diagram to theoretical evolutionary tracks in order to derive stellar masses  $M$ . Since the angular diameter

$$\Theta = \frac{2R}{d} \quad \text{and the Radius} \quad R = \sqrt{\frac{GM}{g}}$$

of an object are given by simple trigonometry and Newton's law of gravity, respectively, the resulting formula for the spectrophotometric distance is

$$d_{\text{spectro}} = \frac{2}{\Theta} \sqrt{\frac{GM}{g}}. \quad (2.3)$$

Thereby  $G$  is the gravitational constant and the last missing parameter,  $\Theta$ , can be derived from comparing synthetic SEDs (spectral energy distributions) to photometric data.

The disadvantage of this method is, that on the one hand it costs considerable effort to determine all these parameters and on the other hand, if so much quantities are needed, all the single uncertainties are propagated to the final result. The advantage, however, is that it also works for distant objects, for which precise astrometry is unavailable.

### 2.2.4 Velocity components and proper motion

The velocity  $\vec{v}$  of celestial objects in space relative to us, which is essential for kinematic studies, is also a quantity, that can not be directly measured. So, first of all, its absolute value  $v$  must be split into two components, the *radial* velocity  $v_{\text{rad}}$  and the *tangential* velocity  $v_{\text{tan}}$  (see Figure 2.8):

$$v = |\vec{v}| = \sqrt{v_{\text{rad}}^2 + v_{\text{tan}}^2}. \quad (2.4)$$

The radial velocity of a star describes the motion along the line of sight, with a negative sign coming towards us and a positive sign moving away from us. It can be directly measured from the blue- or redshift of spectral lines in a stellar spectrum due to the electromagnetic Doppler effect. So, if the wavelength difference  $\Delta\lambda$  of a spectral line with respect to the true wavelength  $\lambda$  is given, the radial velocity turns out to be

$$v_{\text{rad}} = c \frac{\Delta\lambda}{\lambda}, \quad (2.5)$$

where  $c$  is the speed of light. If the examined star has a high surface gravity, it is important to correct its measured radial velocity for the gravitational redshift

$$v_{\text{grav}} = \frac{\sqrt{GMg}}{c} \quad (2.6)$$

induced by the star itself. For white dwarfs, for example, this can have an effect of some tens of  $\text{km s}^{-1}$ .

The tangential velocity can be calculated from the so-called *proper motion*  $\mu$  and the distance  $d$ . The proper motion, as shown in Figure 2.8, is the apparent angular motion of a star on the celestial sphere and is usually measured in  $(\text{m})\text{as yr}^{-1}$  by recording the position of a star at different times. It can also be divided into two components, the proper motion in direction of right ascension  $\mu_{\alpha}$  and the proper motion in direction of declination  $\mu_{\delta}$ . Altogether the tangential velocity is given by

$$v_{\text{tan}} = d \cdot \mu = d \cdot \sqrt{\mu_{\delta}^2 + \mu_{\alpha}^2 \cos^2 \delta}. \quad (2.7)$$

The correction term  $\cos^2 \delta$  accounts for the widening of the right ascension away from the equatorial poles, when the night sky is projected on a flat surface.

Now the velocity is given in equatorial coordinates. But it can also be transformed into three dimensional, cylindrical and heliocentric Galactic velocity components  $u$ ,  $v$  and  $w$  and then into galactocentric ones (see for example Johnson & Soderblom 1987):

$$\begin{pmatrix} U \\ V \\ W \end{pmatrix}_{\text{GC}} = \begin{pmatrix} u \\ v \\ w \end{pmatrix}_{\text{HC}} + \begin{pmatrix} U_{\odot} \\ V_{\odot} + V_{\text{LSR}} \\ W_{\odot} \end{pmatrix}. \quad (2.8)$$

$V_{\text{LSR}} = 242 \text{ km s}^{-1}$  is the  $V$ -velocity component of the local standard of rest (LSR) and  $U_{\odot} = 11.10 \text{ km s}^{-1}$ ,  $V_{\odot} = 12.24 \text{ km s}^{-1}$  and  $W_{\odot} = 7.25 \text{ km s}^{-1}$  are the velocity components of the Sun relative to the LSR (Irrgang et al. 2013). The coordinate system is cylindrical, since  $U$  is the radial velocity,  $V$  the velocity in direction of the Galactic rotation and  $W$  the velocity perpendicular to the Galactic plane.

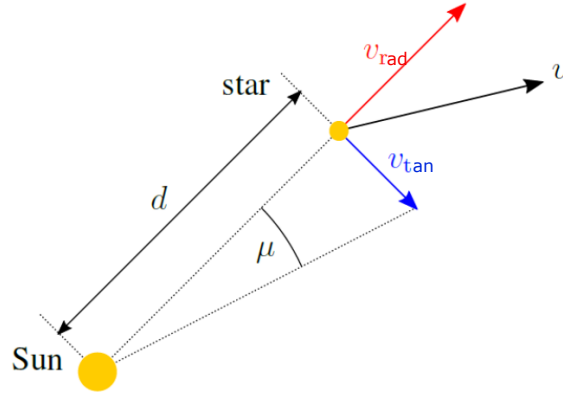


**Figure 2.8:** Definition of radial velocity and the proper motion (adapted from Dimpel 2018).

## 2.3 Different Galactic populations

Stellar kinematic parameters and chemical abundances tell us a lot about nature, formation and history of stars. Therefore all Galactic objects can be divided into three subgroups on the basis of these quantities. As shown in Figure 2.9, these subgroups are the *thin disk* population, the *thick disk* population and the *halo* population. Each of them and their individual photospheric chemical composition properties will be discussed in the following subsections.

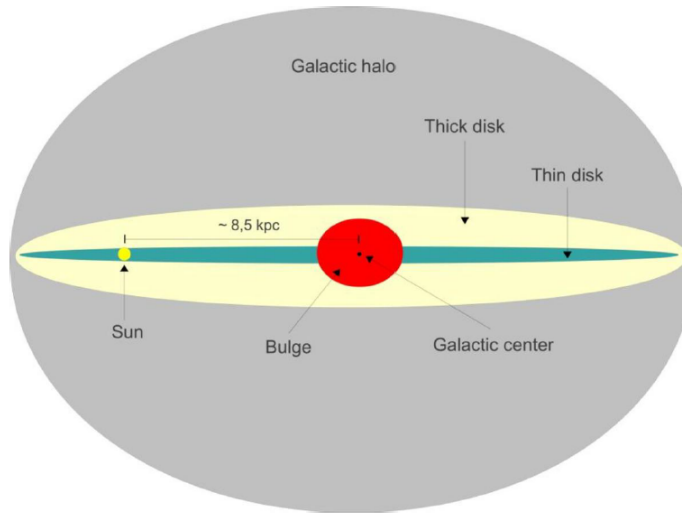


**Figure 2.9:** Schematic sketch of the Milky Way structure with the most important components and the position of the sun (taken from Kreuzer 2021).

### 2.3.1 Thin disk population

As its name says, the thin disk is the thinner part of the Galactic disk, rotating around the Galactic center on nearly circular orbits. Its members are closest to the Galactic plane. It has a radial scale length of  $h_R \approx 2.5 \text{ kpc}$  and a scale height of  $h_z \approx 100 - 400 \text{ pc}$ , depending on the age of the stellar classes. The population

consists of a wide spectrum of stars with different masses and ages and makes up the majority of the objects within the Galactic plane. Also star formation is going on and clusters of young, metal rich stars can be found. Thin disk stars have almost no  $W$ -velocity component perpendicular to the Galactic plane and follow the Galactic rotation, with a  $V$ -velocity of  $V \approx V_{\text{LSR}}$  and a high angular momentum on circular orbits. For example, the Sun belongs to the thin disk. The rest of the objects within the Galactic plane are either thick disk stars or halo stars currently passing through it.

### 2.3.2 Thick disk population

Thick disk stars are an old and metal poor disk population with a radial scale length of  $h_{\text{R}} \approx 3 \text{ kpc}$  and a scale height of  $h_{\text{Z}} \approx 1 \text{ kpc}$ , both larger than those of the thin disk. Almost no star formation is going on and hence, the thick disk is on average an older population compared to the thin disk. Thick disk stars can have not negligible  $W$ -velocity components perpendicular to the Galactic plane, on average lag behind the rotation of the thin disk and may also be on more eccentric orbits with lower angular momenta. Recent investigations have shown, that the thick disk comprises two distinct and overlapping stellar populations with different kinematic properties and chemical compositions (Carollo et al. 2019). They are called the metal weak thick disk (MWTD) and the canonical thick disk, but will be considered as single component in this work.

### 2.3.3 Halo population

The Galactic halo is a spherical component of the Milky Way surrounding the Galactic disk and ranging beyond 100 kpc. It is an old and metal poor population, consisting of globular clusters and also single BHB stars and BSs. Halo stars are not kinematically coupled to the Galactic rotation, which leads to very eccentric, chaotic and even retrograde orbits, which have trajectories in the opposite direction of the Galactic rotation and thus, have negative  $V$ -velocities. Therefore, the halo population has no net rotation and  $V$  is distributed symmetrically around zero velocity. Beside the visible stellar population, the Galactic halo also consists of the so-called dark matter halo. Its mass exceeds that of the stellar halo by far. As consequence, the mass of the halo stars does not contribute significantly to the gravitational potential of the halo (see section 2.4). Furthermore, the halo is not a single homogeneous structure, but consists of several substructures and streams, like Gaia-Enceladus, Sequoia, Thamnos, the Helmi streams and the Sagittarius streams (Helmi 2020). Many activities are going on at the moment to clarify the origin of these structures.

### 2.3.4 Metallicity and $\alpha$ -enhancement

In general, older and younger stellar populations can be distinguished by their metal abundances. The first stars, formed in the early universe, only had hydrogen and helium available as formation material. Such stars are called population III stars, but apparently do no longer exist, because no such objects have been found so far.

Metal poor stars have been found to be old and called population II stars. They may have formed from the first generation of stars. Younger stars, such as the Sun and called population I, are formed out of metal rich material produced by nuclear fusion in the progenitor generation of stars in the cosmic cycle of matter and ejected by supernova explosions and stellar winds. Hence, the old halo population can be decently separated from the younger disk population via spectroscopically measured chemical abundances.

First of all a word on chemical abundances in general: The abundance ratio

$$[X/Y] = \log\left(\frac{N_X}{N_Y}\right) - \log\left(\frac{N_X}{N_Y}\right)_\odot \quad (2.9)$$

is given as the logarithm of a star's number abundance compared to that of the Sun, where  $N_X$  and  $N_Y$  are the particle fractions of the respective elements X and Y. Hence, if a star contains the same fraction of elements X and Y as the Sun, the abundance ratio is zero, if it contains less, it is negative and if it contains more, it is positive. Because the iron abundance is easy to determine for most stars,  $[\text{Fe}/\text{H}]$  is used as a proxy for the overall metallicity of a star. In addition, old stellar populations show an enhancement of the so-called  $\alpha$ -process elements (O, Ne, Mg, Si, S, Ar and Ca) relative to the iron abundance, which were mainly produced by thermonuclear fusion of helium. So,  $[\alpha/\text{Fe}]$  is called the  $\alpha$ -enhancement and  $[\text{Mg}/\text{Fe}]$  is often used as proxy for it.

Therefore, the distinction between disk and halo populations can be done best in the  $[\text{Mg}/\text{Fe}]$  versus  $[\text{Fe}/\text{H}]$  diagram, as shown, for example, in Figure 2.10, since halo and thick disk stars possess a higher  $[\text{Mg}/\text{Fe}]$  ratio than thin disk stars. But if that is not possible, for instance for white dwarfs, which only show hydrogen or helium in their spectra, or for stars that exhibit strong atmospheric diffusion, one needs to rely on kinematic criteria. These criteria then first need to be calibrated by using a suitable calibration sample (see for example Pauli et al. 2006; Naidu et al. 2020). That is also the approach adopted in this work and will be described in more detail in chapter 4.

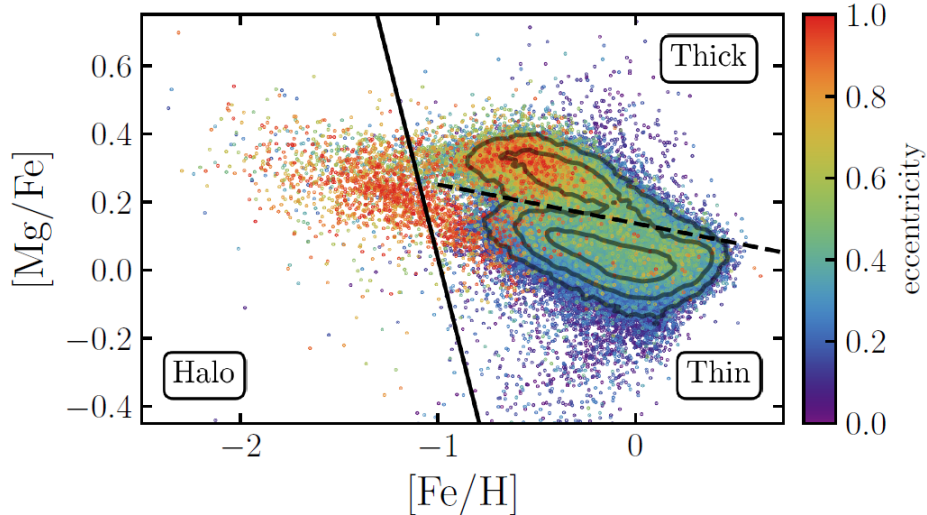


**Figure 2.10:**  $[\text{Mg}/\text{Fe}]$  versus  $[\text{Fe}/\text{H}]$  abundances for the APOGEE DR16 sample. Each star is color-coded by the eccentricity of its Galactic orbit, with higher eccentricity stars appearing above lower eccentricity stars. The solid line shows the separation between halo and disk stars. The dashed shows the separation between thin and thick disk stars. The grey contours show density in the more populated thin and thick disk sequences (taken from Lane et al. 2021).

## 2.4 The Milky Way gravitational potential

In order to model Galactic orbits and to derive orbital parameters, like the eccentricity, a Milky Way gravitational potential needs to be defined. Since the total mass and the shape of the density distribution within the Galaxy and especially the halo are still debated, there exist several attempts for doing so. In general, calculations are carried out using axis symmetric analytical approximations expressed in cylindrical coordinates with the common components  $r$  and  $z$ . The total gravitational potential  $\Phi$  is the sum of the single potentials for the bulge, the disk and the halo:

$$\Phi(r, z) = \Phi_b(r, z) + \Phi_d(r, z) + \Phi_h(r, z). \quad (2.10)$$

The published models of the Galactic potentials for the bulge and the disk are often very similar and just the potential of the dark matter halo differs considerably, since its true mass is not known and assumptions have to be made. The impact of the single potential components on the orbital velocity of stars as function of the radius from the Galactic center is shown in Figure 2.11. It can be seen that the potential for the supermassive black hole in the center of the Milky Way is, in general, negligible for the total gravitational potential and plays only a role for the innermost region of the bulge ( $\sim 30$  pc).

One commonly used potential is that from Allen & Santillan (1991), updated with recent observations by Irrgang et al. (2013) and will also be used in this work for orbit calculations.

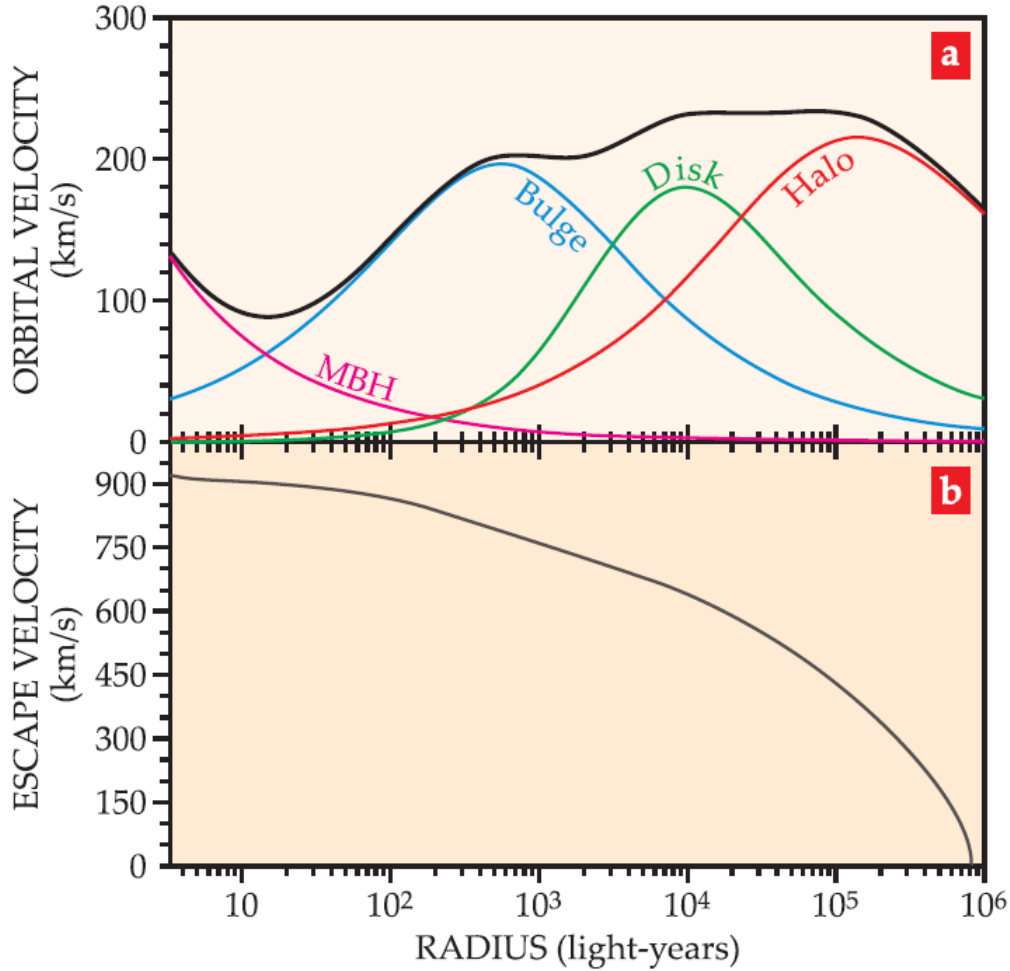


**Figure 2.11:** Gravity links the circular orbital velocity of stars to the mass distribution in the Milky Way. Upper panel: Impact of the Galaxy’s four major mass components, the supermassive black hole (MBH), the bulge, (thin and thick) disk and (dark matter) halo on the orbital velocity of stars as function of the radius from the Galactic center. Lower panel: Approximate escape velocity of the Milky Way as function of the radius from the Galactic center (Brown 2016).

With the prescription of the Milky Way gravitational potential and the six dimensional phase space  $(X, Y, Z, U, V, W)$  as initial condition, the equation of motion for the orbits of stars can numerically be solved (see for example Odenkirchen & Brosche 1992). Then other kinematic parameters can be obtained from the trajectories. Finally, individual stars can be assigned to the thin disk, thick disk and halo based on a parameter-based classification scheme.

## 3 Telescopes and Instruments

No modern experimental science is possible without sophisticated technical devices. Especially for astronomers, different light collecting instruments are needed for revealing the faintest objects of the universe. These instruments are, for example, optical telescopes, which can be called the “eyes” of modern astronomers. However, to work accurately, telescopes require very faint surroundings and good weather conditions on site. That is the reason why remote and desert-like locations are favoured for building them up. Also high elevations are preferred to minimize the impact of the Earth’s atmosphere, for instance the effects of telluric absorption and seeing. The latter one is an astronomical expression for turbulences in the atmosphere, which result in flickering of the stars and can be seen in a clear night even with the naked eye. Although some rare places on Earth have been found, which are suited for building up telescopes, these effects can never be fully neglected. The only location where all of them vanish, is in space. So a lot of effort is put into inventing astronomical instruments to let them work from there. But whereas ground-based telescopes can be very large and developed at the edge of what is technically possible, for example by using adaptive optics to overcome the seeing limitations, spacecrafts need to be smaller, since it is a very challenging task to send big and heavy instruments into space and operate them.

In this work all stars are taken from the MMT sample to carry out a kinematic analysis. So the spectra of these objects were recorded by the Multiple-Mirror-Telescope (MMT) and have been already analysed in previous studies. This data is then complemented with *Gaia* EDR3 astrometry. Both, the MMT HVS survey and the *Gaia* space mission, will be briefly discussed in the next sections.

### 3.1 The MMT HVS survey

In the early 1960s, out of several locations, Mount Hopkins in Arizona, USA, has been chosen for building up the Fred-Lawrence-Whipple-Observatory, because of its high elevation of 2616 m and mostly clear skies (MMTO 2022). The original purpose of the site was a NASA program for tracking satellites equipped with retroreflectors from Earth by using laser systems in 1964. But then the director of the Smithsonian Astrophysical Observatory (SAO), Fred L. Whipple, realized that the location might be a good place for an advanced astronomical telescope. So in the beginning, it consisted of six single 1.8 m mirrors, which were combined to an array, resulting into an effective light collecting area equivalent to a 4.5 m mirror. Each mirror had its own secondary mirror and the telescope was called the Multiple-Mirror-Telescope (MMT). This setup had first light in 1979 and was operational until 1998. Then the telescope received a major upgrade, where the single mirrors were replaced by a 6.5 m monolytic primary mirror. Therefore, the name MMT is no longer an acronym.

The new setup had first light in May 13, 2000, and is operational until today. Both configurations are shown in Figure 3.1.

The MMT blue channel spectrograph, with which the spectra of the stars investigated in this work were recorded, offers a variable resolution between  $R = 740$  and  $R = 3830$ , depending on the grating (MMTO 2022). Here grating #832 (lines/mm) was taken with a theoretical resolution of the maximum value  $R = 3830$  at the blaze wavelength of  $3900 \text{ \AA}$ . It provides a wavelength coverage from  $3570 \text{ \AA}$  to  $4520 \text{ \AA}$ .



**Figure 3.1:** *Left:* Former MMT with six single 1.8 m mirrors. *Right:* Today's configuration with a 6.5 m mirror (MMTO 2022).

Brown et al. (2003) started a spectroscopic survey of faint blue and mostly halo stars, whose spectra were recorded with the MMT. After the first serendipitous discoveries of hyper-velocity-stars (HVSs), which are stars unbound to the Galaxy, a systematic search for them has been triggered. So this survey is called the MMT HVS survey and was completed in 2014 (Brown et al. 2014). A Kiel diagram for the whole sample is shown in Figure 2.2. It consists of 1897 individual objects, which are mainly BHB stars, BSs and WDs.

## 3.2 The *Gaia* space mission

The *Gaia* space mission (Gaia Collaboration et al. 2016) is a very ambitious mission of the European Space Agency (ESA) and it is the follow-up mission of HIPPARCOS. The *Gaia* satellite (Figure 3.2) was launched on December 19, 2013, and arrived a few weeks later at its place of operation near the second Lagrange point L2 of the Sun-Earth-Moon system, about 1.5 million kilometres away from us. It moves on a Lissajous orbit of a 6.3 years period, which is shown in Figure 3.3, and was designed to fulfill its duty in five years, so the nominal mission ended on July 17, 2019. But fortunately, it is still working and is, hence, already in the extended mission, which is expected to operate until 2025.

The original goal of *Gaia* was to provide positions, proper motions, parallaxes and photometry for over one billion objects within the Milky Way and the Local Group with unprecedented precision. This aim was already achieved with the second data release on April 25, 2018, called *Gaia* DR2, which provides astrometric and

photometric data for 1.3 billion stars (Gaia Collaboration et al. 2018). But since *Gaia* is able to collect data for even more objects and the precision of its astrometry increases with increasing measurement times, it is still operating.

Up to now another data release has been published with data for approximately 1.8 billion objects. This third data release has been split into two parts. The astrometric and photometric measurements have been published on December 3, 2020, as an early data release, called *Gaia* EDR3 (Gaia Collaboration et al. 2021), while the full set of *Gaia* DR3 was published on June 13, 2022. Here we make use of the EDR3 data.

Since the analysis of the MMT HVS survey in Brown et al. (2014) suffered a few ambiguities, Kreuzer (2021) revisited the sample for combining MMT spectroscopy with *Gaia* DR2 astrometry and carried out a more sophisticated analysis. This led, for example, to a clear distinction between the blue horizontal branch and blue straggler population within the sample, what was not reliably possible before. Kreuzer (2021) had to use *Gaia* DR2 data, but because *Gaia* EDR3 astrometric data is available now, it appears worthwhile to redo the kinematic analysis in Kreuzer (2021), which is the aim of this work.

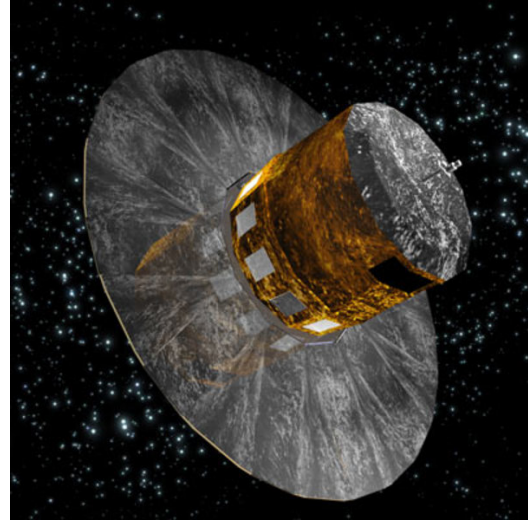


**Figure 3.2:** Picture of the *Gaia* satellite (Universität Heidelberg 2022).

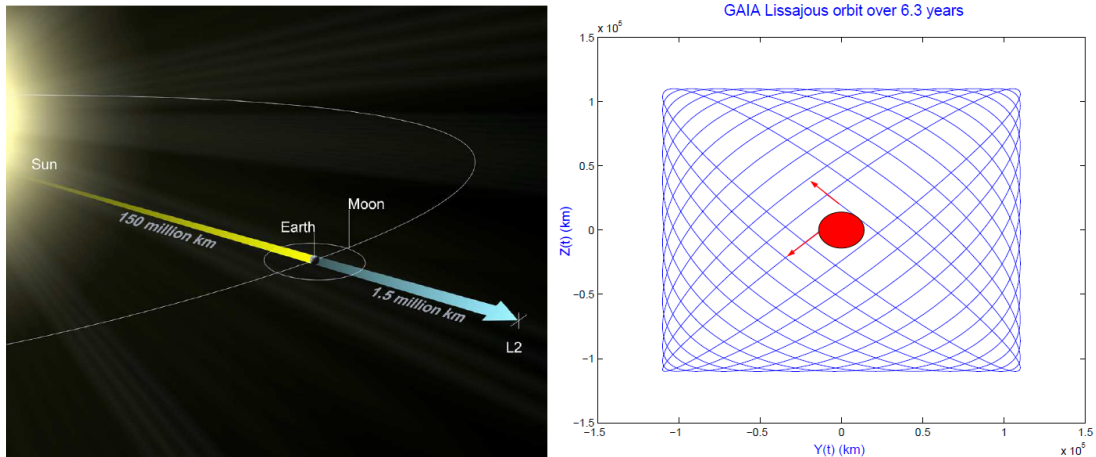


**Figure 3.3:** Second Lagrange point L2 as place of operation for the *Gaia* satellite and its Lissajous orbit with a period of 6.3 years (Mignard 2009).

## 4 Methods and Tools

The main aspect of the kinematic analysis in this work is the assignment of stars to the respective Galactic population, that is the thin disk, the thick disk and the halo. Therefore, a reliable classification scheme is needed and the one used here, is an extended version of the scheme invented by Pauli et al. (2003, 2006), which will be described in the next section before proceeding to the extended one developed in this work.

### 4.1 Previous classification scheme

Pauli et al. (2006) presented a sample of 398 DA white dwarfs from the SPY project (ESO SN Ia Progenitor survey). Since it is not possible for white dwarfs to distinguish their population membership via metallicities, it was necessary to rely on kinematic criteria. In order to do that, a calibration sample of 291 F and G main sequence stars has been used, for which the metal abundances were known from previous investigations.

Thin disk, thick disk and halo populations can be distinguished best in a  $[\text{Mg}/\text{Fe}]$  versus  $[\text{Fe}/\text{H}]$  diagram according to their positions, as shown for the calibration sample of main sequence stars in Figure 4.1. The classification in Pauli et al. (2006) has been carried out as follows:

<b>Halo</b>	→	$[\text{Fe}/\text{H}] < -1.05$	
<b>Thick disk</b>	→	$-1.05 \leq [\text{Fe}/\text{H}] \leq -0.30$	and $[\text{Mg}/\text{Fe}] \geq 0.3$
<b>Thin disk</b>	→	$-0.30 < [\text{Fe}/\text{H}]$	and $[\text{Mg}/\text{Fe}] \leq 0.2$

Stars in the overlapping region between thin disk and thick disk (open triangles) were omitted to ensure a clear distinction between the two disk populations, as well as the four stars in the halo region marked with open boxes, which probably belong to the metal weak thick disk, as their kinematics are incompatible with a halo membership.

A classical kinematic diagram is the  $U - V$ -velocity diagram. Therefore, Pauli et al. (2006) calculated the respective mean values and standard deviations of the  $U$ - and  $V$ -velocity components for the thin disk and thick disk stars of the calibration sample. These are listed in Table 4.1 and needed for calculating the respective population contours, as they are its centers. So, as it can be seen in the  $U - V$ -diagram (Figure 4.2) for the calibration sample, indeed almost all thin disk stars lie within the  $3\sigma_{\text{thin}}$ -contour and all halo stars are located outside the  $3\sigma_{\text{thick}}$ -contour.

The second kinematic diagram used by Pauli et al. (2006) for the classification is the  $J_z - e$ -diagram, which links two important orbital parameters, the  $Z$ -component of the angular momentum  $J_z$  and the eccentricity  $e$ . The latter one was derived from calculated stellar orbits and the diagram for the calibration sample is shown in

**Table 4.1:** The mean values and standard deviations for the  $U$ - and  $V$ -velocity components of the thin and thick disk stars of the calibration sample from Pauli et al. (2006).

Population	$\langle U_{\text{ms}} \rangle$ (km s $^{-1}$ )	$\sigma_{U_{\text{ms}}}$ (km s $^{-1}$ )	$\langle V_{\text{ms}} \rangle$ (km s $^{-1}$ )	$\sigma_{V_{\text{ms}}}$ (km s $^{-1}$ )
Thin disk	3	35	215	24
Thick disk	-32	56	160	45

Figure 4.3. The thin disk, thick disk and halo populations can be distinguished well in this diagram by three different regions, called region A, B and C, respectively. Region A has a triangular shape, is located at low eccentricities, but high angular momenta and contains most of the thin disk stars. The majority of thick disk stars, however, lies in region B, which is a box extended towards lower angular momenta and higher eccentricities. Halo stars are scattered in region C at very high eccentricities close to one and even lower angular momenta, which can also be negative, if the star is on a retrograde orbit. Although the distinction seems to be very clear, there is a little contamination of thick disk stars in region A and of thin disk stars in region B. Thus, the  $J_Z - e$ -diagram can not be used alone for the classification.

The third and last criterion used by Pauli et al. (2006) is the shape of the orbits, which were also calculated for the Galactic potential from Allen & Santillan (1991). This can be evaluated best in a meridional plot, where the motion perpendicular to the Galactic plane ( $Z$ -direction) is plotted against the radial position  $\rho = \sqrt{X^2 + Y^2}$ . Typical thin disk, thick disk and halo orbits are shown in Figure 4.4. Thin disk stars have very plane orbits with almost no extension in  $Z$ -direction and a low variation of  $\rho$ , because of their low eccentricities. For thick disk stars, however, the extensions of both parameters are significantly larger, but the orbits still show a high regularity. That is not the case for halo stars. Their orbits can strongly vary in both directions, be very chaotic and irregular and even come close either to the Galactic center or the outer parts of the Galaxy.

According to the method of Pauli et al. (2006), every star is now classified with the help of the three criteria, its position in the  $U - V$ -diagram, its position in the  $J_Z - e$ -diagram and the orbital behavior in the  $Z - \rho$ -diagram. Each criterion has a classification variable  $c_{UV}$ ,  $c_{J_Z e}$  or  $c_{\text{orb}}$  assigned, which is +1 if it shows the characteristics of a respective population and -1 if it doesn't. Then, if the sum

$$c = c_{UV} + c_{J_Z e} + c_{\text{orb}}$$

is larger or equal to 1 for a an individual star, it is assigned to the respective population. So, for example, if  $c \geq 1$  for the halo criteria, it is assigned to the halo. If  $c \geq 1$  for the thick disk criteria, it is assigned to the thick disk. If it is assigned neither to the halo nor to the thick disk, it is assigned to the thin disk.

This classification scheme was applied on the 398 SPY white dwarfs, resulting into an amount of 91% thin disk, 7% thick disk and 2% halo stars.

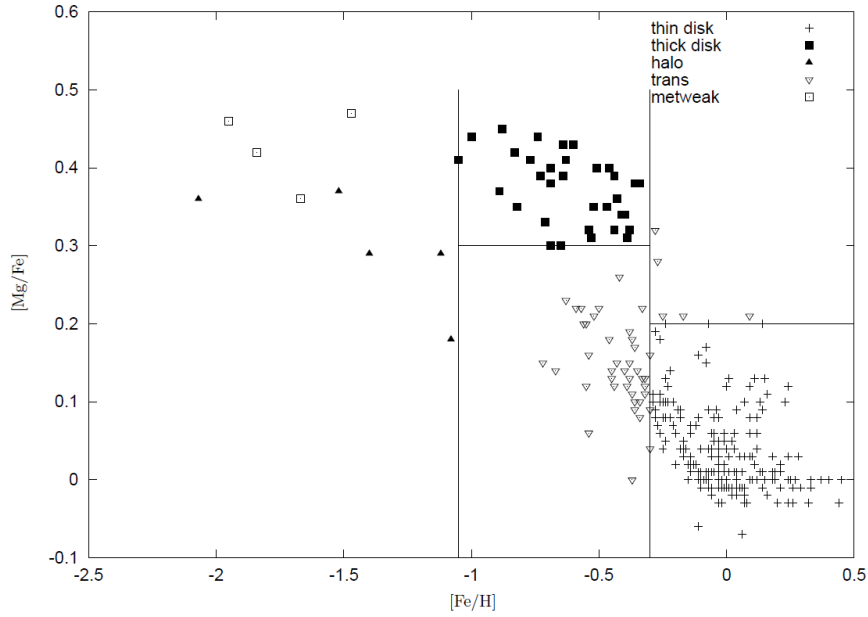


**Figure 4.1:**  $[\text{Mg}/\text{Fe}]$  vs.  $[\text{Fe}/\text{H}]$  abundance diagram for the calibration sample of main sequence stars. Distinction between thin disk stars (crosses), thick disk stars (filled boxes) and halo stars (filled triangles). Stars in the overlapping region between thin disk and thick disk (open triangles) and probable metal weak thick disk members (open boxes) are shown in the diagram, but were neglected for the calibration to ensure a clear distinction between population memberships (Pauli et al. 2006).

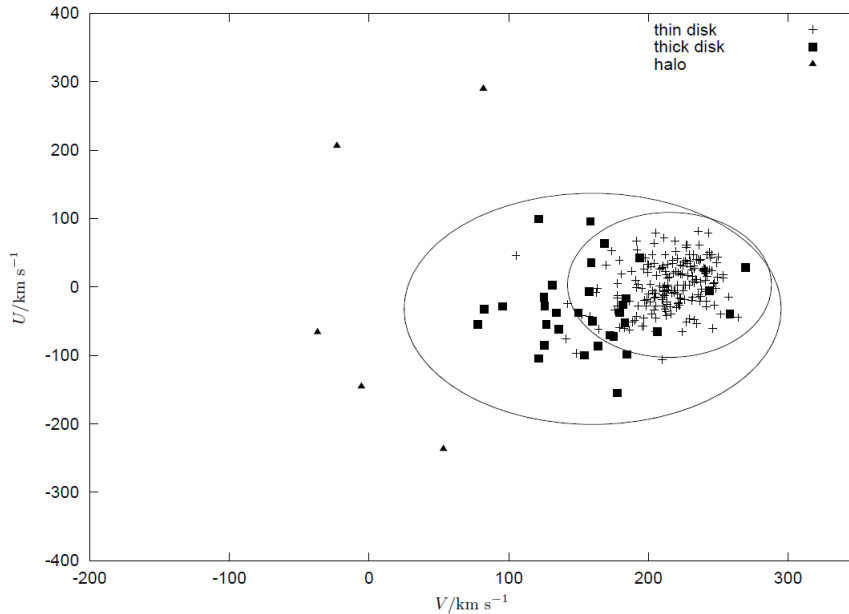


**Figure 4.2:**  $U - V$ -velocity diagram for the calibration sample of main sequence stars (Pauli et al. 2006).

## 4.1 Previous classification scheme

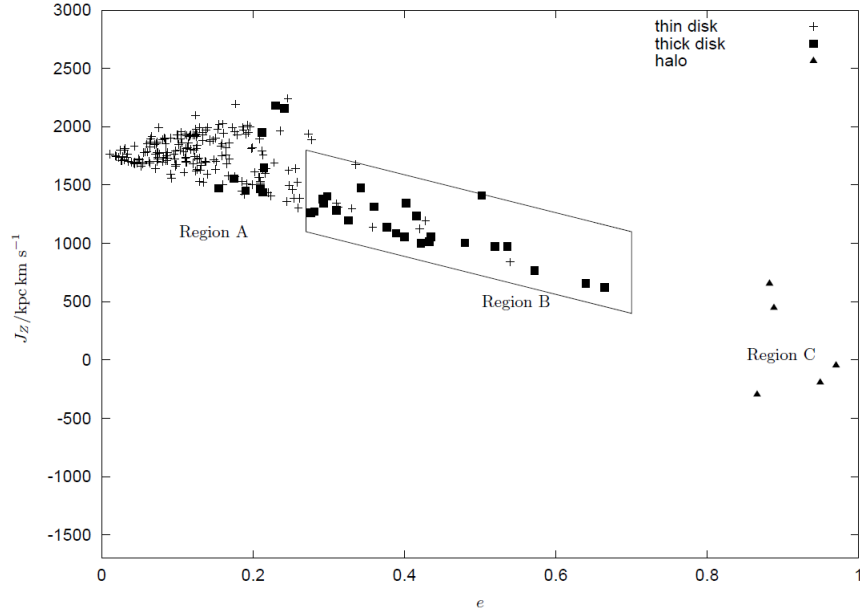
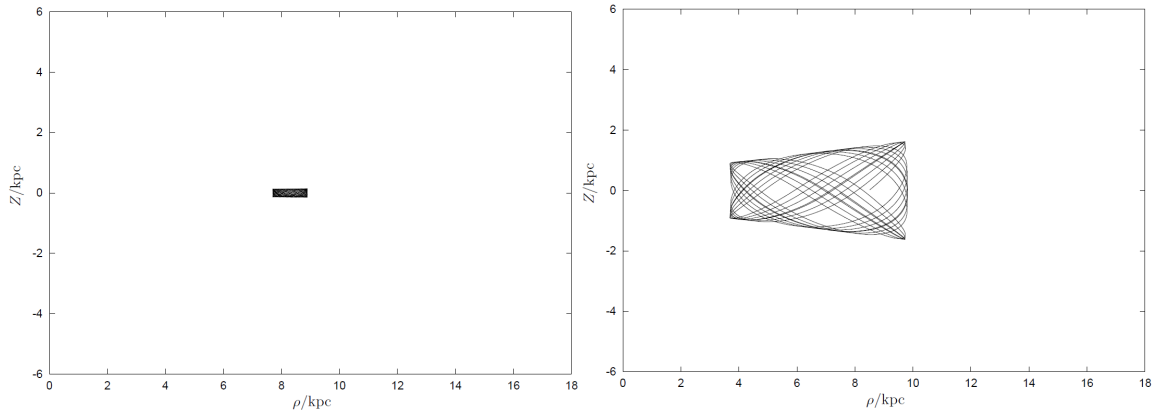
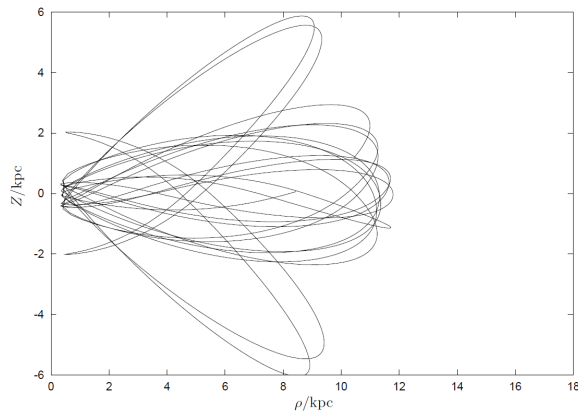


**Figure 4.3:**  $J_z - e$ -diagram for the calibration sample of main sequence stars (Pauli et al. 2006).



(a) Typical thin disk orbit.

(b) Typical thick disk orbit.



(c) Typical (chaotic) halo orbit.

**Figure 4.4:** Shapes of typical orbits for the respective populations (Pauli et al. 2006).

## 4.2 The extended classification scheme

The classification scheme in this work builds upon that from Pauli et al. (2006), but with some updates and extensions. Therefore, the first difference is that the much larger calibration sample from Anguiano et al. (2020) has been used, including a total of 270324 stars from the APOGEE (**A**pache **P**oint **O**bservatory **G**alactic **E**volution **E**xperiment) survey. The chemical classification for these stars is shown in Figure 4.5 and leads to the mean values and standard deviations for the velocity components of thin disk, thick disk and halo listed in Table 4.2. These slightly differ in comparison to the values adopted by Pauli et al. (2006), what is not surprising, since the sample of Anguiano et al. (2020) is round about 930 times larger and hence, provides more precise results. The classification in Anguiano et al. (2020) has been executed as follows:

<b>Halo</b>	→	$[\text{Fe}/\text{H}] < -1.0$
<b>Thick disk</b>	→	$-1.0 < [\text{Fe}/\text{H}] < 0.0$ and $+0.18 < [\text{Mg}/\text{Fe}] < +0.40$
<b>Thin disk</b>	→	$-0.7 < [\text{Fe}/\text{H}] < +0.5$ and $-0.10 < [\text{Mg}/\text{Fe}] < +0.17$

**Table 4.2:** The mean values  $\mu$  and standard deviations  $\sigma$  for the velocity components of thin disk, thick disk and halo from the calibration sample of Anguiano et al. (2020).

Population	$U$	$\sigma_U$	$V$	$\sigma_V$	$W$	$\sigma_W$
Thin disk	-0.52	37.61	229.43	25.01	0.02	18.63
Thick disk	-3.04	64.68	191.40	40.10	0.02	43.60
Halo	-2.90	165.50	-2.30	95.10	-5.00	94.10

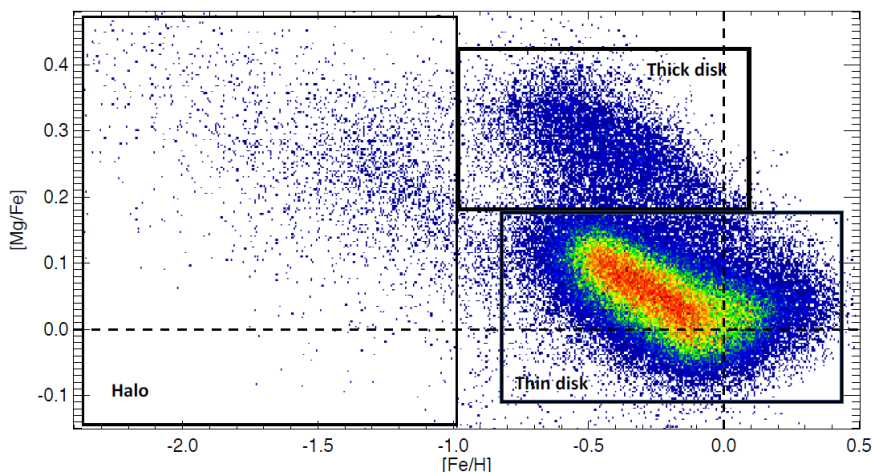


**Figure 4.5:** The distribution of  $[\text{Mg}/\text{Fe}]$  with  $[\text{Fe}/\text{H}]$  abundances for a sample of stars from the APOGEE survey. The color code indicates stellar density, where red shows the highest density and blue the lowest. The dashed lines show the solar values for reference (Anguiano et al. 2020).

Another advantage is that also values for the  $W$ -velocity component, as well as all three components for the halo are given. This allows to calculate halo contours and

not only to use the  $U - V$ - and  $J_Z - e$ -diagram for the kinematic classification, but also other velocity combinations like  $W - U$ ,  $W - V$ , the so-called Toomre-diagram, where  $\sqrt{U^2 + W^2}$  (motion perpendicular to the Galactic rotation) is plotted over  $V$ , and  $E_{\text{kin}} \equiv U^2 + V^2 + W^2$  over  $V$ . All diagrams with the respective  $3\sigma$  population contours can be seen for the MMT WD sample in section 5.3, for the MMT BHB sample in section 6.3 and for the MMT BS sample in section 7.3.<sup>1</sup>

Since the orbits of stars can often uniquely reveal their population membership (Figure 4.4), they are an important aspect for the classification. Therefore, they were calculated for all investigated stars in this work by using the code developed in Irrgang (2014), based on the Milky Way gravitational potential from Allen & Santillan (1991) updated with recent observations by Irrgang et al. (2013). The stellar trajectories were followed for ten revolutions around the Galactic center or for a maximum of 15 Gyr backwards in time. Uncertainties on the output parameters were estimated by using a Monte Carlo calculation with 50 000 samples. From the resulting orbits, quantities like eccentricity  $e$ , maximum distance in  $Z$ -direction from the Galactic plane  $z_{\text{max}}$  and total energy  $E_{\text{tot}}$  for stars were derived.

The classification of this work is based on the positions of stars in the  $U - V$ -,  $W - U$ -,  $W - V$ -,  $L_Z - e$ -,  $\sqrt{U^2 + W^2} - V$ - (Toomre) and  $E_{\text{kin}} = (U^2 + V^2 + W^2) - V$ -diagram and on the shape of the orbits (similar criteria are, for instance, used in Altmann et al. (2004) and in Martin et al. (2016)). For all of the kinematic diagrams  $3\sigma$  population contours are calculated and then evaluated, if a star lies only in the thin disk contour, only in the thick disk contour or only in the halo contour in the respective diagrams. Subsequently, it is counted how often a star lies within which contour, resulting into a score for each population ranging up to a value of six. So, for example, if a star lies three times within a thin disk contour, two times within a thick disk contour and once within a halo contour, it gets assigned a thin-disk-score of three, a thick-disk-score of two and a halo-score of one. Objects even lying outside the halo contour are considered as halo members, consistent with Pauli et al. (2006), where all stars lying outside the thick disk contour are regarded as halo objects. So the sum of the three scores is always six.

A complication in the interpretation of those diagrams arise from overlapping regions, in which an unambiguous identification is not possible. Therefore, the shape of the individual Galactic orbits is important, as pointed out by Pauli et al. (2006) and Altmann et al. (2004). In this work it is quantitatively taken into account by using the parameter  $z_{\text{max}}$ . So a star is most likely a thin disk member if  $z_{\text{max}} \leq 1$  kpc, most likely a thick disk member, if  $1 \text{ kpc} < z_{\text{max}} \leq 5$  kpc and most likely a halo member, if  $z_{\text{max}} > 5$  kpc (Gilmore & Reid 1983). The contamination of stars from neighbored populations is expected to be less for this criterion than the contamination due to the overlapping population contours in the kinematic diagrams (especially for those including  $V$ ). Therefore, on the one hand the  $z_{\text{max}}$ -value gets assigned another point for the population scores, so that they are ranging up to seven now, and on the other hand it is used as counter check for the overall scores (see following classification scheme or Figure 4.6). In Figure 5.8 a histogram of the

---

<sup>1</sup> Note that there are some changes in the  $L_Z - e$ -diagrams in comparison to Pauli et al. (2006). First of all the symbol  $J_Z$  for the angular momentum is exchanged by  $L_Z$ . The reason for that is, that the letter  $J$  is more common for the orbital actions than for the angular momentum. Furthermore,  $3\sigma$ -contours for the thin and thick disk have been calculated by transferring them from the velocity diagrams to the  $L_Z - e$ -diagram instead of using the empirical boxes from Pauli et al. (2006).

$z_{\max}$ -values for the WDs is shown, in Figure 6.4 for the BHB stars and in Figure 7.4 for the BSs. These underline the difference of  $z_{\max}$  between disk dominated samples (like the WDs) and halo dominated samples (BHB stars/BSs), which makes it reasonable to use it for the classification.

The classification scheme based on the three population scores and the orbits is as follows:

$$\begin{aligned}
 \text{Thin disk} &\rightarrow \text{thin-disk-score} \geq 5 \quad \text{and} \quad z_{\max} \leq 1 \text{ kpc} \\
 \text{Thick disk} &\rightarrow \text{thick-disk-score} \geq 2 \quad \text{and} \quad 1 \text{ kpc} < z_{\max} \leq 5 \text{ kpc} \\
 \text{Halo} &\rightarrow \text{halo-score} \geq 2 \quad \text{and} \quad z_{\max} > 5 \text{ kpc} \\
 &\quad \text{or} \quad z_{\max} > 10 \text{ kpc} \quad \text{or} \quad V < 0 \text{ (retrograde orbit)}
 \end{aligned}$$

If a star is still unassigned to any population due to this scheme, which is the case, when the scores are uniformly distributed or the orbits do not match with the maximum of the score, it is said, that if the thin-disk-score is larger than the sum of the thick-disk-score and the halo-score, it is assigned to the thin disk and if it is smaller, it is assigned to the thick disk. The star is never classified as halo member, since it is unlikely that a true halo object shows thin and thick disk characteristics at several points. This will always work, because the sum of the scores is odd. The whole classification scheme is summarized in Figure 4.6.

The orbits are used twice for the classification, which means they are somehow double weighted. Thus, one could say the importance of the  $z_{\max}$ -value of the orbits is overemphasized. But that is not true, because it is very unlikely that, for example, a thin disk star can be found at a distance of several kpc above the Galactic plane or a halo star always stays close to it. Furthermore, the orbits are always verified by the respective population score and vice versa. Hence, it can be said the combination of score and orbit is interlocking very well.

With a needed thin-disk-score of at least five, thin disk stars are classified stricter than thick disk and halo stars. The reason is that they are expected to deviate only little from their average characteristics. So true thin disk stars will most likely neither lie outside of any thin disk contour in the kinematic diagrams nor show irregular orbits with a high  $z_{\max}$ -value. Thick disk and halo characteristics, however, can deviate more strongly and therefore, stars are already assigned to the respective population, if the score equals at least two. This behavior can also be seen for the standard deviations of the mean velocity components in Table 4.2. In combination with the orbits the classification of thick disk and halo stars is very reliable.

Sets of all kinematic diagrams are shown for the WDs in Figure 5.9, for the BHB stars in Figure 6.5 and for the BSs in Figure 7.5.

Although the classification scheme is based on empirical experiences and does not contain any statistical refinements, as they can be found in more sophisticated ones, it can be considered as improvement to that from Pauli et al. (2006). Several more kinematic diagrams have been used, as well as the orbits of stars in a less subjective way. Also the problem of possibly missclassified objects due to the overlap of the population contours has been drastically reduced by including the  $z_{\max}$ -value of the orbits. Overall it can be said the classification is simple, but still robust and efficient.

## 4.2 The extended classification scheme

---

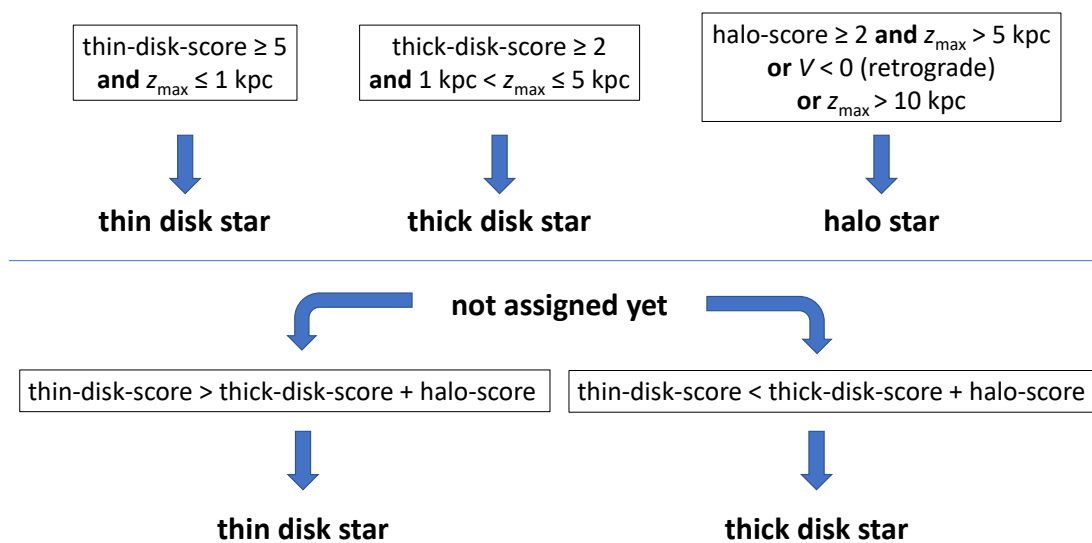


**Figure 4.6:** Schematic of the classification scheme.

# 5 White Dwarfs in the MMT sample

The MMT WD sample consists of 401 single white dwarfs with surface gravities  $\log(g) < 6.0$ , which make up more than 20% of the whole MMT HVS survey. So the question is, why these stars appear in a survey not meant to search for white dwarfs, but to find runaway or even hyper-velocity-stars. This is explained in Kreuzer (2021) due to the photometric selection criteria for the MMT HVS survey and typical photometry uncertainties. Kreuzer (2021) crossmatched the MMT WD sample with other white dwarf catalogs, revealed 101 yet unknown WDs and spectroscopically confirmed 166 WDs, previously only listed as candidates. Hence, it appears worthwhile to repeat the kinematic analysis of this sample. Since WDs are intrinsically faint objects and can be observed only in a small volume around us ( $d \lesssim 1$  kpc), it is not easy to investigate the Galactic halo WD population. Therefore, the kinematic analysis of the MMT WD sample will focus on finding possible halo candidates, which might be only accessible, if they are currently passing through the Galactic disk.

First of all, the previous findings of Kreuzer (2021) for the WDs will be summarized in section 5.1 and then the astrometric data of *Gaia* DR2 will be compared to that of EDR3 in section 5.2 to see how it changed. Thereafter, the kinematic analysis will be carried out in section 5.3, followed by a discussion of the found halo candidates in section 5.4.

## 5.1 Previous findings

Kreuzer (2021) carried out a comprehensive analysis of the MMT WD sample. So with the help of theoretical models and grids he derived atmospheric parameters for the WDs, such as the effective surface temperatures  $T_{\text{eff}}$  and surface gravities  $\log(g)$ . These could then be plotted in a Kiel diagram together with theoretical evolutionary tracks (Figure 5.1) for determining masses by a simple interpolation routine. The resulting mass distribution is shown in Figure 5.2 together with two fitted Gaussian kernels. Despite the lower number of white dwarfs and the description by single Gaussians, which is probably not optimal, the two peaks at 0.388 and 0.554 solar masses are in good agreement with comparable published investigations (for details see Kreuzer 2021).

From  $T_{\text{eff}}$ ,  $\log(g)$ , the masses  $M$  and the angular diameter  $\Theta$  (derived from photometric fits to synthetic SEDs) Kreuzer (2021) then calculated spectrophotometric distances for the WDs, following the approach described in subsection 2.2.3. These were then compared to the *Gaia* DR2 parallax inferred distances from Bailer-Jones et al. (2018) in Figure 5.3. In general there is a good agreement, especially for close-by objects. Kreuzer (2021) found only eight stars to be much closer ( $d \lesssim 100$  pc) according to the spectrophotometric distances in comparison to the parallax inferred

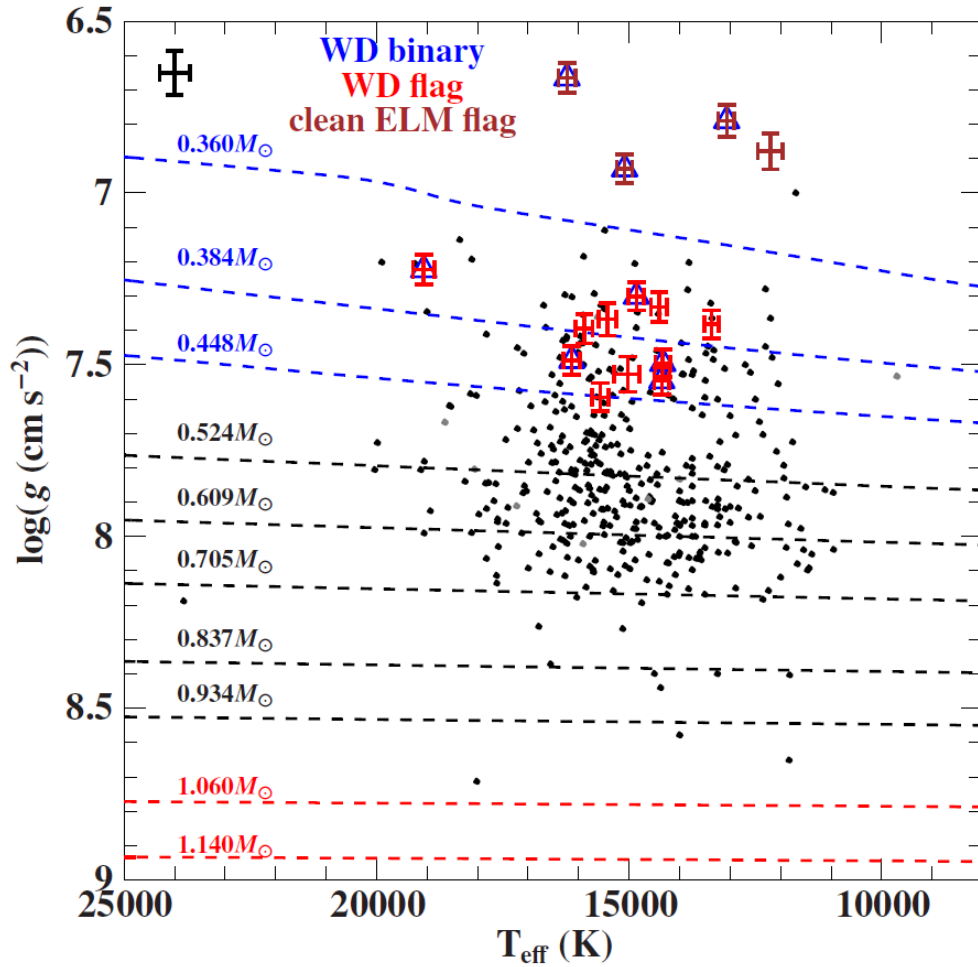


**Figure 5.1:** Positions of all WDs in a Kiel diagram with overplotted evolutionary tracks and flags for binaries (blue triangles), clean ELM objects (brown errorbars) and WDs (red errorbars). Gray dots may indicate possible light contamination by close-by objects. Median uncertainties are plotted in the top left corner (taken from Kreuzer 2021).

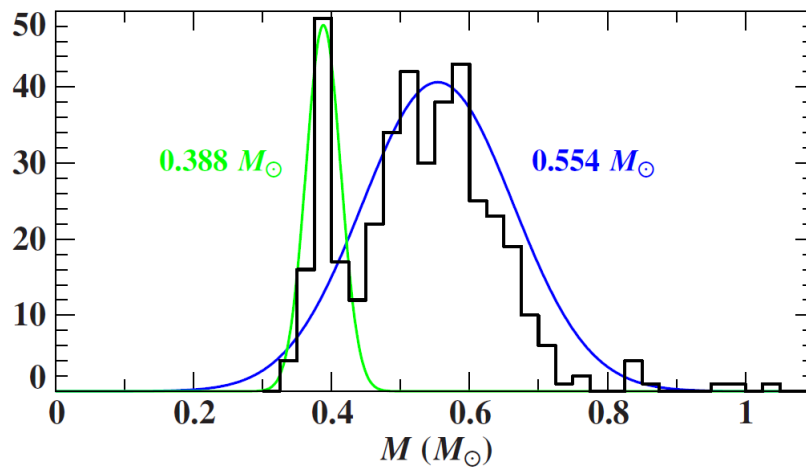


**Figure 5.2:** Histogram of masses  $M$  for all MMT WDs (taken from Kreuzer 2021).

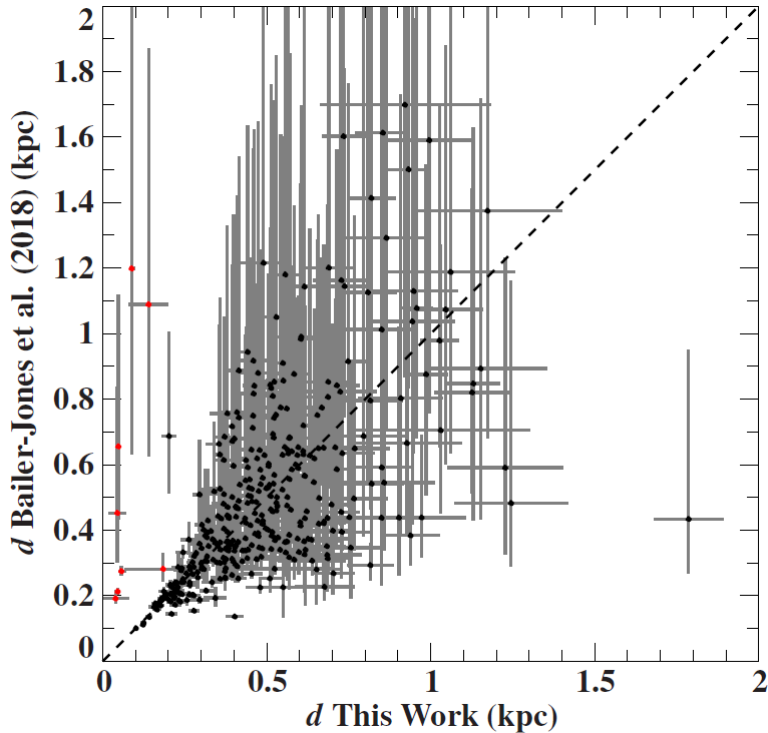


**Figure 5.3:** Comparison of the measured spectrophotometric distances to the distances inferred from *Gaia* DR2 parallaxes by Bailer-Jones et al. (2018). The dashed line is the identity relation. Highly-discrepant candidates, for which very small spectrophotometric distances were found, are plotted as red dots (taken from Kreuzer 2021).

distances, which are marked with red dots and correspond to the gray dots in Figure 5.1. All of them have close-by objects that may affect the distance measurements. The outlier in the lower right corner is most likely affected by the prior used in Bailer-Jones et al. (2018). Since the uncertainties of the spectrophotometric distances are smaller than the ones for the parallax inferred distances, Kreuzer (2021) preferred the measurements from his work.

The kinematic analysis of the WDs in Kreuzer (2021) does not comprise a full classification into thin disk, thick disk and halo objects, but only filters out halo candidates based on the Toomre-diagram (see Figure 5.4). It contains only 373 objects, because there are no *Gaia* DR2 proper motions available for 20 of the WDs and Kreuzer (2021) neglected the eight outliers in Figure 5.3 marked with red dots. However, it can be seen that most of the stars are distributed symmetrically around a  $V$ -velocity of  $V \approx 240 \text{ km s}^{-1} \approx V_{\text{LSR}}$  and lie within the thin disk or thick disk contours. Hence, the MMT WD sample contains mostly Galactic disk members, as expected for white dwarfs. Kreuzer (2021) only found five candidates probably belonging to the halo, whose orbits are shown in Figure 5.5. Three of them (J0026-0807, J1146+2129 and J1659+1421) were not known as white dwarfs before. All of them, except J1146+2129, show an extension above and below the Galactic disk and a high irregularity, which confirms them to be halo objects. Two of them (J0917+0209 and J0026-0807) even seem to be on retrograde orbits, as their  $V$ -velocity is negative. In particular, the nature of J1146+2129 should be checked with more recent data, since its orbit does not even reach 1 kpc in  $Z$ -direction and

is very regular. Thus, a thin or thick disk membership seems to be more likely.

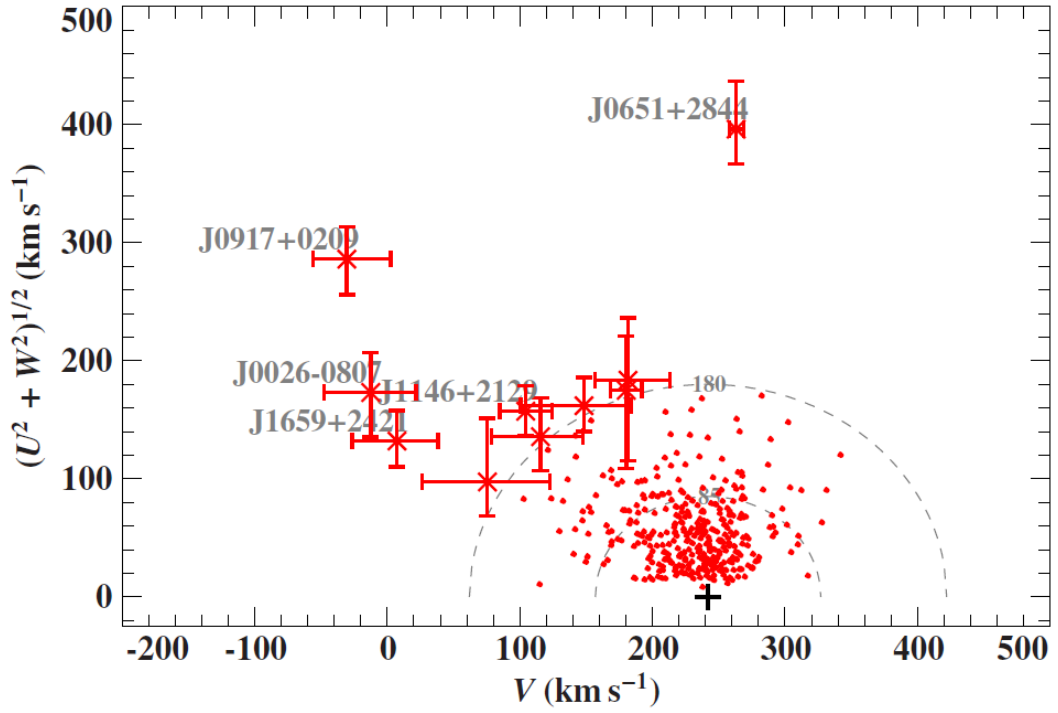


**Figure 5.4:** Toomre-diagram of the MMT WD sample. Probable halo WD candidates are marked with their individual short identifiers. Thin and thick disk contours (dashed gray lines) at  $85 \text{ km s}^{-1}$  and  $180 \text{ km s}^{-1}$ , respectively (taken from Kreuzer 2021).

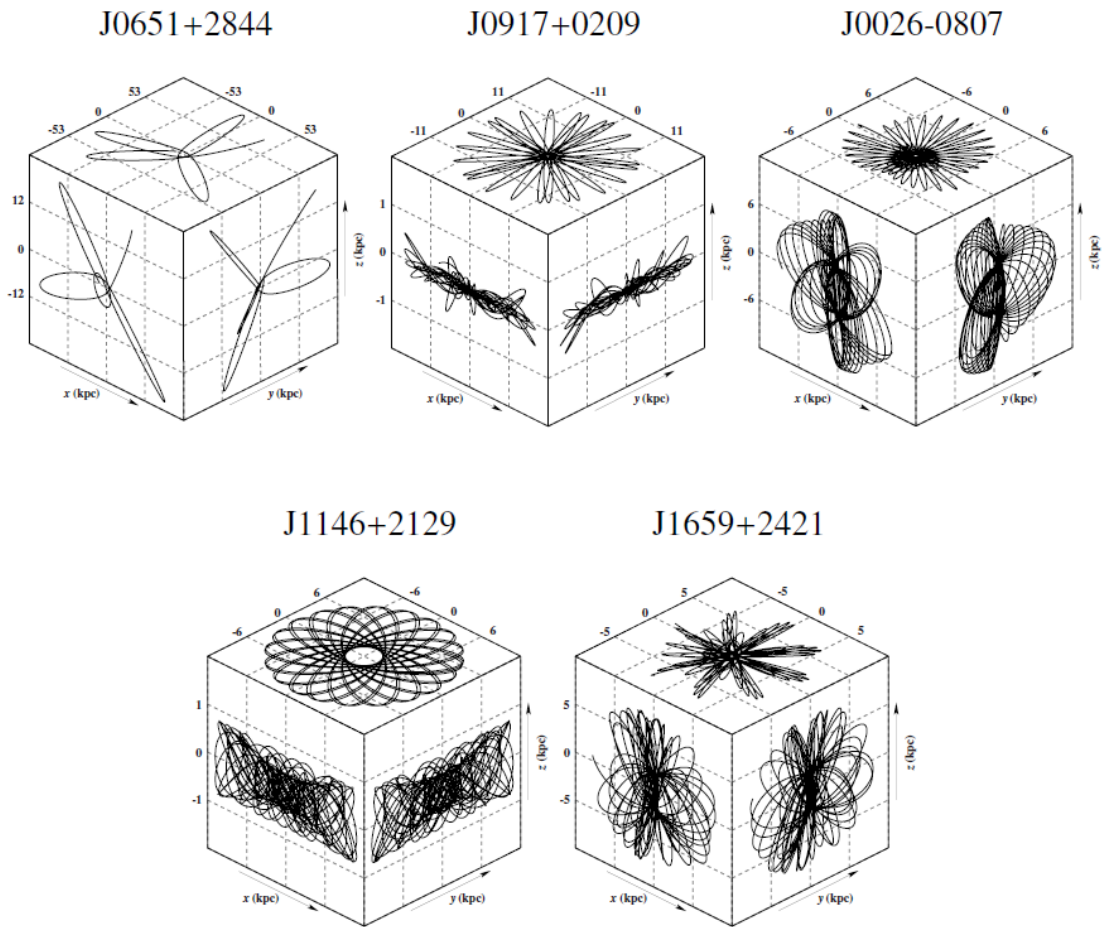


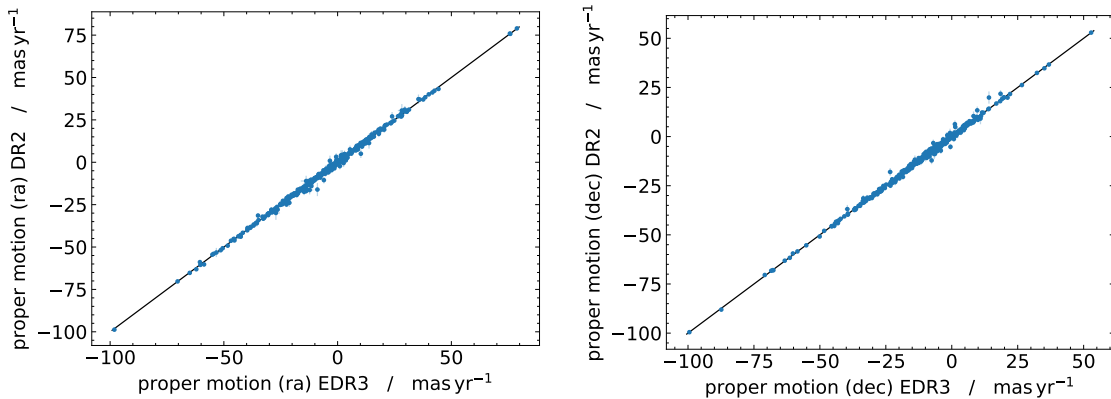
**Figure 5.5:** Orbits of the five halo WD candidates by calculating their trajectories 5 Gyr into the future (taken from Kreuzer 2021).

## 5.2 Comparison of *Gaia* DR2 and EDR3 astrometric data

Before repeating the kinematic analysis for the MMT WD sample with *Gaia* EDR3 proper motions, it might be interesting how the astrometric data changed from DR2 to EDR3. Especially, it appears worthwhile to check if the parallax inferred EDR3 distances now exceed the precision of the spectrophotometric distances and can be preferred to use. Therefore, the new proper motions and distances will be compared to the previous ones used by Kreuzer (2021) in the next two subsections.

### 5.2.1 Proper motions

The comparison of the proper motions from *Gaia* DR2 and EDR3, shown in Figure 5.6, demonstrates that they are in extremely good agreement and have very small uncertainties, except of a few little outliers. Hence, it is to be expected that the kinematics of the WDs will not change significantly due to the new proper motions. However, the number of objects within the MMT WD sample with available *Gaia* proper motions increased from 373 to 392. Hence, only 9 out of 401 WDs still lack proper motion measurements and perhaps halo candidates can be found among the 19 additional objects. In conclusion, *Gaia* EDR3 provides improved proper motions including 19 objects with no data in DR2, which calls for a kinematic reanalysis.



(a) Comparison of the proper motion in direction of right ascension.

(b) Comparison of the proper motion in direction of declination.

**Figure 5.6:** Comparison of *Gaia* DR2 and EDR3 proper motions. The diagonal lines are the identity relations.

### 5.2.2 Distances

Unfortunately, the spectrophotometric distances from Kreuzer (2021) were not available for the WDs, but at least the atmospheric and photometric parameters. Thus, they were determined following the approach described in subsection 2.2.3 and uncertainties were estimated with a Monte Carlo simulation of 20 000 000 samples. As estimator for the resulting distributions the mode and 68.27% ( $1\sigma$ ) highest density

interval (HDI) has been chosen. The resulting distances are shown in comparison to *Gaia* EDR3 parallax inferred (geometric<sup>2</sup>) distances from Bailer-Jones et al. (2021) in Figure 5.7. In general they are in good agreement, especially for close-by objects. However, there are of course the same outliers with extremely small distances as marked with red dots in Figure 5.3. While Kreuzer (2021) neglected them, they are used in this work for the kinematic analysis, since they are not outstanding or suspicious at any further point. Again, as well as in Figure 5.3, the uncertainties on the spectrophotometric distances are smaller than the ones by Bailer-Jones et al. (2021). Therefore, they are also preferred in this work.

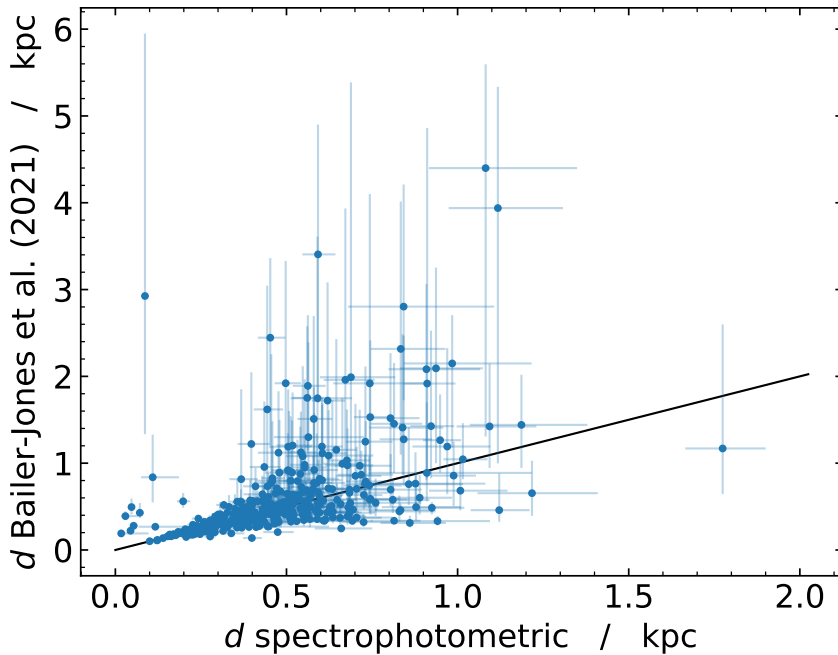


**Figure 5.7:** Comparison of the measured spectrophotometric distances to the (geometric) distances inferred from *Gaia* EDR3 parallaxes by Bailer-Jones et al. (2021). The diagonal line is the identity relation.

### 5.3 Kinematic analysis

The MMT WD sample is expected to be dominated by thin disk stars, with a smaller contribution of thick disk stars and only a few halo stars. Since the distance from the Galactic plane in  $Z$ -direction is a useful indicator for population membership (as described in section 4.2), first of all the distributions of the recorded distances above or below the Galactic plane ( $z_{\text{now}}$ ) and of the maximum distances ( $z_{\text{max}}$ ) derived from the orbits are shown in Figure 5.8. They strongly support the expectations, as almost all WDs are located below  $z_{\text{now}} < 1$  kpc. Even  $z_{\text{max}}$  exceeds 1 kpc only for a

<sup>2</sup> Bailer-Jones et al. (2021) calculated distances with two different approaches. The first, geometric, uses the parallax together with a direction-dependent prior on distance. The second, photogeometric, additionally uses the colour and apparent magnitude of a star, by exploiting the fact that stars of a given colour have a restricted range of probable absolute magnitudes (plus extinction). In the comparison of Figure 5.7 the pure geometric ones are shown.

small number of objects and hence, halo WDs are rarely expected as result for the classification.

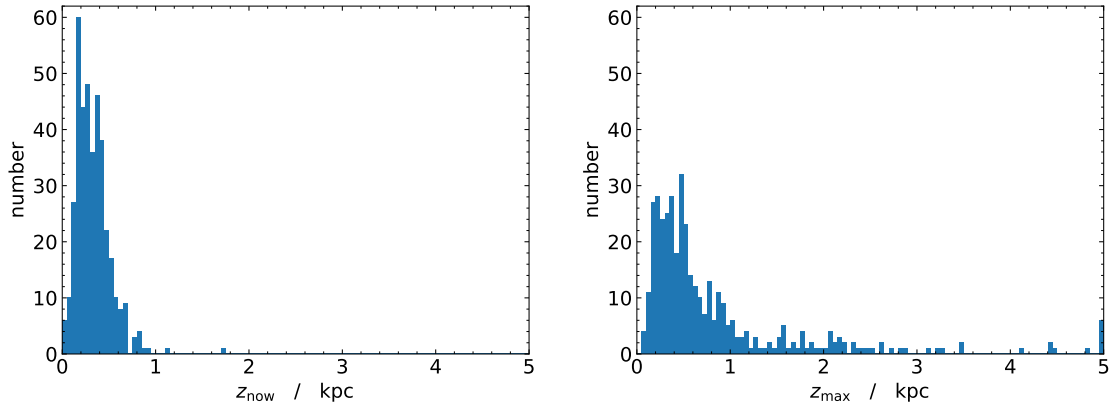


**Figure 5.8:** Histograms for the distributions of recorded  $z_{\text{now}}$ -values and maximum  $z_{\text{max}}$ -values derived from the orbits for the MMT WD sample.

Following the procedure outlined in section 4.2, the classification of the WDs was carried out by plotting the six kinematic diagrams shown in Figure 5.9 and evaluating the orbits. Obviously, almost all of the WDs lie within the thin and thick disk contours and just a few are located outside in each diagram. The resulting percentages and total numbers (given in brackets) of the classification for each population are the following:

<b>Thin disk</b>	→	79%	(310)
<b>Thick disk</b>	→	19%	(76)
<b>Halo</b>	→	2%	(6)

This fulfills the expectations. Pauli et al. (2006) investigated a comparable number of white dwarfs (398) from the SPY survey and found percentages of 91% thin disk stars, 7% thick disk stars and 2% halo stars (section 4.1). Whereas the amount of halo objects is identical, their thick disk contribution is smaller. Dimpel (2018) revisited the extended SPY survey with a total number of 609 white dwarfs and carried out the same classification as Pauli et al. (2006). He found 92% thin disk stars, 7% thick disk stars and 1% halo stars. Thus, his thick disk contribution is also smaller than in this work. The reason for that might be, that the SPY white dwarfs are significantly brighter than the MMT ones and hence, on average less distant. Therefore, a larger number of thick disk stars can be expected in the MMT WD sample. Furthermore, six halo candidates are found within the MMT WD sample. That is one more than in the previous analysis of Kreuzer (2021). They will be discussed in section 5.4.

In Figure 5.10 an additional interesting kinematic diagram is shown, which is not part of the classification. There the total energy  $E_{\text{tot}}$  (sum of orbital kinetic energy and gravitational potential energy) is plotted over  $L_Z$ . The color-code is that of the final classification. It clearly shows a clustering of all disk members in the same region and only halo stars are outliers, confirming their classification. All stars have a negative  $E_{\text{tot}}$ , which means they are all bound to the Galaxy.

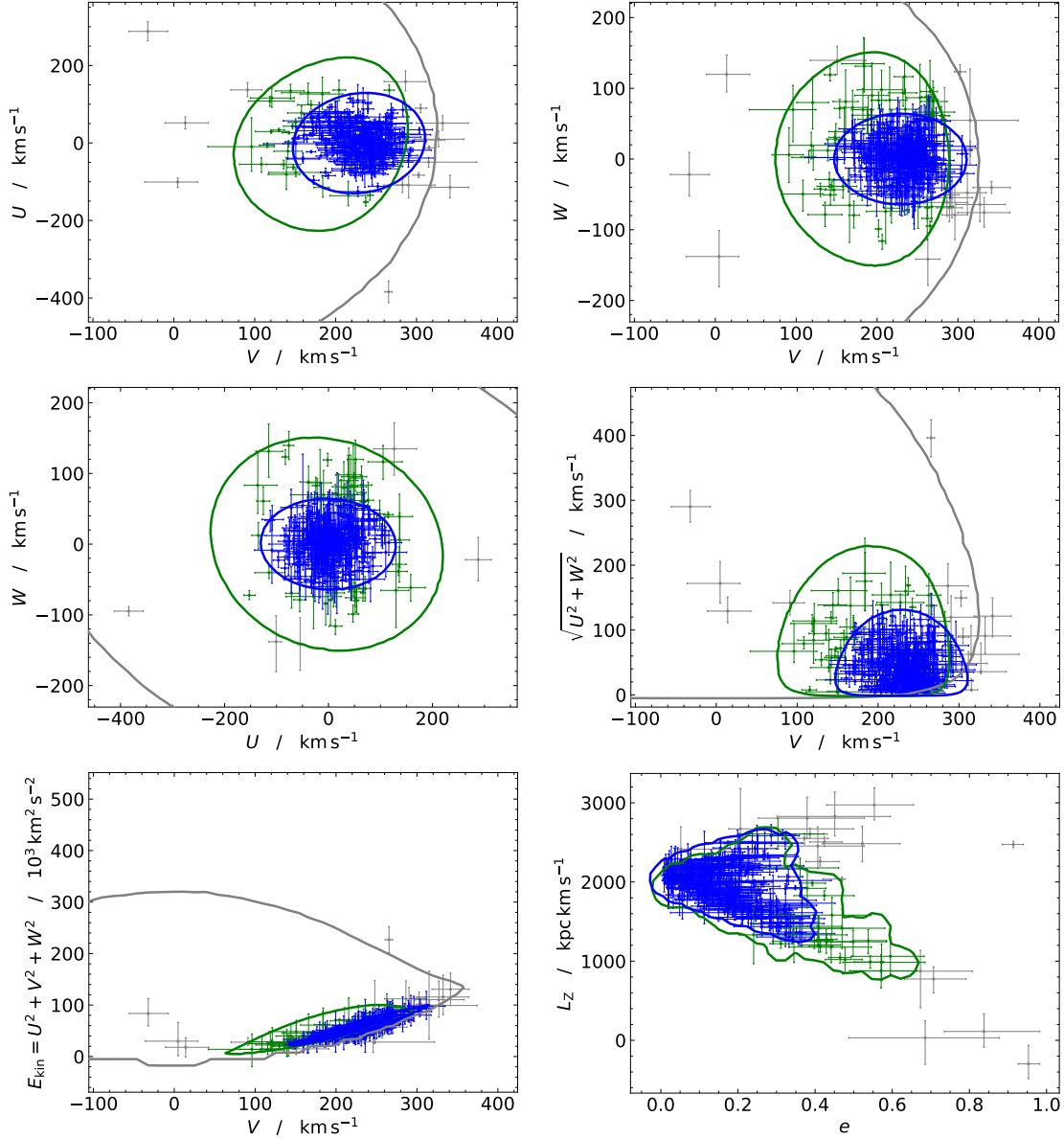


**Figure 5.9:** The six kinematic diagrams,  $U - V$ ,  $W - V$ ,  $W - U$ , Toomre,  $E_{\text{kin}} - V$  and  $L_Z - e$  used for the classification of the WDs together with the respective  $3\sigma$  population contours for thin disk, thick disk and halo. Blue: thin disk. Green: thick disk. Gray: halo. Assignments of individual stars to the stellar populations due to the contours can be different in different diagrams. Therefore, the color-code is individual for each diagram.

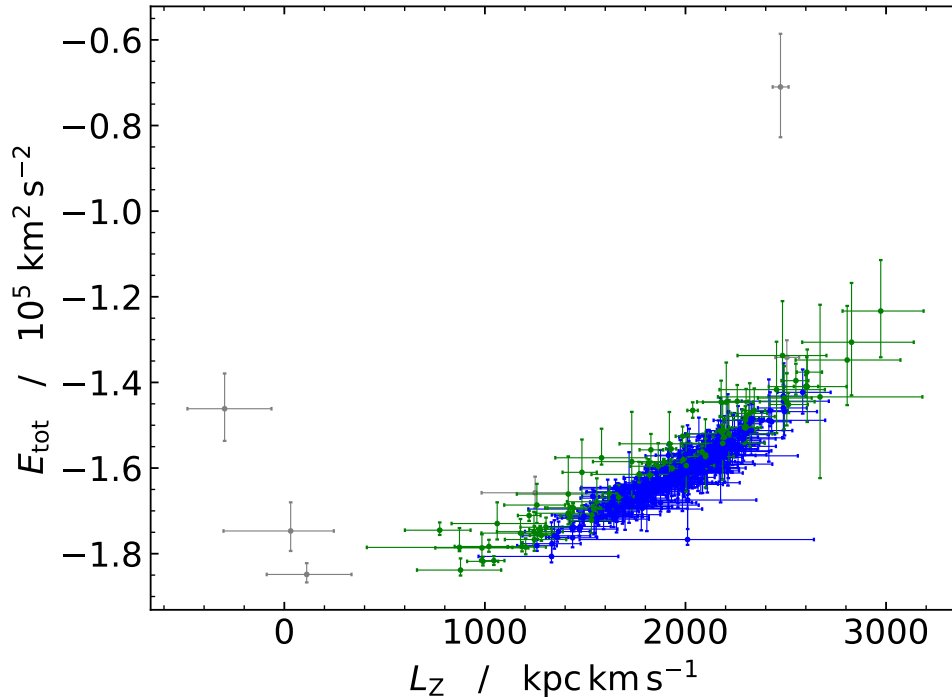


**Figure 5.10:**  $E_{\text{tot}} - L_Z$ -diagram for the MMT WD sample with the color-code according to the final classification. Blue: thin disk. Green: thick disk. Gray: halo.

## 5.4 Discussion of the halo candidates

Six halo candidates were found within the MMT WD sample, according to the classification scheme described in section 4.2. Their orbits are shown in Figure 5.11. Obviously, all of them extend far above and below the Galactic disk and show a high irregularity, which confirms them to be halo objects. One of them (J0917+0209) is on a retrograde orbit, as its  $V \approx -32 \text{ km s}^{-1}$  is negative. The  $V$ -velocity of J0026-0807 is still positive ( $\sim 4 \text{ km s}^{-1}$ ), but very close to zero. This behaviour is also reflected in its orbit, as it almost has no motion in  $Y$ -direction. The most extreme candidate is J0651+2844, because its distance from the Galactic centre within the Galactic plane ranges up to several tens of kpc and it has the highest  $z_{\text{max}} \approx 18 \text{ kpc}$  of all halo candidates.

In comparison to the five halo candidates from Kreuzer (2021), two new ones (J1557+2823 and J2227+2355) are found and one (J1146+2129) got rejected, as already predicted in section 5.2. It is classified as thick disk star now. So in conclusion it can be said, that most of the WD halo candidates in Kreuzer (2021) were confirmed due to the reanalysis with *Gaia* EDR3 proper motions, but also new ones have been discovered.

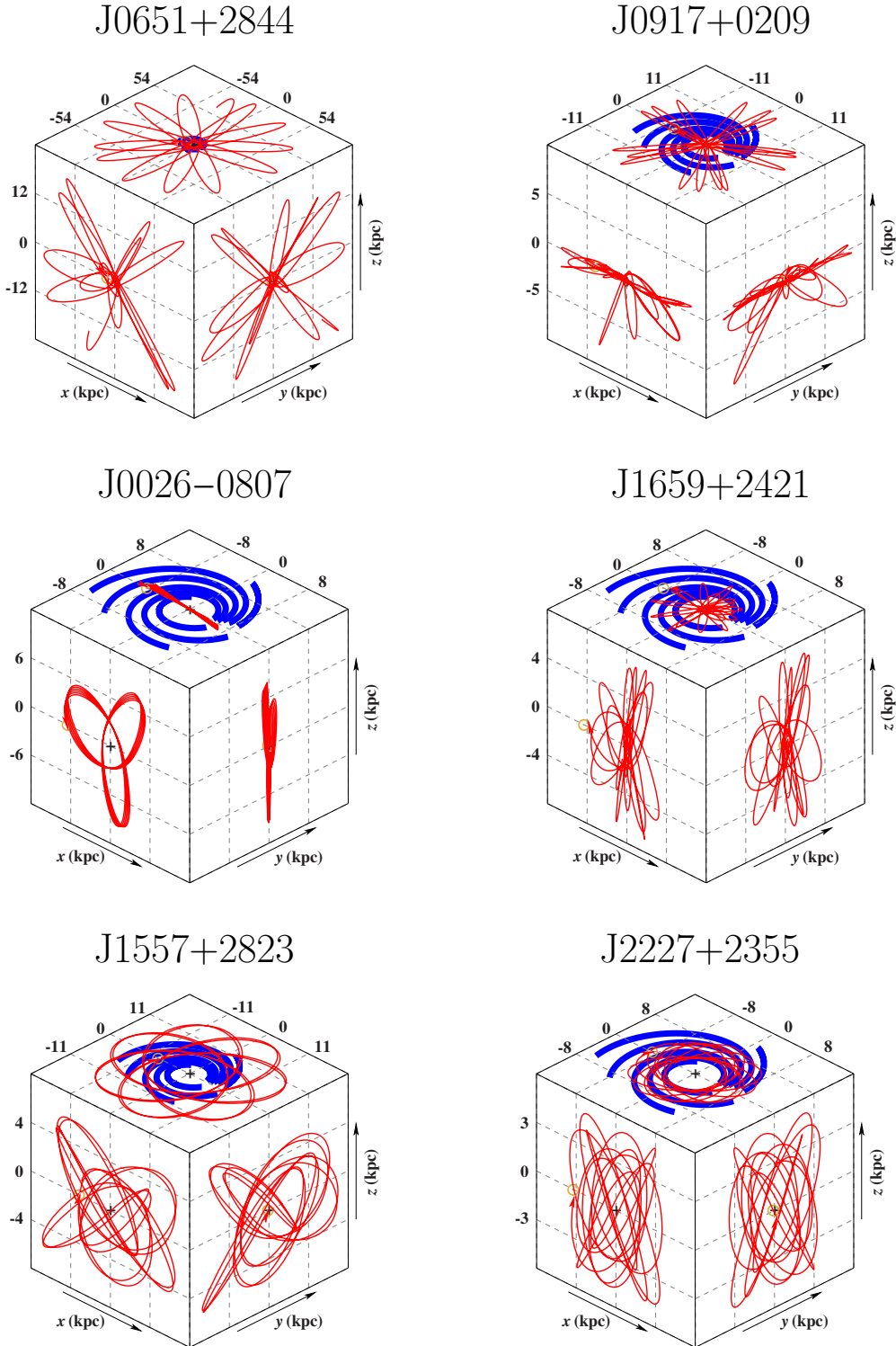


**Figure 5.11:** Three-dimensional orbits of the six WD halo candidates in a Galactic Cartesian coordinate system. The  $z$ -axis points towards the Galactic north pole. The red trajectories with arrows, indicating the star's current position, are calculated in the gravitational potential from Allen & Santillan (1991), updated with recent observations by Irrgang et al. (2013), for either ten revolutions or 15 Gyrs backwards in time. The blue spirals represent the shape of the Galaxy as reference and the current positions of the Sun and the Galactic center are marked with a yellow circle and a plus sign, respectively.

# 6 Blue Horizontal Branch stars in the MMT sample

The objects in the MMT HVS survey have been originally selected in order to find faint blue B-type halo stars excluding the Galactic plane. Therefore, beside the contamination of WDs and a small contribution of other populations shown in Figure 2.2, it contains a large number of about 1300 BHB stars and BSs, which are typical for an old halo population. A major problem is to distinguish blue horizontal branch stars from blue stragglers. But because the BHB stars are core helium burning stars, their surface gravities are somewhat lower than that of the hydrogen burning BS stars. Hence, Kreuzer (2021) found the empirical relation

$$\log(g) < 0.000112 \cdot T_{\text{eff}} + 2.75 \quad (6.1)$$

for the BHB stars to directly distinguish them from the BSs for the first time in the MMT sample. In previous analyses only percentages could be derived, but no classification of individual objects has been carried out. This allowed him to separately discuss both stellar classes.

The analysis of the MMT BHB sample has the aim to find kinematic outliers, such as runaway or hyper-velocity-stars. Hence, the focus is set on looking for objects that are possibly unbound to the Galaxy. In contrary to the WDs of chapter 5, which are strongly dominated by Galactic disk members, almost all BHB stars are expected to be old halo objects. Thus, it might also be interesting to filter out stars belonging to the Galactic disk instead of the halo by applying the classification scheme described in section 4.2.

Again first of all the findings of Kreuzer (2021) will be summarized in section 6.1 and the *Gaia* EDR3 proper motions will be compared to the previous ones from DR2 in section 6.2, before addressing the kinematic analysis of the BHB stars in section 6.3.

## 6.1 Previous findings

By applying the empirical relation of Equation 6.1 on the sample of faint blue stars, Kreuzer (2021) separated a total number of 838 BHB stars from the BSs (~45% of the whole MMT sample). Then he carried out a comprehensive spectroscopic analysis with the help of model atmospheres and a sophisticated analysis strategy. The atmospheric parameters  $T_{\text{eff}}$  and  $\log(g)$  are discussed with respect to the metallicity and the helium abundance, as well as the so-called Grundahl jump, which can be seen as jump towards higher surface gravities for the cooler end of the BHB in Figure 6.1 (for details see Kreuzer 2021).



somewhere in the Galactic disk, the high-velocity BHB stars have moderate radial velocities and are dominated by their tangential velocities. Also a pre-ELM-WD nature cannot be excluded for all of these candidates (for details see Kreuzer 2021), but even in that case  $v_{\text{Grf}}$  would still be extreme (Table 6.1). Therefore, it will be exciting if redoing the analysis with *Gaia* EDR3 data confirms or falsifies these proper motion dominated high-velocity stars.

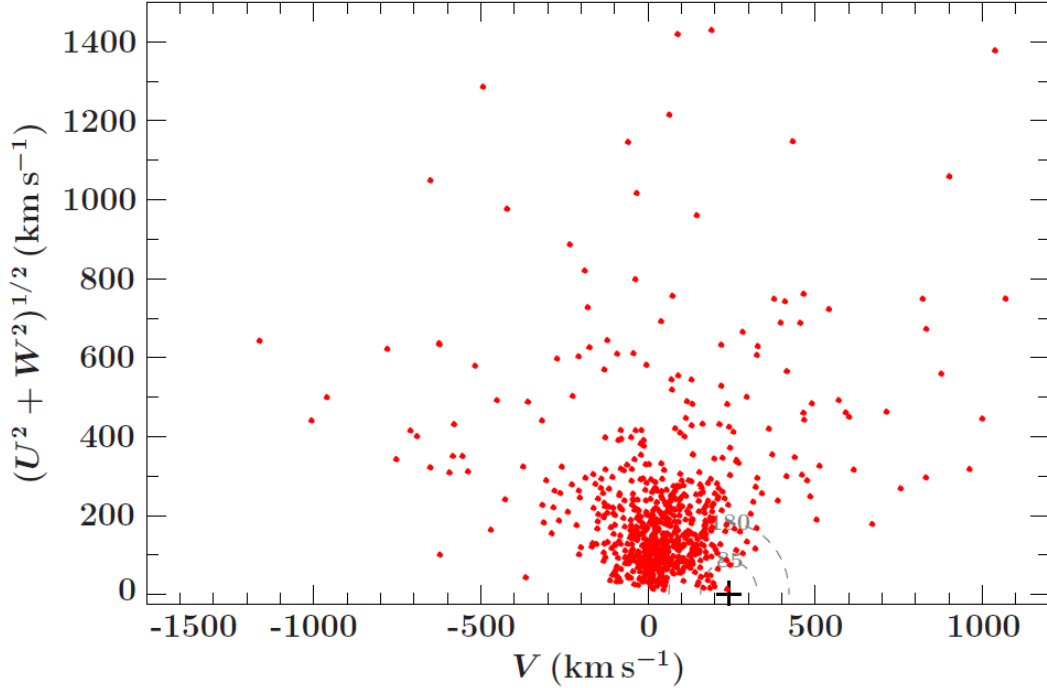


**Figure 6.2:** Toomre-diagram of the BHB candidates. The plot shows the parameter space of all non-extreme objects. Gray dashed thin and thick disk contours at  $85 \text{ km s}^{-1}$  and  $180 \text{ km s}^{-1}$  are the same as in Figure 5.4 (taken from Kreuzer 2021).

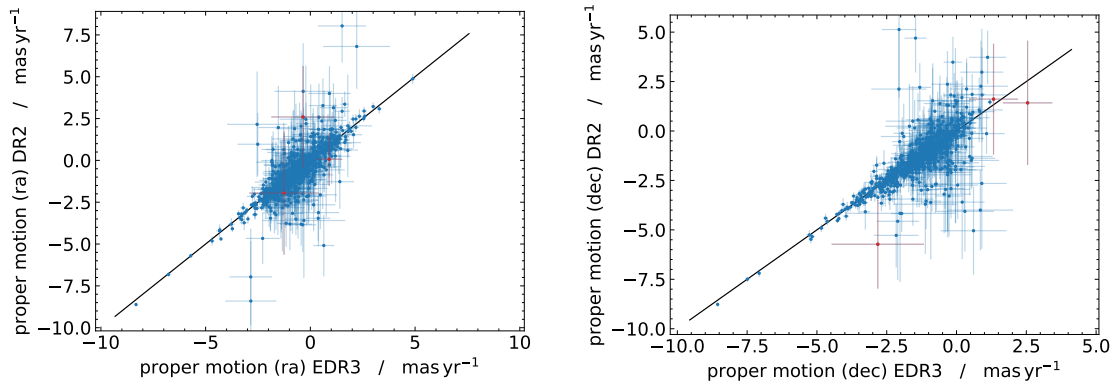
**Table 6.1:** The kinematically most extreme BHB candidates. Given are the effective temperature  $T_{\text{eff}}$ , the surface gravity  $\log(g)$ , the radial velocity  $v_{\text{rad}}$ , the distance  $d$ , both proper motions  $\mu$  and the Galactic rest frame velocity  $v_{\text{Grf}}$ . In addition to the BHB parameters a distance  $d_{\text{ELM}}$  and Galactic rest frame velocity  $v_{\text{Grf,ELM}}$  estimate for the pre-ELM WD case is provided (taken from Kreuzer 2021).

Object	$T_{\text{eff}}$ (K)	$\log(g)$ (cgs)	$v_{\text{rad}}$ ( $\text{km s}^{-1}$ )	$d$ (kpc)	$\mu$		$v_{\text{grf}}$ ( $\text{km s}^{-1}$ )	$d_{\text{ELM}}$ (kpc)	$v_{\text{grf,ELM}}$ ( $\text{km s}^{-1}$ )
					$\mu_{\alpha} \cos \delta$	$\mu_{\delta}$			
SDSS J070010.88+293737.8	$8360^{+220}_{-190}$	$3.30^{+0.10}_{-0.12}$	$-44.0^{+9.7}_{-9.1}$	$71.5^{+11.2}_{-9.3}$	$8.04 \pm 2.19$	$-5.04 \pm 2.23$	$3043.6^{+1085.3}_{-953.8}$	45.2	1846
SDSS J083005.76+185105.1	$9590^{+140}_{-240}$	$3.38^{+0.08}_{-0.11}$	$135.8^{+13.7}_{-12.8}$	$81.7^{+11.2}_{-8.6}$	$6.81 \pm 2.53$	$-4.07 \pm 2.04$	$2996.2^{+1217.2}_{-1113.7}$	51.7	1818
SDSS J085954.99+350306.1	$10230^{+160}_{-190}$	$3.69^{+0.08}_{-0.09}$	$30.2^{+10.3}_{-10.2}$	$43.6^{+5.3}_{-4.5}$	$-5.09 \pm 1.84$	$4.70 \pm 1.74$	$1618.4^{+524.1}_{-487.5}$	27.6	1089
SDSS J131614.96+001932.2	$8200^{+180}_{-120}$	$2.94^{+0.20}_{-0.12}$	$139.2^{+20.3}_{-19.5}$	$109.5^{+18.9}_{-22.0}$	$2.59 \pm 3.04$	$-5.73 \pm 2.25$	$3252.5^{+1690.8}_{-1350.0}$	69.2	1970
SDSS J132831.75+075712.7	$10300^{+160}_{-160}$	$3.79^{+0.07}_{-0.07}$	$-28.7^{+8.3}_{-8.3}$	$55.4^{+5.9}_{-5.2}$	$-8.41 \pm 3.59$	$5.13 \pm 3.45$	$2656.4^{+1130.2}_{-1053.0}$	35.0	1622
SDSS J212620.18-034148.8	$11100^{+140}_{-150}$	$3.78^{+0.06}_{-0.06}$	$-104.0^{+6.6}_{-6.6}$	$53.1^{+4.9}_{-4.6}$	$-6.96 \pm 2.88$	$-3.60 \pm 2.89$	$2025.6^{+771.5}_{-722.3}$	33.6	1194
SDSS J220914.80-093323.7	$7900^{+280}_{-130}$	$2.75^{+0.13}_{-0.09}$	$-228.1^{+10.8}_{-11.9}$	$128.3^{+18.2}_{-18.1}$	$-1.73 \pm 2.95$	$-4.00 \pm 2.04$	$3004.1^{+1334.4}_{-1159.9}$	81.1	1512
SDSS J225059.68+292932.7	$8400^{+190}_{-210}$	$2.77^{+0.11}_{-0.10}$	$-126.9^{+13.0}_{-13.8}$	$127.7^{+17.4}_{-16.2}$	$-2.47 \pm 1.43$	$1.07 \pm 1.64$	$2013.7^{+841.4}_{-755.7}$	80.8	1146

## 6.2 Comparison of *Gaia* DR2 and EDR3 proper motions

Since parallax inferred distances are not reliable for very distant objects, only the change of the proper motions from *Gaia* DR2 to EDR3 needs to be checked. The kinematic analysis of the BHB stars will be carried out with the spectrophotometric distances from Kreuzer (2021).

The comparison of both *Gaia* DR2 proper motions to the EDR3 ones is shown in Figure 6.3. First of all it can be seen that the proper motions components are much smaller than, for example, for the WDs in Figure 5.6. This is typical for very distant stars, because their apparent motion on the night sky is less obvious, even if they move with the same velocity as closer stars. Furthermore, they deviate more strongly and have higher uncertainties, especially in the region close to zero, which might affect the results of the kinematic analysis. Since *Gaia* EDR3 measurements are of superior quality, a kinematic reanalysis is very promising. The stars marked with red dots are three out of six BHB candidates being unbound to the Galaxy, which will be discussed in chapter 8. In total *Gaia* EDR3 provides proper motions for 814 objects within the MMT BHB sample, which are 66 more than in DR2. So perhaps some kinematically extreme stars can be found among the additional ones.



(a) Comparison of the proper motion in direction of right ascension.

(b) Comparison of the proper motion in direction of declination.

**Figure 6.3:** Comparison of *Gaia* DR2 and EDR3 proper motions. The diagonal lines are the identity relations. The stars marked with red dots are three out of six BHB candidates being unbound to the Galaxy and will be discussed in chapter 8. For the other three no *Gaia* DR2 proper motions are available.

## 6.3 Kinematic analysis

Histograms for the  $z_{\text{now}}$ - and  $z_{\text{max}}$ -distributions are shown in Figure 6.4 for the MMT BHB sample. They clearly differ from that of the WDs in Figure 5.8, as they range up to several tens of kpc, even above 100 kpc, and almost no stars lie below 5 kpc. Therefore, the sample must be thoroughly halo dominated and non-halo objects should be rarely found. This completely supports the expectations.

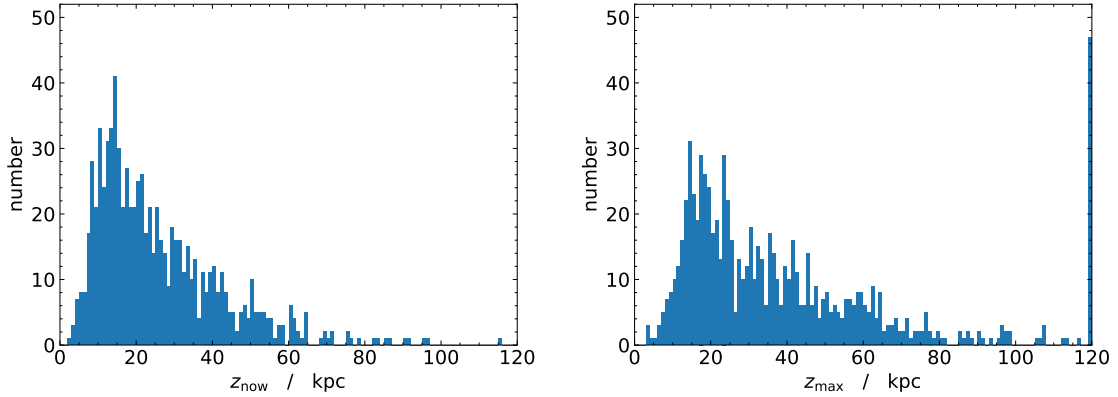


**Figure 6.4:** Histograms for the distributions of recorded  $z_{\text{now}}$ -values and maximum  $z_{\text{max}}$ -values derived from the orbits for the MMT BHB sample.

The classification was again carried out by applying the procedure described in section 4.2. All six kinematic diagrams are shown in Figure 6.5 together with the respective  $3\sigma$  population contours for thin disk, thick disk and halo. The most extreme objects are omitted in the plots, because either their positions exceed the axis limits or their uncertainties would dominate the whole diagram, but are still part of the classification. While in the diagrams for the WDs (Figure 5.9) only a small number of stars is located outside the thick disk contours, here the sample is distributed almost homogeneously over the whole area. Especially for the diagrams including the single-velocities  $U$ ,  $V$  and  $W$ , the stars are spread symmetrically around zero. In particular, for the  $V$ -velocity (not following the Galactic rotation) this behaviour is a strong hint towards the halo nature of the objects, but also illustrates the problem of the overlapping population regions. For example in the  $W - U$ -diagram the thin disk contour is completely filled with lots of stars, because it is centered at  $W = 0$  and  $U = 0$ , while it is almost empty in the  $L_Z - e$ -diagram. In the latter one it is also shown that the majority of the stars cluster around  $L_Z = 0$  and have high eccentricities between  $e = 0.5$  and  $e = 1$ . This can not be the case for disk members. The percentages (absolute numbers) of the populations are the following:

<b>Thin disk</b>	→	0.4%	(3)
<b>Thick disk</b>	→	0.1%	(1)
<b>Halo</b>	→	99.5%	(810)

This result is unambiguous, as almost 100% of the MMT BHB sample are classified as halo objects. It is also underlined by the  $E_{\text{tot}} - L_Z$ -diagram in Figure 6.6. The thin and thick disk region, located around  $L_Z = 2000 \text{ kpc km s}^{-1}$  and  $E_{\text{tot}} = -1.6 \cdot 10^5 \text{ km}^2 \text{ s}^{-2}$  and, for example, seen in Figure 5.10 for the WDs, is nonexistent. Only the three blue thin disk candidates and a few halo stars are settled in a region moderately above it. In general the distribution is almost axis-symmetric around  $L_Z = 0$  and ranges closer to  $E_{\text{tot}} = 0$  than Figure 5.10, suggesting that some of the extreme outliers not shown in Figure 6.6 might have a positive total energy and are, hence, unbound to the Galaxy.

For verifying the population membership of the four non-halo candidates, their orbits are shown in Figure 6.7. The first two (J0723+3519 and J0731+2416) truly

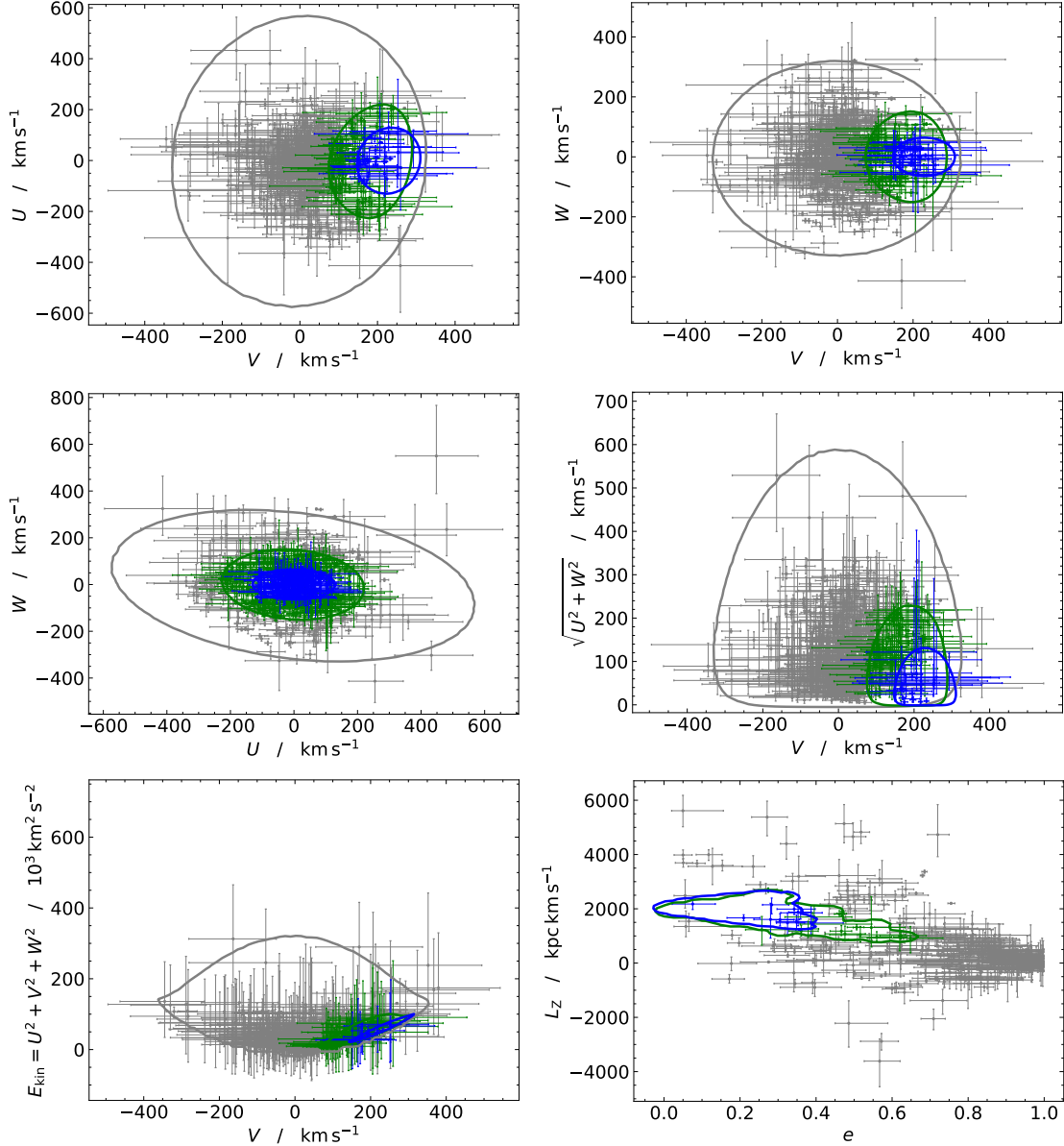


**Figure 6.5:** The six kinematic diagrams,  $U - V$ ,  $W - V$ ,  $W - U$ , Toomre,  $E_{\text{kin}} - V$  and  $L_z - e$  used for the classification of the BHB stars together with the respective  $3\sigma$  population contours for thin disk, thick disk and halo. Blue: thin disk. Green: thick disk. Gray: halo. The color-code is individual for each diagram. The most extreme objects (either lying outside the axis limits or having extremely large errorbars) are omitted in the diagrams, but are still part of the classification.

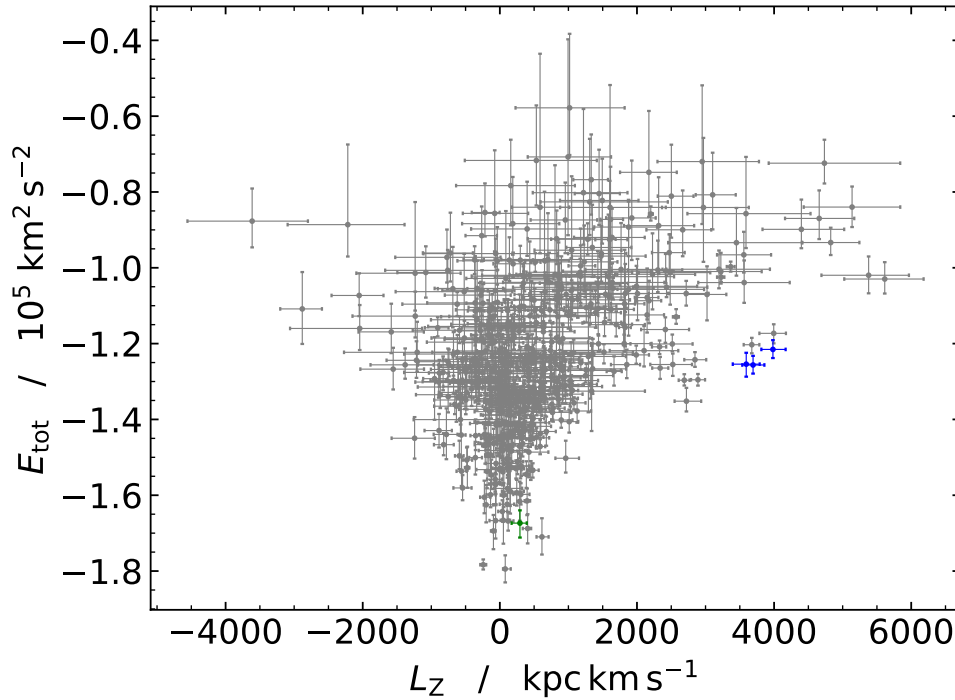


**Figure 6.6:**  $E_{\text{tot}} - L_Z$ -diagram for the MMT BHB sample with the color-code of the classification. Blue: thin disk. Green: thick disk. Gray: halo. The most extreme objects are omitted.

show disk characteristics, as they have only a moderate extension in  $Z$ -direction and are very regular on almost circular orbits in the outer regions of the Galactic plane. The third one (J0751+1018) shows a similar behaviour, but is a bit more eccentric. Anyway, a disk membership is also very likely for it. The last one (J1757+4708), however, has an oddly shaped and chaotic orbit, suggesting that it nevertheless belongs to the halo population. Although all, except J1757+4708, are classified as thin disk stars, a thick disk membership seems to be more likely according to the orbits. J1757+4708, which is classified as thick disk star, belongs to the halo instead. So in conclusion it can be said, that the classification scheme described in section 4.2 overall works fine for filtering out non-halo candidates from such an extremely halo dominated sample.

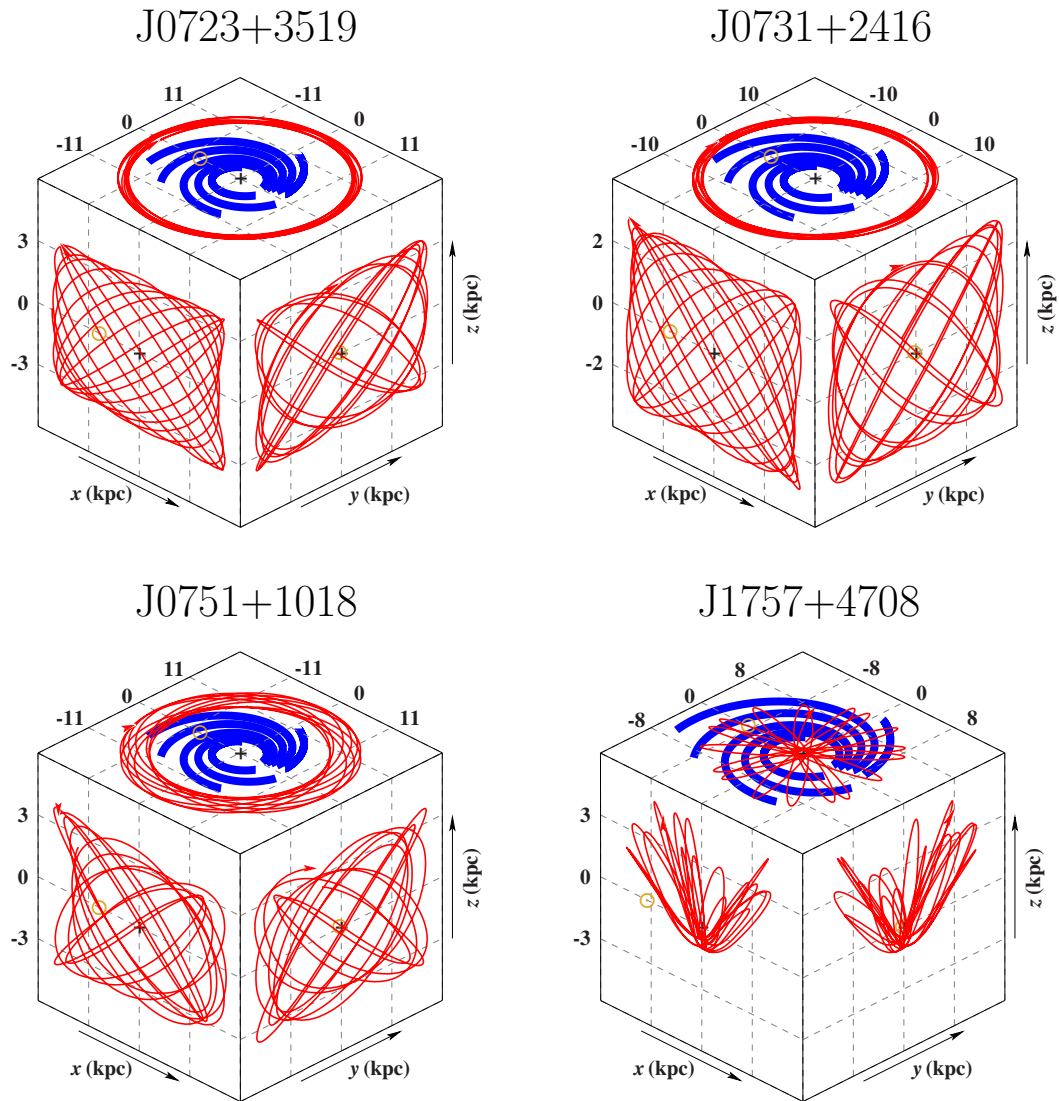
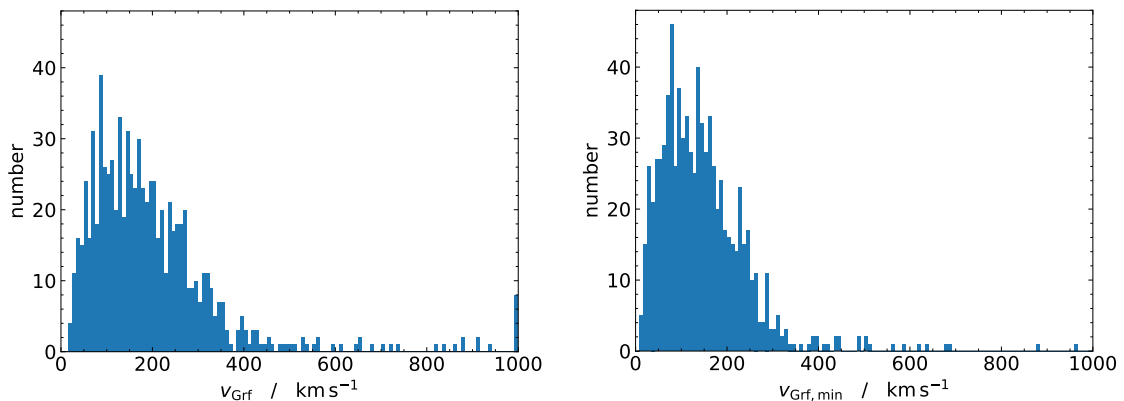


Figure 6.7: Same as Figure 5.11, but for the four BHB non-halo candidates.

Kreuzer (2021) found in his analysis of the BHB stars eight candidates with extreme kinematics in terms of a high  $1\sigma$  minimum Galactic rest frame velocity of  $v_{\text{Grf},\text{min}} > 1000 \text{ km s}^{-1}$ . Therefore, in Figure 6.8 the distributions of  $v_{\text{Grf}}$  and its  $1\sigma$  minimum value  $v_{\text{Grf},\text{min}}$  for the reanalysis with *Gaia* EDR3 proper motions are shown. Whereas there are still a few stars with  $v_{\text{Grf}} \gtrsim 1000 \text{ km s}^{-1}$ , all stars of the sample have a  $1\sigma$  minimum Galactic rest frame velocity of  $v_{\text{Grf},\text{min}} < 1000 \text{ km s}^{-1}$ . Since, based on DR2 proper motions, some stars in Kreuzer (2021) even exceed  $v_{\text{Grf}} > 3000 \text{ km s}^{-1}$  with uncertainties larger than  $\pm 1000 \text{ km s}^{-1}$  (see Table 6.1), it can be said that *Gaia* EDR3 provides unprecedented quality for astrometric data. In this case the constraints on kinematic parameters could be drastically reduced, so that all of the eight candidates in Kreuzer (2021) turn out to be far less extreme in terms of Galactic rest frame velocities.



**Figure 6.8:** Histograms for the distributions of Galactic rest frame velocity  $v_{\text{Grf}}$  and its  $1\sigma$  minimum value  $v_{\text{Grf},\text{min}}$  for the BHB stars.

Nevertheless six candidates were found within the MMT BHB sample in this analysis, which have probabilities of being bound to the Galaxy  $P_b < 5\%$ . They are all part of the kinematically most extreme objects omitted in Figure 6.5 and Figure 6.6. These candidates and the way of calculating boundness probabilities will be discussed separately in chapter 8.

# 7 Blue Stragglers in the MMT sample

By applying the relation of Equation 6.1, Kreuzer (2021) separated a total number of 438 BSs from the BHB stars ( $\sim 23\%$  of the MMT sample). The aims for the analysis of the MMT BS sample are the same as for the BHB stars: Find kinematic outliers, such as runaway or even hyper-velocity-stars (i.e. stars possibly unbound to the Galaxy) and filtering out disk members from this halo dominated sample with the help of the classification scheme described in chapter 4.

Hence, first of all again all findings of Kreuzer (2021) for the BSs will be summarized in section 7.1 and the *Gaia* EDR3 proper motions will be compared to the previous ones from DR2 in section 7.2, before addressing the kinematic analysis in section 7.3.

## 7.1 Previous findings

Kreuzer (2021) used a similar analysis strategy for the BSs as for the BHB stars. The Kiel diagram is shown in Figure 7.1 together with theoretical evolutionary tracks. According to the positions of the BSs there, they must be more massive than the typical halo turnoff mass of around  $0.8 M_{\odot}$ , but the maximum mass should be  $\lesssim 1.6 M_{\odot}$ . The comparison to the evolutionary tracks is consistent with the rejuvenation picture by a merger of two main sequence stars.

For the kinematic analysis again spectrophotometric distances had to be calculated. So Kreuzer (2021) assumed a generic BS mass of  $1.5 \pm 0.15 M_{\odot}$ , which is consistent with the evolutionary tracks and the rejuvenation picture. Although the uncertainty was propagated to the distance uncertainty, the impact of the uncertainty in  $\log(g)$  was still more severe and thus, the mass uncertainty is not dominating the distance uncertainty. The Toomre-diagram for all objects with available *Gaia* DR2 proper motions and decent data quality (386 candidates) is shown in Figure 7.2. Again an almost symmetric distribution around  $V = 0$  is observable, which underlines the predominant halo membership of the BSs. In contrary to the BHB stars no kinematically extreme outliers were found with a Galactic rest frame velocity of  $v_{\text{Grf},\text{min}} > 1000 \text{ km s}^{-1}$ .

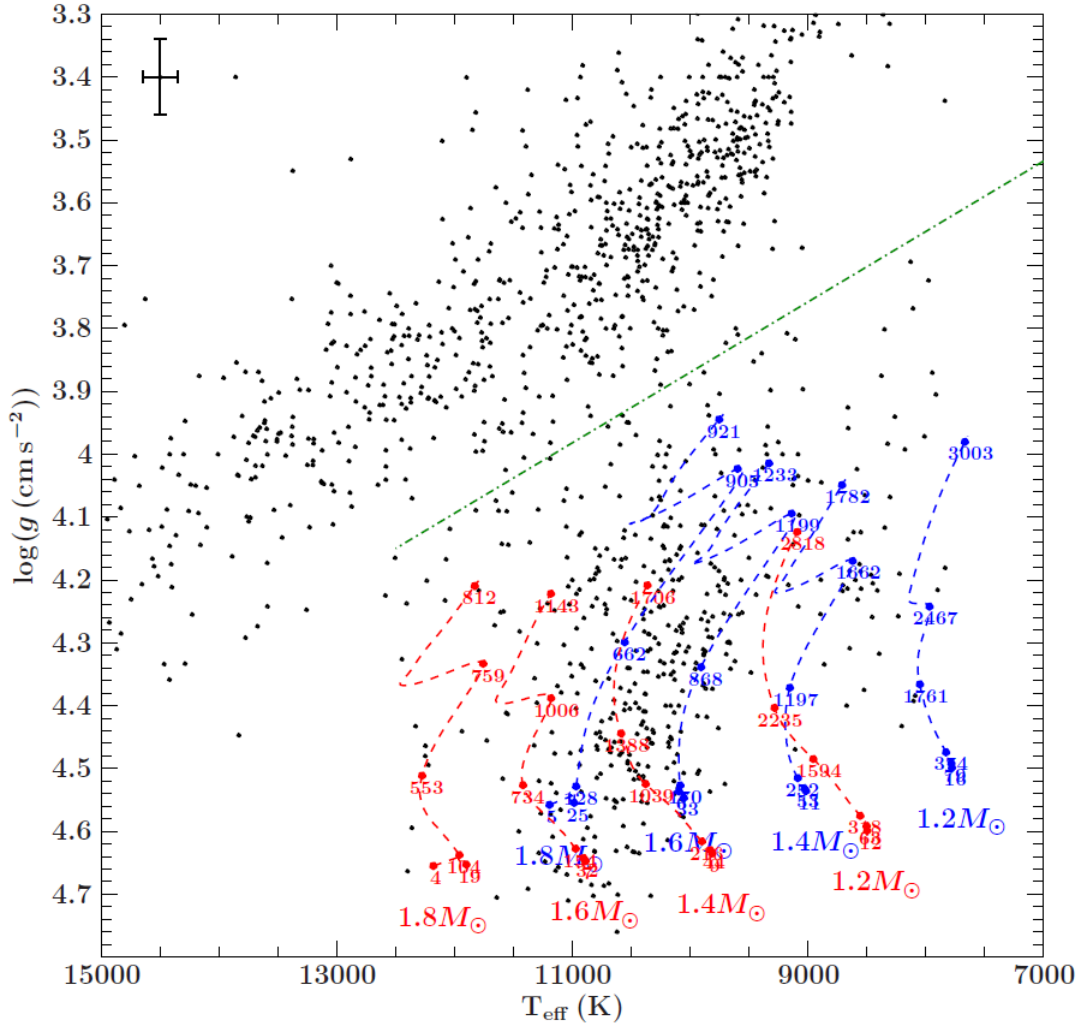


**Figure 7.1:** Positions of all BS (and BHB) candidates in the Kiel diagram. Overplotted are evolutionary tracks from the zero age main sequence (ZAMS) to the terminal age main sequence (TAMS) (for details see Kreuzer 2021). The dashed green line represents the empirical cut (Equation 6.1) between the BHB and BS population. Median uncertainties are plotted in the top left corner (taken from Kreuzer 2021).

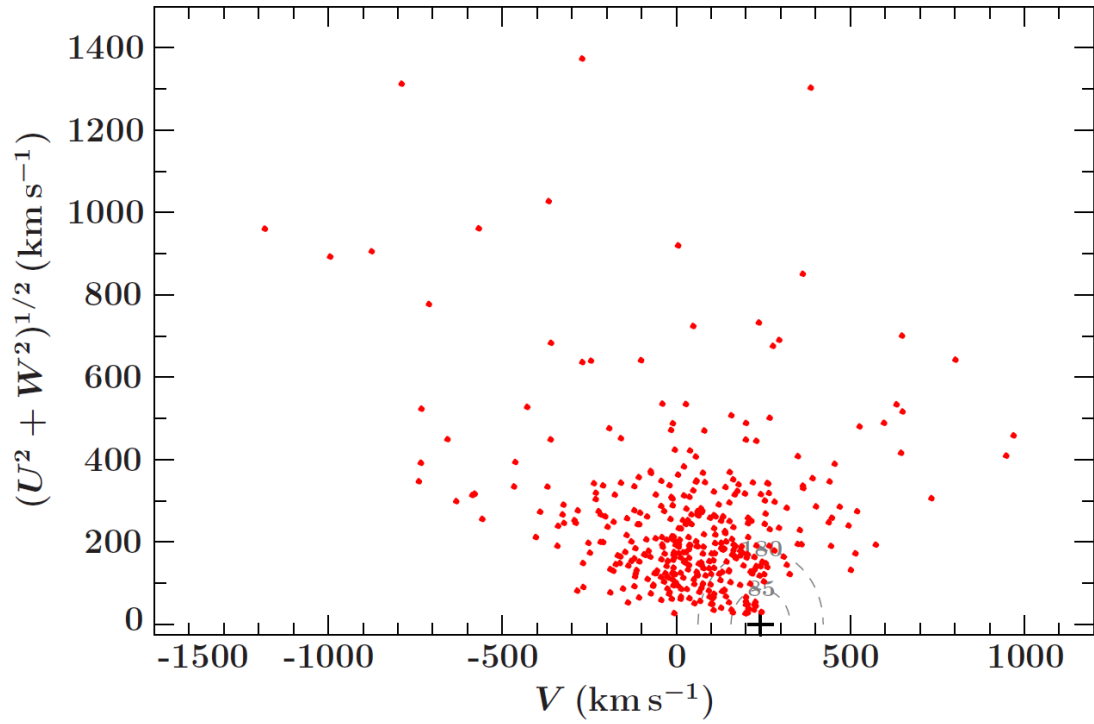
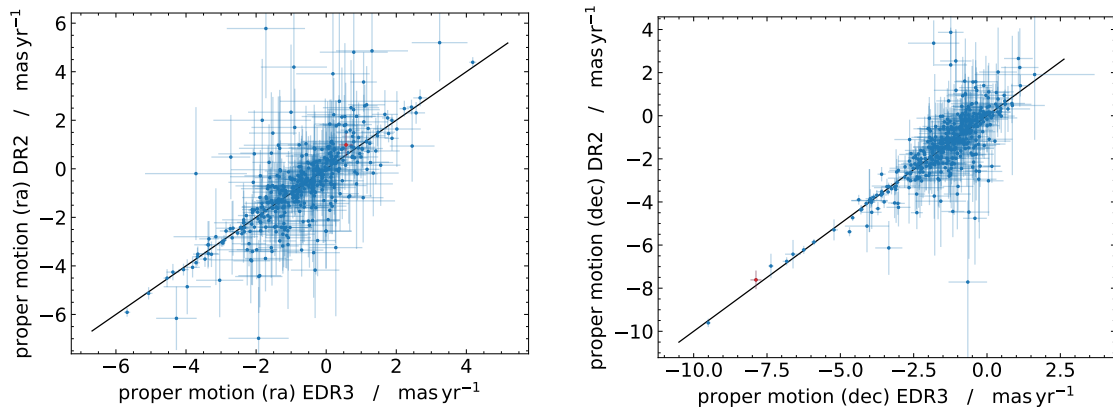


**Figure 7.2:** Toomre-diagram of the BS candidates. Gray dashed thin and thick disk contours at  $85 \text{ km s}^{-1}$  and  $180 \text{ km s}^{-1}$  are the same as in Figure 5.1 and Figure 6.1 (taken from Kreuzer 2021).

## 7.2 Comparison of *Gaia* DR2 and EDR3 proper motions

Again, as for the BHB stars, parallax inferred distances can not be used for the BSs and the spectrophotometric ones from Kreuzer (2021) are taken for the kinematic analysis. Hence, only the *Gaia* DR2 and EDR3 proper motions need to be compared (Figure 7.3). The same pattern as in Figure 6.3 occurs, that is they deviate strongly and have high uncertainties in the region close to zero. Therefore, also for the BSs the results of the kinematic reanalysis are expected to be a significant improvement. The number of stars with available proper motions increased from 386 in *Gaia* DR2 to 450 in EDR3<sup>3</sup>. Hence, 64 additional objects will be part of the analysis.



(a) Comparison of the proper motion in direction of right ascension. (b) Comparison of the proper motion in direction of declination.

**Figure 7.3:** Comparison of *Gaia* DR2 and EDR3 proper motions. The diagonal lines are the identity relations. The star marked with a red dot is one out of two BS candidates being unbound to the Galaxy, which will be discussed chapter 8.

## 7.3 Kinematic analysis

The histograms for the  $z_{\text{now}}$ - and  $z_{\text{max}}$ -distributions for the MMT BS sample (Figure 7.4) show the same pattern as that for the BHB stars (Figure 6.4). They range up to several tens of kpc, even above 100 kpc in the case of  $z_{\text{max}}$ , and almost no stars lie below 5 kpc. This again strongly indicates a thoroughly halo domination of the sample and disk members should be rarely found, as expected.

The classification was once again carried out by applying the procedure described in section 4.2. All six kinematic diagrams are shown in Figure 7.5 together with the respective  $3\sigma$  population contours for thin disk, thick disk and halo. Also the most extreme objects are omitted again in the plots, but are still part of the classification.

<sup>3</sup> This number is even higher than the total number of BSs separated from the BHB stars in Kreuzer (2021). The reason for that might be that Kreuzer (2021) considered the uncertainties on  $T_{\text{eff}}$  and  $\log(g)$  for applying Equation 6.1, whereas in this work only the mean values have been used. Since this issue should not affect the result of the kinematic analysis, it is not further investigated.

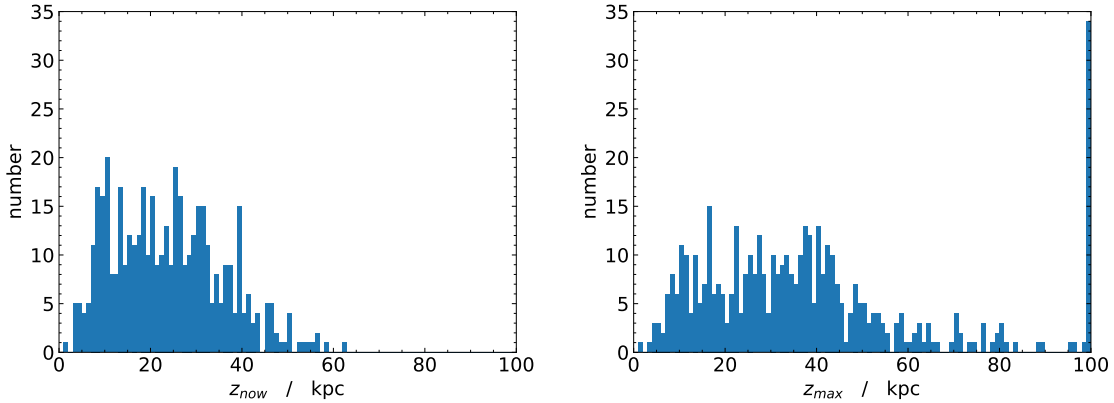


**Figure 7.4:** Histograms for the distributions of recorded  $z_{\text{now}}$ -values and maximum  $z_{\text{max}}$ -values derived from the orbits for the MMT BS sample.

The diagrams show exactly the same behaviour for the BSs as for the BHB stars and therefore, the whole discussion of section 6.3 can be identically adopted. The percentages (total numbers) of the populations according to the classification are the following:

<b>Thin disk</b>	→	0.7%	(3)
<b>Thick disk</b>	→	1.1%	(5)
<b>Halo</b>	→	98.2%	(442)

Although the amount of non-halo candidates is slightly larger than for the BHB stars, more than 98% of the objects are classified as halo stars. This result is in perfect agreement with the expectation and is also once again underlined by the  $E_{\text{tot}} - L_Z$ -diagram in Figure 7.6. The disk member region is essentially empty, at best the three thin disk candidates, marked in blue, and the five thick disk candidates, marked in green, are close to it. For the BSs the  $E_{\text{tot}}$ -axis of the diagram even exceeds the upper limit of being bound to the Galaxy of  $E_{\text{tot}} = 0$ , again suggesting that perhaps some unbound stars could be found among the kinematically most extreme objects.

Again it should be verified, whether the non-halo candidates according to the classification are really disk members by inspecting their orbits. These are shown for the three thin disk candidates in Figure 7.7 and for the five thick disk candidates in Figure 7.8. In the case of the thin disk candidates their orbits extend only moderately above and below the Galactic disk, show a high regularity and almost circular orbits in the outer region of the Galactic plane. This confirms them to be true disk members, although a thick disk membership seems to be more likely than a thin disk one. For the thick disk candidates, however, the evaluation of the orbits is rather difficult. The extension in  $Z$ -direction is again very moderate for all of them, especially for J0757-0825 with  $z_{\text{max}} \approx 1.5$  kpc, but, although the shape of the orbits is not really odd, it is also not very regular. Additionally, the orbits projected on the Galactic plane are substantially more eccentric than those of the thin disk candidates. So in general according to the orbits a halo membership seems to be more likely for all of the thick disk candidates, but since their kinematics show disk characteristics (otherwise they would not be classified as thick disk candidates), a disk membership can also not be excluded. The inspection of their Galactic orbits

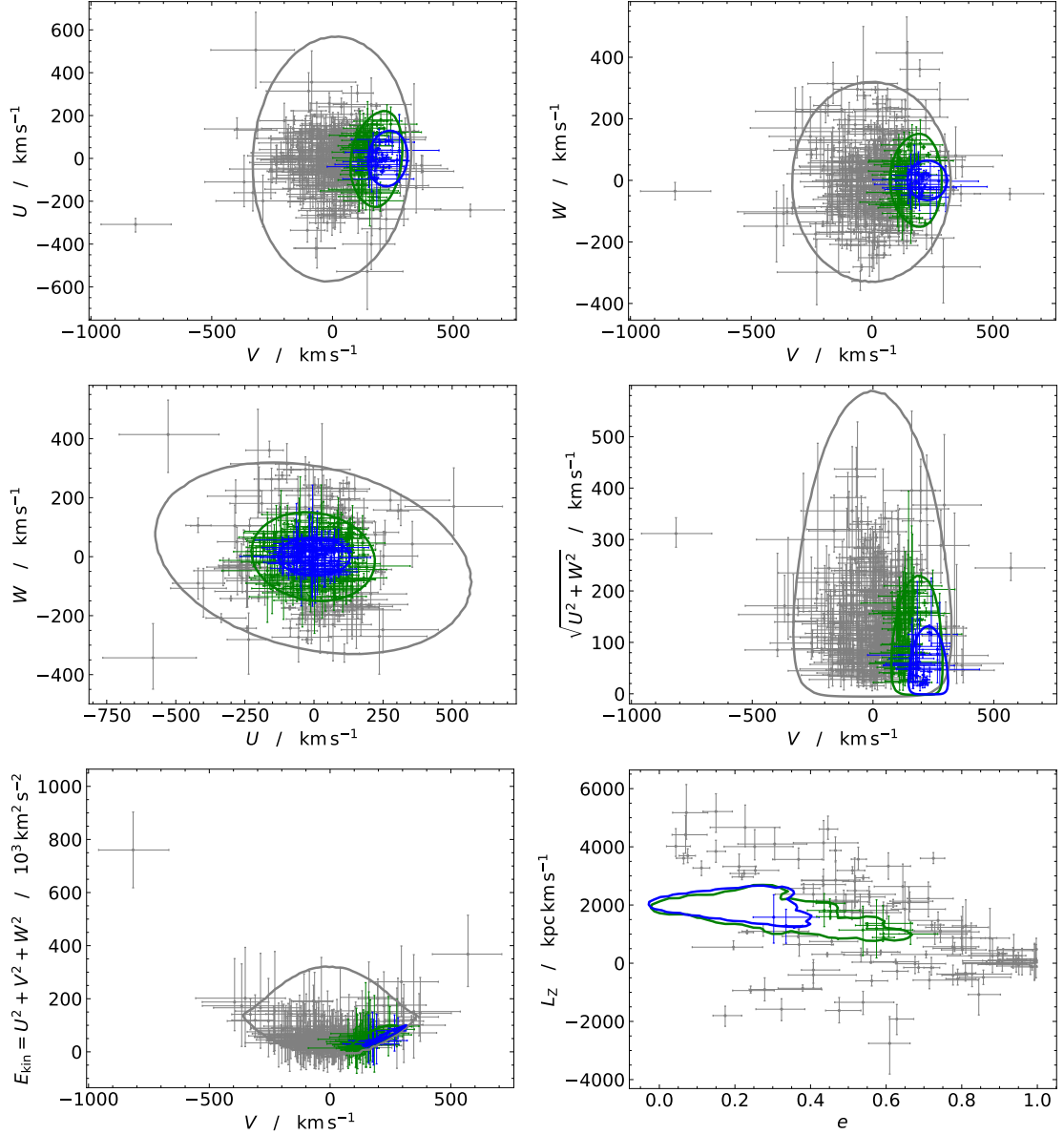


**Figure 7.5:** The six kinematic diagrams,  $U - V$ ,  $W - V$ ,  $W - U$ , Toomre,  $E_{\text{kin}} - V$  and  $L_z - e$  used for the classification of the BSs together with the respective  $3\sigma$  population contours for thin disk, thick disk and halo. Blue: thin disk. Green: thick disk. Gray: halo. The color-code is individual for each diagram. The most extreme objects are omitted in the diagrams, but are still part of the classification.

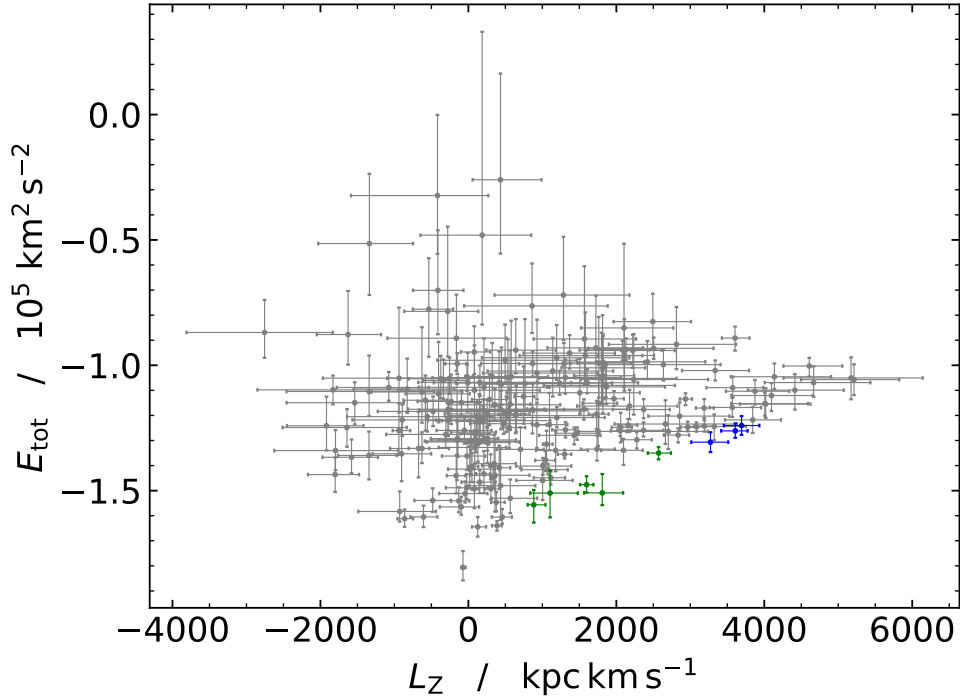


**Figure 7.6:**  $E_{\text{tot}} - L_Z$ -diagram for the MMT BS sample with the color-code of the classification. Blue: thin disk. Green: thick disk. Gray: halo. The most extreme objects are omitted.

does not allow for a clear-cut population assignment. They could be regarded as thick disk or halo members. It can be concluded once again that the classification scheme of section 4.2 provides a reliable filtering of possible non-halo candidates out of extremely halo dominated samples.

Kreuzer (2021) did not find any kinematically extreme object with  $v_{\text{Grf,min}} > 1000 \text{ km s}^{-1}$  within the MMT BS sample, as he did for the BHB stars. Whereas the results of the kinematic analysis in this work are consistent with that of Kreuzer (2021) in terms of the Galactic rest frame velocity, also for the BSs two candidates could be found with a low probability of being bound to the Galaxy  $P_b < 5\%$ . These are discussed separately together with the six BHB stars from section 6.3 in chapter 8.

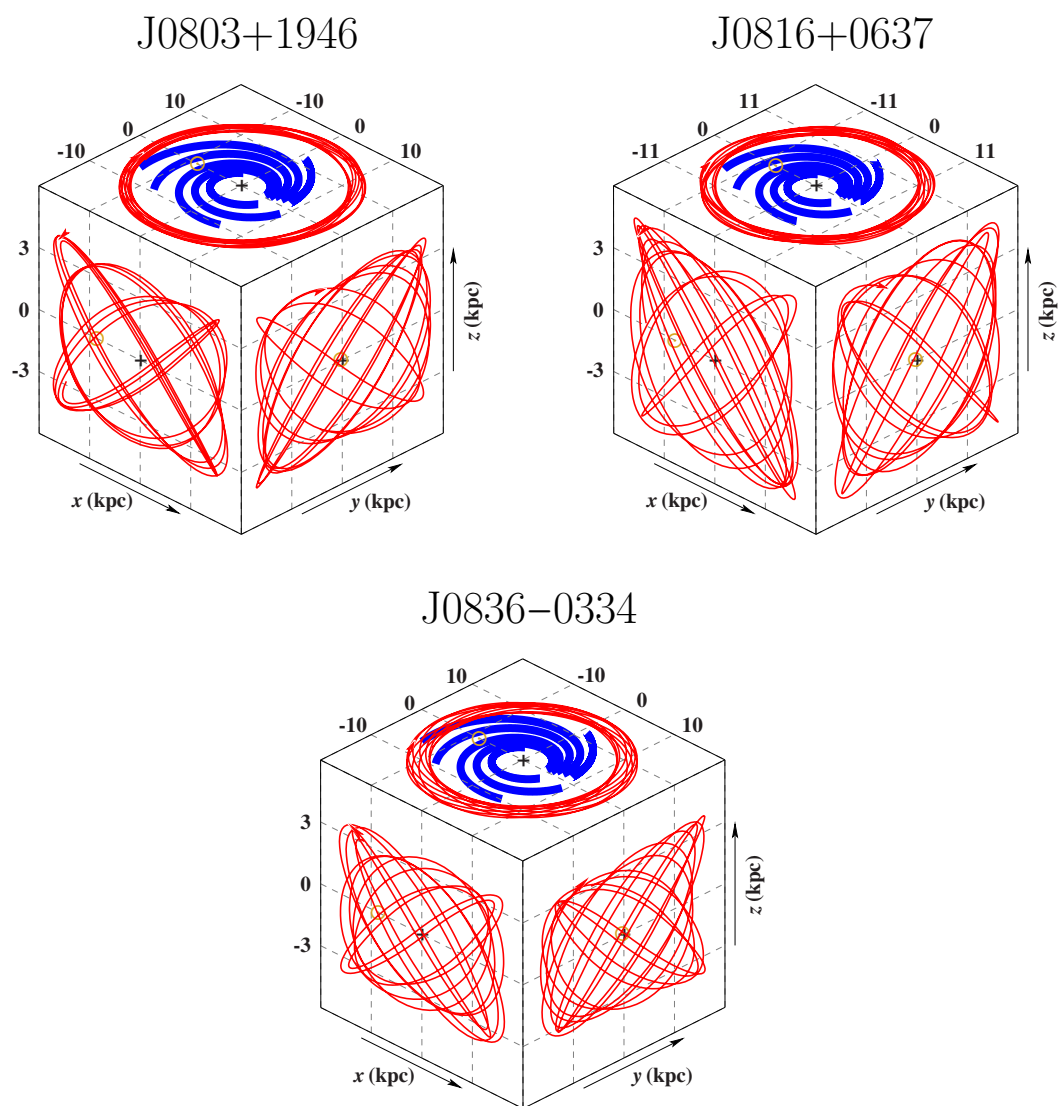


**Figure 7.7:** Same as Figure 5.11 for the three BS thin disk candidates.

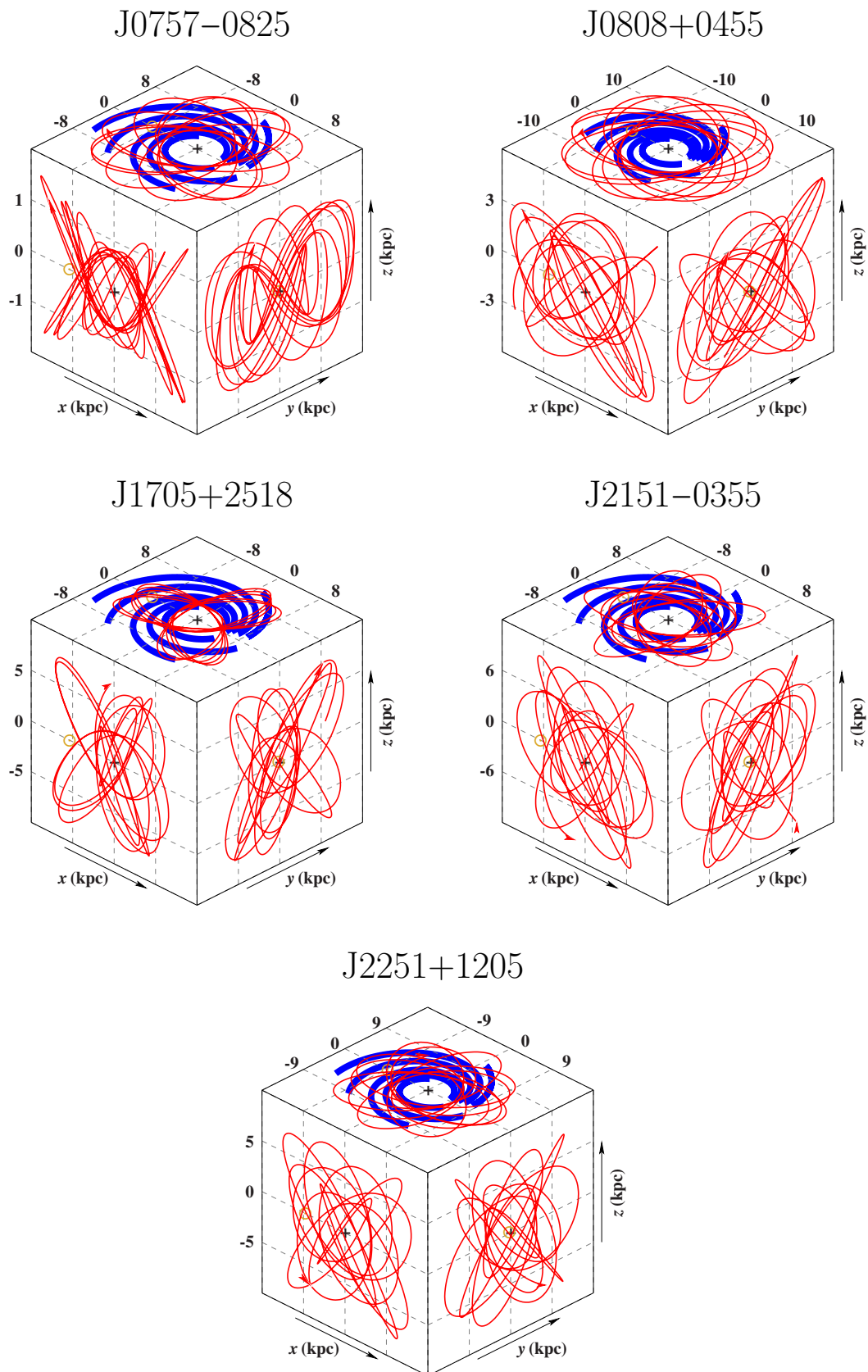


**Figure 7.8:** Same as Figure 5.11 for the five BS thick disk candidates.

## 8 Discussion of the kinematically most extreme objects

Six BHB stars and two BSs have been found to be possibly unbound to the Galaxy with probabilities exceeding 95% (see section 6.3 and section 7.3). First of all, it should be clarified how the boundness probability can be determined. In general, the essential criterion for a star to be unbound is that its Galactic rest frame velocity  $v_{\text{Grf}}$  exceeds the local escape velocity  $v_{\text{esc}}$  at the stars position (see for instance  $v_{\text{esc}}$  as function of the radius from the Galactic center in Figure 2.11). Both velocities can be derived from the Galactic orbits, for example via Monte Carlo simulations. Therefore, also the difference  $v_{\text{Grf}} - v_{\text{esc}}$  can be calculated. As an example, Figure 8.1 shows the resulting distribution for the star J0946+4256. The percentage of data points below zero is then defined as boundness probability. In the case of Figure 8.1, this results into  $P_b = 0.35\%$ , which is the smallest value of all eight candidates discussed in this chapter.

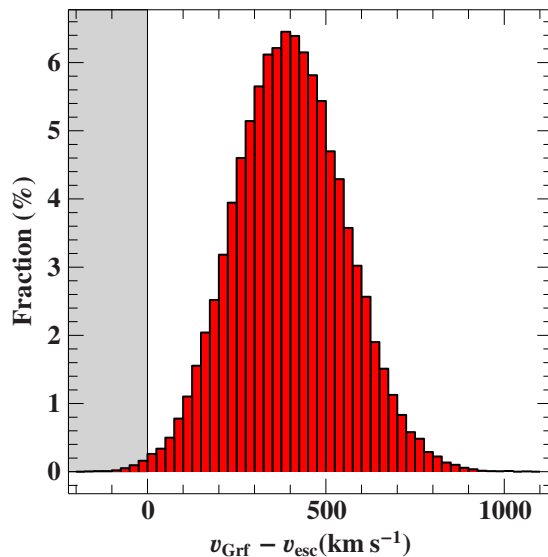


**Figure 8.1:** Distribution of  $v_{\text{Grf}} - v_{\text{esc}}$  for the star J0946+4256 resulting from a Monte Carlo simulation. The percentage of it below zero (gray area) is defined as boundness probability  $b$ . In this case it is  $b = 0.348\%$ .

The boundness probabilities and other important parameters are listed for the eight candidates in Table 8.1<sup>4</sup>. In principal, the quality of the data looks fine and none of the candidates can be excluded due to overall suspicious or unrealistic values. The uncertainties, of course, increase with increasing distance, but are still smaller than for the most extreme objects in Kreuzer (2021) listed in Table 6.1, owing to the improved precision of *Gaia* EDR3. Especially the data of J0946+4256, which is with a distance of  $\sim 30$  kpc the closest one of the eight candidates, has rather small uncertainties. Another hint if we can trust the data of the candidates is provided by the color-magnitude diagram in Figure 8.2. There the whole BHB and BS sample is plotted and the eight candidates are marked with red dots. It can be seen that all, except the blue straggler J0946+4256, cluster at the faintest edge of the diagram below an apparent magnitude of 20 mag, which is close to detection limit

<sup>4</sup> One of these (J1316+0019) is also an extreme object in Kreuzer (2021) (see Table 6.1). The other seven might be additional ones, for which no Gaia DR2 proper motions are available.

**Table 8.1:** Important parameters for all of the eight candidates being unbound to the Galaxy. Given are the effective temperature  $T_{\text{eff}}$ , the surface gravity  $\log(g)$ , the radial velocity  $v_{\text{rad}}$ , the spectrophotometric distance  $d$ , both proper motions  $\mu_{\alpha}$  and  $\mu_{\delta}$ , the Galactic rest frame velocity  $v_{\text{Grf}}$  and the boundness probability  $P_{\text{b}}$ .

Object	$T_{\text{eff}}$ (K)	$\log(g)$ (cgs)	$v_{\text{rad}}$ (km s $^{-1}$ )	$d$ (kpc)	$\mu_{\alpha}$ (mas yr $^{-1}$ )	$\mu_{\delta}$ (mas yr $^{-1}$ )	$v_{\text{Grf}}$ (km s $^{-1}$ )	$P_{\text{b}}$ (%)
J0002+3118	10510	3.80	$-215 \pm 10$	$54^{+6}_{-6}$	$6.6 \pm 2.8$	$-2.1 \pm 1.1$	$1595^{+743}_{-715}$	4.11
J0250-1535	9640	3.49	$49 \pm 13$	$59^{+8}_{-7}$	$0.9 \pm 0.7$	$2.5 \pm 0.9$	$880^{+281}_{-245}$	2.44
J0912+0424	9280	3.63	$194 \pm 14$	$61^{+9}_{-8}$	$-3.6 \pm 1.7$	$3.1 \pm 1.3$	$1448^{+585}_{-489}$	1.00
J0926+0927	9560	4.10	$74 \pm 12$	$55^{+9}_{-8}$	$-3.6 \pm 1.5$	$-2.2 \pm 1.0$	$981^{+362}_{-365}$	4.03
J0937+1823	8880	3.15	$131 \pm 8$	$105^{+31}_{-13}$	$-1.3 \pm 1.7$	$1.3 \pm 0.9$	$1205^{+725}_{-520}$	2.02
J0943+2914	10440	2.96	$135 \pm 19$	$153^{+14}_{-16}$	$-2.4 \pm 1.7$	$0.6 \pm 1.5$	$1455^{+1482}_{-775}$	1.74
J0946+4256	11320	4.35	$-241 \pm 13$	$29^{+5}_{-4}$	$0.6 \pm 0.2$	$-7.9 \pm 0.2$	$872^{+143}_{-143}$	0.35
J1316+0019	8200	2.94	$138 \pm 21$	$110^{+20}_{-20}$	$-0.3 \pm 1.6$	$-2.8 \pm 1.7$	$1258^{+812}_{-633}$	2.56

of *Gaia*. J0946+4256, however, is significantly brighter with an apparent magnitude of  $\sim 19$  mag. This suggests that the data of J0946+4256 is more reliable and hence, it will be focused on this candidate in the following.

Remarkably, it is one of two candidates with a negative radial velocity, suggesting that it comes towards us, maybe ejected from a globular cluster, a satellite galaxy or even from further away. The nature of a HVS ejected from somewhere within the Galactic plane, however, can be discarded, because of the negative radial velocity. Anyway, it appears to be a very promising candidate for an unbound star. The orbit of J0946+4256 is shown in Figure 8.3, calculated 100 Myr backwards in time. Obviously it is just a straight line and no special behaviour can be seen. This substantiates the hypothesis of an unbound star, coming either from the outskirts of the Milky Way halo or even from outside of it.

Anyway, there is also an alternative scenario possible for J0946+4256, namely that it is not a blue straggler, but the progenitor of an extremely low mass white dwarf (pre-ELM WD). Those are believed to evolve in a close binary system of a red giant and a common white dwarf. The expanding envelope of the red giant fills the Roche lobe of the WD and mass is transferred to it, but the WD can not ingest it. So it begins to surround the whole system (common envelope evolution) until it gets ejected and only the helium core of the red giant remains with a mass around  $0.2 M_{\odot}$ . Assuming that the temperature was not high enough to start helium burning, this helium core is not powered by any nuclear process any more. Hence, it contracts, moves towards higher temperatures and surface gravities and continuously degenerates until it reaches the ELM WD stage. This phase is called the pre-ELM phase. A Kiel diagram for the BHB stars and BSs overplotted with evolutionary tracks from Driebe et al. (1998) leading to the ELM stage is shown in Figure 8.4. It can be seen that the tracks cross the BHB and BS region, showing that a pre-ELM WD nature is in principal possible for J0946+4256, although those are very rare objects (only some tens of it have been found yet). Figure 2.2 also underlines that the region of pre-ELM WD candidates overlaps with that of the BSs. In the case of a pre-ELM WD nature, the mass ( $\sim 0.2 M_{\odot}$ ) would be much lower than the mass of a blue straggler ( $\sim 1.5 M_{\odot}$ ). This also reduces the spectrophotometric distance, as it

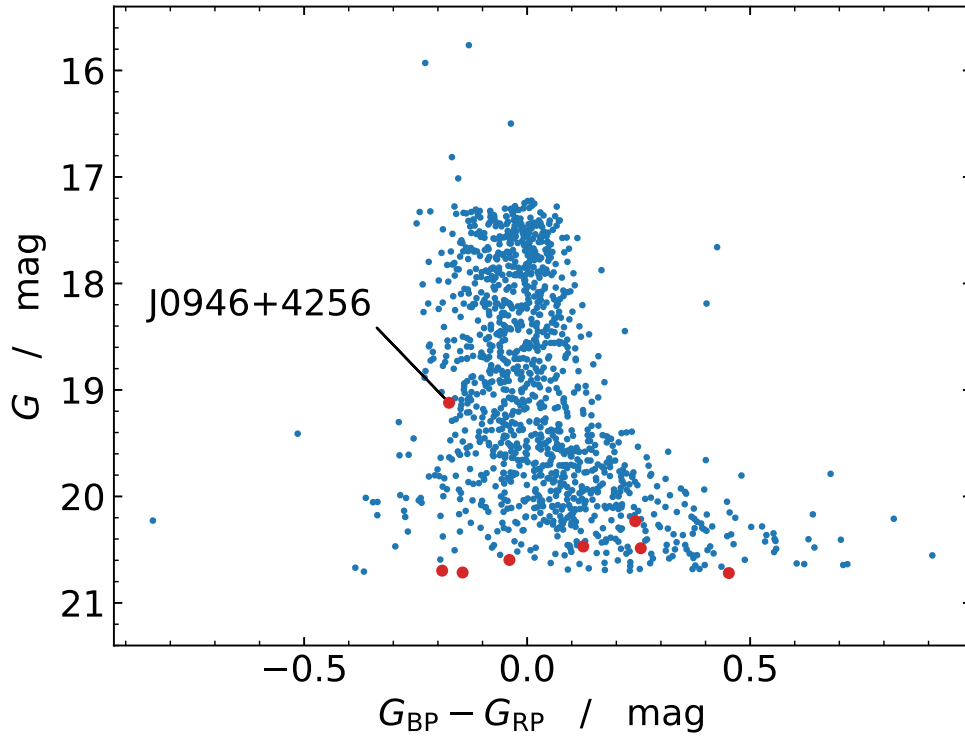


**Figure 8.2:** Color-magnitude diagram of the whole BHB and BS sample. The eight candidates being unbound to the Galaxy are marked with red dots.

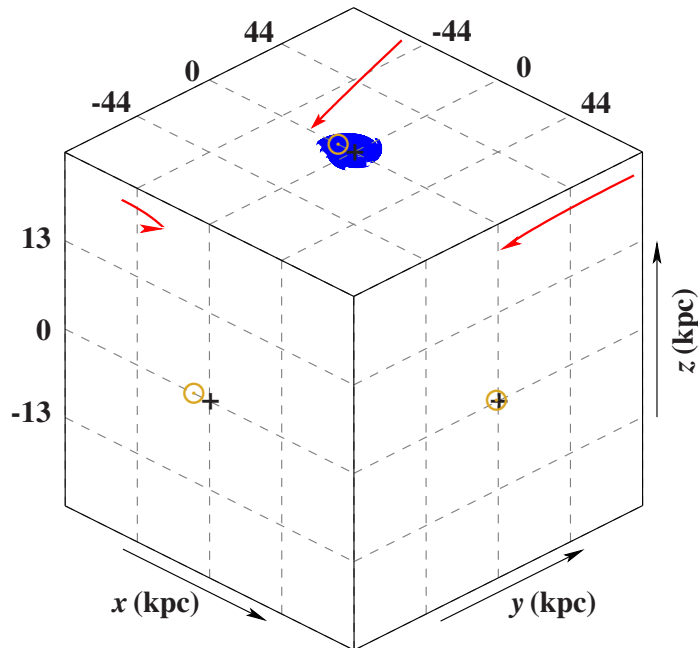


**Figure 8.3:** Same as Figure 5.11 for J0946+4256, but calculated 100 Myr backwards in time.

scales with  $\sqrt{M}$  (Equation 2.3). Therefore, the distance of J0946+4256 has been recalculated by multiplying the previous one with the factor

$$\sqrt{\frac{M_{\text{ELM}}}{M_{\text{BS}}}} = \sqrt{\frac{0.2 M_{\odot}}{1.5 M_{\odot}}} \approx 0.365.$$

This considerably reduces the distance  $d$  (now  $\sim 10$  kpc) and hence, also the tangential velocity, which scales linearly with  $d$ . The  $v_{\text{Grf}} - v_{\text{esc}}$ -histogram and the orbit in case of a pre-ELM WD nature are shown in Figure 8.5. Because the kinematics are far less extreme, it would be 100% bound and show a commonly shaped halo orbit. In fact, if J0946+4256 is truly a pre-ELM WD, also the radial velocity would be incorrect, because ELM WDs can only exist in close binary systems. The known systems show large radial velocity variations with periods of the order of one day. Thus, one would need to determine the systemic velocity of the system by distinguishing it from the radial velocity of the binary system. This would be only possible with spectroscopic follow-up observations, which could reveal the nature of J0946+4256 by searching for a binary companion. If discovered, it is most likely an pre-ELM WD and bound to the Galaxy. If not, it is most likely a BS and a candidate for being unbound to the Milky Way. Anyway it is a very exciting object.

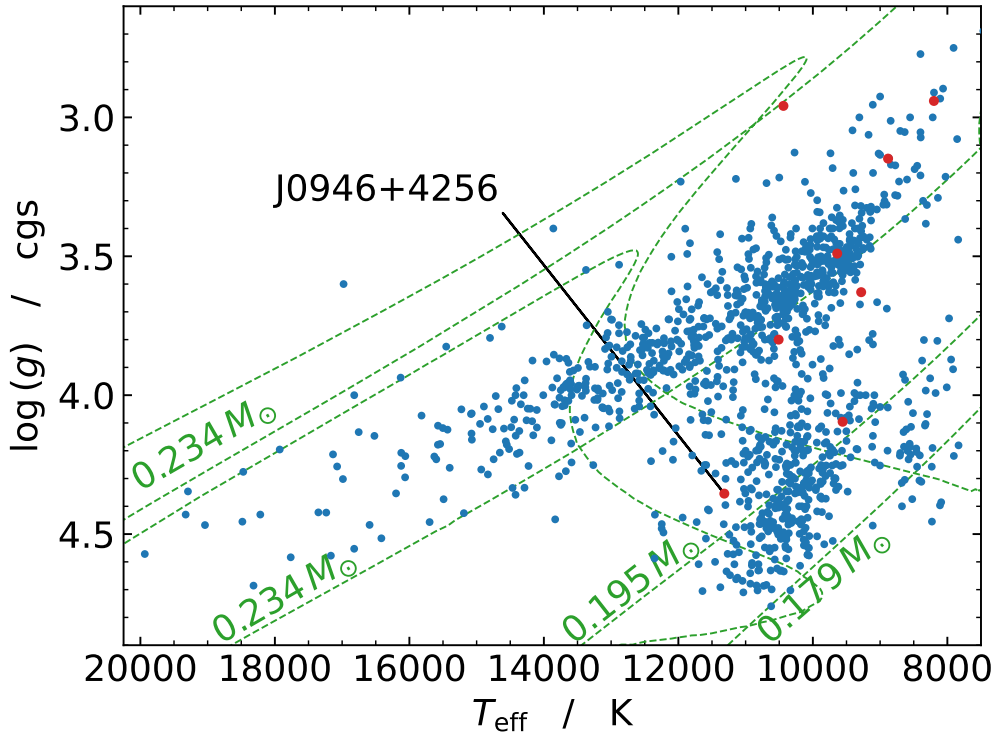


**Figure 8.4:** Kiel diagram for the whole BHB and BS sample. The eight candidates for being unbound to the Galaxy are marked with red dots. Overplotted are pre-ELM WD evolutionary tracks from Driebe et al. (1998).

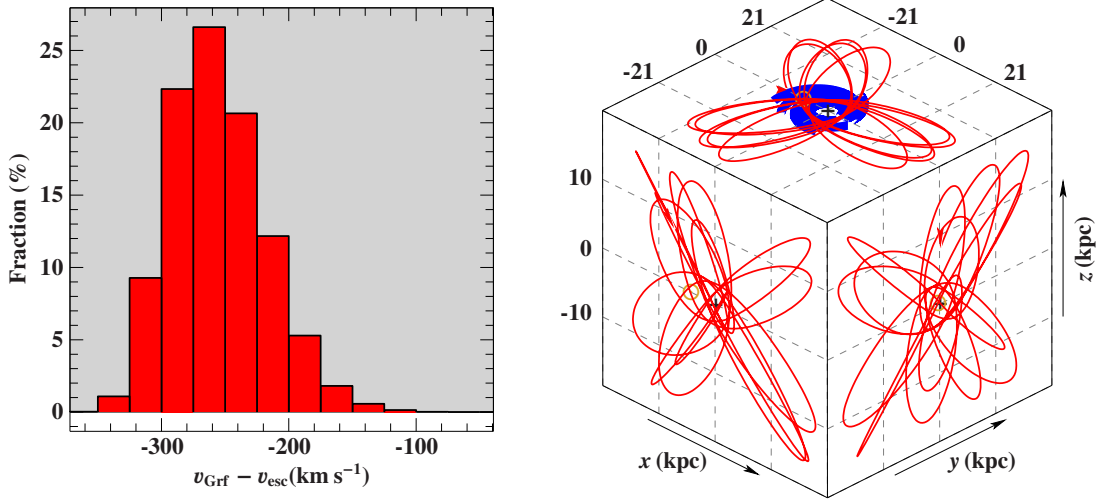


**Figure 8.5:** *Left:*  $v_{\text{Grf}} - v_{\text{esc}}$ -histogram for J0946+4256 in the case of an pre-ELM WD nature. The resulting boundness probability would be  $b = 100\%$ . *Right:* Three-dimensional orbit of J0946+4256 in the case of an pre-ELM WD nature showing common halo characteristics.

In conclusion it can be said all of the eight candidates for being unbound to the Galaxy are extremely interesting objects. Especially J0946+4256 is the highlight among the candidates, as it is closer and brighter than the others. Therefore, also the uncertainties on the kinematic parameters are smaller and the data seems to be very reliable. It is classified as BS, although an pre-ELM WD nature can also not be excluded. The scenario of an object coming from the outskirts of the Milky Way halo or even from outside of it towards us is very likely, since it has a negative radial velocity and a straight line as orbit. In the case of an pre-ELM WD, however, it would be 100% bound to the Galaxy on a common halo orbit. This question can only be solved by spectroscopic follow-up observations.

Furthermore, one should also not lose sight of the other seven candidates. Although, they are too close to the edge of the *Gaia* detection limit in terms of apparent magnitude, future astrometric data releases can maybe provide more reliable data. This could be, for example, *Gaia* DR4. It is anyway exciting, if these eight objects eventually can be confirmed or falsified as candidates for being unbound to the Galaxy.

## 9 Summary and outlook

The stellar population of the Galactic halo contains important information to understand the properties of our Galaxy, like its structure and motions, its history and its gravitational potential, especially that of the dark matter halo. Therefore, the MMT sample originally had the aim to construct an unbiased sample of faint blue halo stars, which is complete in a well defined colour and magnitude regime. It consists of a total number of 1897 objects, mainly blue horizontal branch (BHB) stars, blue stragglers (BSs) and white dwarfs (WDs), but also a few other stellar classes. Kreuzer (2021) already comprehensively analysed the whole amount of these objects by complementing the MMT spectroscopic data with *Gaia* DR2 astrometry. Recently, the early data release of the *Gaia* space mission, EDR3, provided improved proper motions. Therefore, it was tempting to revisit the MMT sample and to redo the kinematic analysis.

All three classes of stars (BHB, BS and WD) are revisited in a study of their kinematics. A comparison of the new *Gaia* EDR3 catalog to the previous one demonstrated not only the superior quality of the data, but also provided data for stars that *Gaia* DR2 had not measured. Spectrophotometric distances and radial velocities from Kreuzer (2021) were combined with *Gaia* EDR3 proper motions to calculate Galactic space velocity components ( $U, V, W$ ). The Galactic trajectories were computed by integrating the equation of motion back in time, aiming at assigning the stars to the respective Galactic populations of the thin and thick disks as well as the halo.

A classification scheme has been developed to distinguish between these three populations. It makes use of six kinematic diagrams, starting with the three basic velocity diagrams ( $U - V$ ,  $W - V$  and  $W - U$ ). Combinations of the components of the space motions are used to construct the Toomre-diagram ( $\sqrt{U^2 + W^2} - V$ ), as well as a diagram that makes use of the kinetic energy  $E_{\text{kin}} = U^2 + V^2 + W^2$  (vs  $V$ , the component in the direction of Galactic rotation). Properties of the orbits, which are their eccentricity  $e$ , their  $Z$ -component of the angular momentum  $L_Z$  and their maximum extend above or below the Galactic plane ( $z_{\text{max}}$ ) complete the set of criteria.  $3\sigma$  population contours have been calculated from a well-established Galactic model for each diagram and a system of population scores has been introduced, which count how often a star is located within which contour (see Figure 4.6). This classification has been applied on each of the major MMT samples, the white dwarfs, the blue horizontal branch stars and the blue stragglers.

Because of their proximity, it is a priori clear that the WD sample is dominated by thin disk stars and indeed, 79% turn out to be thin disk stars, 19% to be thick disk stars and 2% to be halo stars. All halo candidates were confirmed by the shape of their orbits, as they are chaotic and irregular. Because only few halo WDs are known today, the new discoveries are a significant addition and warrant follow-up observations.

---

Because of their large average distances, the MMT BHB sample, as well as the MMT BS sample, is expected to be dominated by the halo population. That is also represented by the resulting percentages of 99.5% and 98.2% halo objects, respectively. The classification scheme works fine for filtering out the non-halo candidates, as almost all of them were confirmed by the shape of their orbits.

The highlight of this work are eight candidates, six BHB stars and two BSs, which are possibly unbound to the Galaxy, as their boundness probability is below 5%. All of them show a decent data quality, although they are distant and very faint. Particularly one of them (J0946+4256, classified as BS) is outstanding, because the uncertainties on the data are even smaller than for the others and it is about two magnitudes brighter. This means, whereas the others are close to the detection limit of *Gaia* in terms of apparent magnitude, the data of J0946+4256 is reliable. Remarkably, it has a negative radial velocity and a straight line as orbit, suggesting that it comes from the outskirts of the Galactic halo or from even further away towards us.

Alternatively, the star could be closer than anticipated, if it were of lower mass. In recent years, a class of extremely low mass (ELM) WDs ( $M < 0.3 M_{\odot}$ ) has been found, which can be easily distinguished from BHB stars and BSs. However, stars transiting from the red giant stage to the cooling sequence (pre-ELM) might spectroscopically mimic BSs (or BHB stars). These are formed in a close binary system of a red giant and a common white dwarf. The gravitational force of the WD strips the envelope of the red giant, only leaving its helium core. This remnant subsequently contracts under its own gravity until it reaches the ELM WD cooling sequence, when the electron gas becomes fully degenerate. Evolutionary tracks in the Kiel diagram show, that such a nature is in principle possible for J0946+4256, although these objects are very rare. In this case its mass would be considerably smaller ( $\sim 0.2 M_{\odot}$  instead of a typical BS mass of  $\sim 1.5 M_{\odot}$ ), reducing its spectrophotometric distance, as well as its tangential velocity, by a factor of almost 3. Then it would be 100% bound with a common halo orbit. A reliable parallax would help to clarify the nature of this enigmatic object, as a direct comparison of the parallax distance with the spectrophotometric distance could reveal the mass of it. Unfortunately, an object with a distance of 30 kpc would have a parallax of 0.033 mas and even for *Gaia* DR5 a precision of only 0.149 mas is predicted (ESA 2022). Hence, it would need a future mission, even outperforming *Gaia*, to solve this problem that way. On the other hand spectroscopic follow-up observations could also clarify its nature by searching for a binary companion, through a radial velocity study, which must be existent in the case of a pre-ELM WD nature. But this will also be very difficult, because of the faintness of the star. Anyway, if discovered, it is most likely a pre-ELM WD and bound to the Galaxy. If not, it is most likely a blue straggler and a candidate for being unbound. In both cases it stays an very exciting object.

In general, better proper motions would significantly improve the precision of the kinematic parameters for all members of the MMT sample and, in particular, allow to confirm or falsify the six BHB and two BS candidates, which are possibly unbound to the Galaxy. Therefore, future astrometric data releases are eagerly awaited. These could be, for example, *Gaia* DR4 or even DR5. It is predicted, that DR5 proper motion errors will be three times smaller by the end of the *Gaia* mission (ESA 2022), which would help to constrain the boundness probability even for the faintest objects.

# References

- Allen, C. & Santillan, A. 1991, *Rev. Mexicana de Astron. Astrofis.*, 22, 255
- Altmann, M., Edelman, H., & de Boer, K. S. 2004, *Astronomy & Astrophysics*, 414, 181
- Anguiano, B., Majewski, S. R., Hayes, C. R., et al. 2020, *The Astronomical Journal*, 160, 43
- Bailer-Jones, C. A. L., Rybizki, J., Fouesneau, M., Demleitner, M., & Andrae, R. 2021, *Astronomical Journal*, 161, 147
- Bailer-Jones, C. A. L., Rybizki, J., Fouesneau, M., Mantelet, G., & Andrae, R. 2018, *The Astronomical Journal*, 156, 58
- Brown, W. R. 2016, *Physics Today*, 69, 52
- Brown, W. R., Geller, M. J., & Kenyon, S. J. 2014, *The Astrophysical Journal*, 787, 89
- Brown, W. R., Prieto, C. A., Beers, T. C., et al. 2003, *The Astronomical Journal*, 126, 1362
- Carollo, D., Chiba, M., Ishigaki, M., et al. 2019, *The Astrophysical Journal*, 887, 22
- Cesa, J. 2020, Equatorial coordinate system (celestial) - Wikimedia Commons, the free media repository, [Accessed 23-May-2022]
- de la Vega, A., Quillen, A., Carlin, J., Chakrabarti, S., & D’Onghia, E. 2015, *Monthly Notices of the Royal Astronomical Society*
- Dimpel, M. 2018, bachelor thesis, Friedrich Alexander University of Erlangen-Nuremberg, Germany
- Driebe, T., Schoenberner, D., Bloeker, T., & Herwig, F. 1998, *A&A*, 339, 123
- ESA. 2022, *Gaia* webpage, <https://www.cosmos.esa.int/web/gaia/science-performance>, [Accessed 21-July-2022]
- Gaia Collaboration, Brown, A. G. A., Vallenari, A., et al. 2018, *A&A*, 616, A1
- Gaia Collaboration, Brown, A. G. A., Vallenari, A., et al. 2021, *A&A*, 650, C3
- Gaia Collaboration, Prusti, T., de Bruijne, J. H. J., et al. 2016, *A&A*, 595, A1
- Gilmore, G. & Reid, N. 1983, *Monthly Notices of the Royal Astronomical Society*, 202, 1025

- Heber, U. 2009, *Annual Review of A&A*, 47, 211
- Helmi, A. 2020, *Annual Review of Astronomy and Astrophysics*, 58, 205
- Irrgang, A. 2014, PhD thesis, Friedrich Alexander University of Erlangen-Nuremberg, Germany
- Irrgang, A., Wilcox, B., Tucker, E., & Schiefelbein, L. 2013, *A&A*, 549, A137
- Johnson, D. R. H. & Soderblom, D. R. 1987, *The Astronomical Journal*, 93, 864
- Kreuzer, S. 2021, PhD thesis, Friedrich Alexander University of Erlangen-Nuremberg, Germany
- Lane, J. M. M., Bovy, J., & Mackereth, J. T. 2021, *Monthly Notices of the Royal Astronomical Society*, 510, 5119
- Martin, C. 2020, Stellar parallax - Wikimedia Commons, the free media repository, [Accessed 23-May-2022]
- Martin, P., Jeffery, C. S., N., N., & Woolf, V. M. 2016, *Monthly Notices of the Royal Astronomical Society*, stw3305
- Mignard, F. 2009, <https://www.cosmos.esa.int/web/gaia/l2>, [Accessed 11-July-2022]
- MMTO. 2022, MMTO website, <https://www.mmtto.org/>, [Accessed 29-May-2022]
- Naidu, R. P., Conroy, C., Bonaca, A., et al. 2020, *The Astrophysical Journal*, 901, 48
- Odenkirchen, M. & Brosche, P. 1992, *Astronomische Nachrichten*, 313, 69
- Pauli, E.-M., Napiwotzki, R., Altmann, M., et al. 2003, *Astronomy and Astrophysics*, 400, 877
- Pauli, E. M., Napiwotzki, R., Heber, U., Altmann, M., & Odenkirchen, M. 2006, *Astronomy and Astrophysics*, 447, 173
- Universität Heidelberg. 2022, website university of Heidelberg, <https://zah.uni-heidelberg.de/de/institute-des-zah/astronomisches-rechen-institut/willkommen-auf-den-seiten-des-gaiaari-projektes>, [Accessed 30-May-2022]



## Acknowledgements

First and foremost, I would like to thank Uli Heber for giving me the opportunity for this work, for introducing me to the highly interesting topic of stellar kinematics and for the advice and support throughout the whole time. I also want to thank Matti Dorsch and Aakash Bhat, as well as Uli, for the nice discussions in our weekly meetings. A special thanks to Matti for helping me to solve any technical issue I had and Philipp Jessberger for the nice conversations, while driving me from the train station to the observatory several times.

Many thanks to Simon Kreuzer for providing the data of your work and Andreas Irrgang for providing and continuously improving your stellar isiscripts.

Last but not least I want to thank my family and friends for their ongoing support and care. Thank you all!

# Eigenständigkeitserklärung

Hiermit bestätige ich, dass die vorliegende Arbeit von mir selbst verfasst wurde, dabei nur die angegebenen Quellen und Hilfsmittel verwendet wurden und dass sie nicht in wesentlichen Teilen mit einer Arbeit übereinstimmt, die bereits einer anderen Prüfungsbehörde vorgelegt wurde.

Erlangen, den 25. Juli 2022

---

Ort, Datum

---

Sebastian Weich